



**The Interaction of  
Radio Waves with the  
Auroral Ionosphere**

Thesis submitted for the degree of  
Doctor of Philosophy  
at the University of Leicester

By

**Giles Edward Bond**  
Department of Physics and Astronomy  
University of Leicester

July 1997

UMI Number: U095799

All rights reserved

INFORMATION TO ALL USERS

The quality of this reproduction is dependent upon the quality of the copy submitted.

In the unlikely event that the author did not send a complete manuscript and there are missing pages, these will be noted. Also, if material had to be removed, a note will indicate the deletion.



UMI U095799

Published by ProQuest LLC 2013. Copyright in the Dissertation held by the Author.  
Microform Edition © ProQuest LLC.

All rights reserved. This work is protected against  
unauthorized copying under Title 17, United States Code.



ProQuest LLC  
789 East Eisenhower Parkway  
P.O. Box 1346  
Ann Arbor, MI 48106-1346

**Giles Edward Bond**

**The Interaction of Radio Waves with the  
Auroral Ionosphere**

**Abstract**

A high power radio wave propagating through the ionosphere perturbs the natural plasma in a number of ways. These include bulk changes in the electron temperature and density, and the excitation of plasma waves and instabilities. The ionosphere can be regarded as a natural plasma laboratory, with far greater scale sizes than anything achievable in a conventional laboratory, thus giving unique access to a range of plasma waves and instabilities. In this thesis results from two campaigns involving the EISCAT (European Incoherent SCATter) ionospheric modification facility (heater) at Tromsø, Northern Norway are presented.

The first campaign, in February 1995, was principally concerned with modification of the auroral electrojet region during both disturbed and quiet conditions. During this campaign the EISCAT UHF incoherent scatter radar was utilised to achieve the first experimental demonstration of artificial ionospheric cooling by a high power radio wave.

For the second campaign, in April 1996, the most important diagnostic was CUTLASS (Co-operative UK Twin Located Auroral Sounding System), which can measure power backscattered from field aligned irregularities produced during heating. It has been found that irregularities are excited over a horizontal spatial extent of around 175 km, which far exceeds the nominal width of the heater beam. The temporal decay of artificial irregularities after the heater has been switched off exhibits a two stage decay process, and the irregularities remain in the ionosphere for up to four minutes after heater-off.

In addition to these experimental studies, a computer model has been developed to investigate the electron temperature and density changes which are induced in the ionospheric D- and E-regions during periods of electrojet activity. The model reproduces the experimental observations, and predicts reduced artificial heating efficiency under disturbed natural conditions.

## Acknowledgements

I would like to thank the following people for their help during my postgraduate studies:

Professor Tudor Jones and Professor Stan Cowley for allowing me the opportunity to study in the Radio and Space Plasma Physics Group.

Professor Terry Robinson for his encouragement and numerous useful discussions.

The members of the Radio and Space Plasma Physics Group, including Jon “always injured” Angell, Neil “terminator” Arnold, Eric “young at heart” Bradshaw, Jackie “in the navy” Davies, Rob “firework” Dickens, Paul “spice boy” Eglitis, John “father” Gauld, Adrian “caveman” Hall, Graham “sprinter” Holdsworth, Hina “wee” Khan, Mark “Foxes in Europe I don’t believe it” Lester, Steve “fat” Milan, Marc “the dutchman” Mijnaerends, Gabby “gobs” Provan, Brian “squash guru” Shand, Jon “part-time” Storey, John “Bob” Taylor, Chris and Julian “the men with the mobiles”, Nigel “computer guru” Wade, Darren “don’t call me Daz” Wright, Tim “natural born killer” Yeoman, the RSL boys: especially Clive, Lino, and Alan “chopper” Stocker, the workshop crew Peter, Stuart and Mick.

Last but not least a special thank-you to Aurélie for all her love and support.

**To my family, especially Mum,  
Dad and Erica**

# Contents

	<b>Page</b>
<b>Chapter 1 Introduction</b>	
1.1 The plasma state	1
1.2 The Sun and magnetosphere	1
1.3 The upper atmosphere	2
1.4 The high latitude ionosphere	3
1.5 Measurement techniques	4
1.6 Ionospheric modification	4
1.7 Aims of the present investigation	5
1.8 Concluding remarks	6
<b>Chapter 2 Review of Large-Scale Ionospheric Modification</b>	
2.1 Introduction	7
2.2 Plasma frequencies and gyrofrequencies	8
2.3 Propagation of a radio wave in the ionosphere	9
2.4 O- and X-mode effects	10
2.5 RF modification of the E-region	11
2.6 Theory of RF modification	12
2.7 The Farley-Buneman Instability	13
2.8 Other heating and loss processes	16
2.9 Artificial heating of E-region irregularities	18
2.10 Previous modelling studies	20
2.11 Electron temperature modification	21
2.12 Electron density modification	22
2.13 Concluding remarks	22
<b>Chapter 3 Review of Previous Work on Artificial Field Aligned Irregularities</b>	
3.1 Introduction	24
3.2 Parametric instabilities	24
3.3 The thermal parametric instability	25
3.4 Theory of FAI decay	27
3.5 Review of experimental work	32
3.5.1 Observations of decaying FAI	34

3.6 Concluding remarks	35
------------------------	----

## **Chapter 4 Instrumentation**

4.1 Introduction	36
4.2 HF modification	36
4.3 The EISCAT RF modification facility	37
4.3.1 Heating facility transmitters	37
4.3.2 The heater antenna arrays	38
4.3.3 Heater modulation	39
4.4 Incoherent scatter	
4.4.1 Development of incoherent scatter	40
4.4.2 Parameters determined by incoherent scatter	41
4.4.3 The EISCAT radars	42
4.4.4 Incoherent scatter measurement techniques	43
4.4.5 EISCAT programmes	44
4.4.6 Incoherent scatter data analysis	44
4.4.7 Incoherent scatter measurement errors	45
4.5 Coherent scatter	
4.5.1 Coherent scatter mechanisms	46
4.5.2 The CUTLASS radar	46
4.5.3 Coherent scatter measurement techniques	47
4.6 The low power diagnostic system	48
4.7 Concluding remarks	49

## **Chapter 5 Artificial Modification of the Auroral E-Region**

5.1 Introduction	51
5.2 Experimental procedure	52
5.3 Experimental results	52
5.4 Model calculations	54
5.5 Discussion and Conclusions	
5.5.1 Discussion of Observations	58
5.5.2 Discussion of Model Results	60
5.6 Summary	63

## **Chapter 6 CUTLASS Spatial Observations of the Artificially Modified Ionosphere**

6.1 Introduction	65
------------------	----

6.2 Experimental arrangement	66
6.3 Observations	
6.3.1 CUTLASS observations of the horizontal extent of the heated region	66
6.3.2 Estimating the size of the heated region	69
6.3.3 CUTLASS observations during vertical and field aligned heater beam propagation	71
6.3.4 Results from the Iceland radar	71
6.4 Discussion and conclusions	
6.4.1 CUTLASS spatial measurements	71
6.4.2 Comparisons of vertical and field-aligned heater beam positions	75
6.4.3 Iceland observations of the heated region	75
6.5 Summary	76

## **Chapter 7 Decay Characteristics of Heater Induced Irregularities**

7.1 Introduction	78
7.2 Experimental arrangement	78
7.3 Observations	
7.3.1 CUTLASS observations	79
7.3.2 EISCAT observations	81
7.4 Discussion	82
7.5 Summary	85

## **Chapter 8 Summary and Conclusions**

8.1 Introduction	87
8.2 Summary of principal observations	87
8.3 Further work	89

<b>References</b>	<b>93</b>
-------------------	-----------

# **Chapter 1**

## ***Introduction***

### **1.1 The plasma state**

Matter can be classified in terms of four states, the first three of which are familiar in everyday life: solid, liquid and gaseous. These three states are categorised according to the strength of the bonds that hold their constituent particles together. The fourth state of matter, plasma, is slightly different as it forms through a gradual change rather than a well defined phase transition at a specific temperature and pressure. In a plasma, some of the neutral particles are split into positively charged ions and negatively charged electrons, a process known as ionisation. Because plasmas contain charged particles they interact strongly with electromagnetic fields, and exhibit many properties not associated with the other states of matter. Plasma is the most common state of matter in the universe, and although plasmas on the Earth's surface tend to be limited to laboratories, a naturally occurring plasma, known as the ionosphere, is found in the Earth's atmosphere (Fig. 1.1). The ionosphere provides a natural plasma laboratory in the near-Earth environment, which can be utilised to perform unique plasma physics experiments which would not be possible in the confines of a laboratory. In addition, the strong interaction which occurs between the ionosphere and radio waves has numerous technological implications, particularly in the field of radio communications.

### **1.2 The Sun and magnetosphere**

The Sun is the energy source which drives the whole atmosphere, including the ionosphere. It emits most radiation in the visible spectrum, but also emits radio waves, X-rays and energetic particles. Hot plasma moving out from the Sun forms the solar wind, which carries with it the interplanetary magnetic field or IMF. The activity of the Sun is not constant, and the most significant variation is the 11 year solar cycle, which is often quantified in terms of the number of sunspots visible on the Sun's surface.

The Earth lies approximately  $1 \times 10^8$  km from the Sun, although it is positioned within the IMF and the solar wind, so it can almost be said to lie within the Sun's atmosphere. Fig. 1.2 presents a schematic of the magnetosphere, which is the area around the Earth governed by its magnetic field. This region is compressed towards the dayside of the Earth and elongated on the nightside, due to the interaction with the solar wind. At high latitudes, particles precipitate from the magnetosphere down the open magnetic field lines into the ionosphere, where aurorae are formed

(Northern and Southern lights). Particles can also transfer from the ionosphere into the plasmasphere, which is a magnetospheric region of cold, dense plasma near the Earth. There can also be a flow of heat from the magnetosphere to the ionosphere, and magnetospheric electric fields map down into the ionosphere, driving current systems known as electrojets.

### **1.3 The upper atmosphere**

The ionosphere is the partially ionised region of the Earth's upper atmosphere, which surrounds the Earth between 60 and 1000 km above the surface. The influence of gravity causes both the neutral atmosphere and the ionosphere to be horizontally stratified. Fig. 1.1 illustrates how the atmosphere is organised into a series of regions which are characterised by their vertical temperature structure. Between 100 and 1000 km lies the thermosphere, where solar heating gives a rapid increase in temperature. Below the thermosphere is the mesosphere, where there is a decrease in temperature and the heavier elements become fewer. The stratosphere lies between 10 and 30 km, and here the temperature falls with decreasing height due to photon absorption. The region below 10 km is the troposphere. In this region the temperature decreases with increasing height, and the turbulence present causes weather.

The ionosphere is defined separately from the atmospheric layers, and is organised according to electron density (Fig 1.1). The structure and properties of the ionosphere vary rapidly with height. During the day, electromagnetic radiation from the sun is incident on the neutral atmosphere, and this produces ionisation of a small fraction ( $< 1\%$ ) of the neutral particles. The electron density at a particular height is determined by a balance between ionisation by the sun (photoionisation) and various loss processes such as chemical recombination between ions and electrons (Chapman, 1931). The radiation is absorbed as it passes down into the increasingly dense atmosphere. In the F-region the ionisation is produced by the most strongly absorbed of the extreme ultra violet radiation. In this region, the collision frequencies are low, and the electrons typically recombine before they can lose their energy through collisions with the neutral gas. For this reason the F-region electron temperature is higher than that of the ions and neutrals. In Summer the F-region splits in two, sometimes referred to as the F<sub>1</sub>-region for heights below 250 km, and the F<sub>2</sub>-region for heights above 250 km. The peak ionospheric plasma density occurs in the F-region, and values as high as  $10^{12} \text{ m}^{-3}$  can occur. The F-region above this peak is known as the "topside" ionosphere, and the electron density in this region is due to diffusion rather than a balance between photoionisation and recombination. Below the F-region is the E-region, which

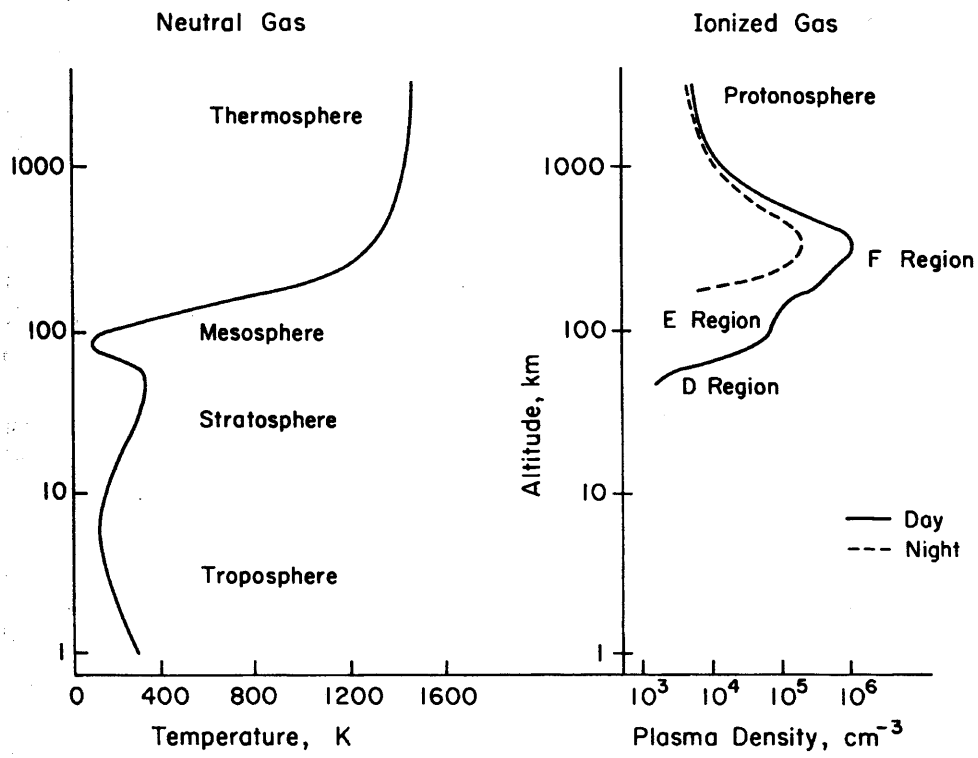


**Figure 1.1.** Profiles of atmospheric temperature and ionospheric plasma density (after Kelley, 1989).

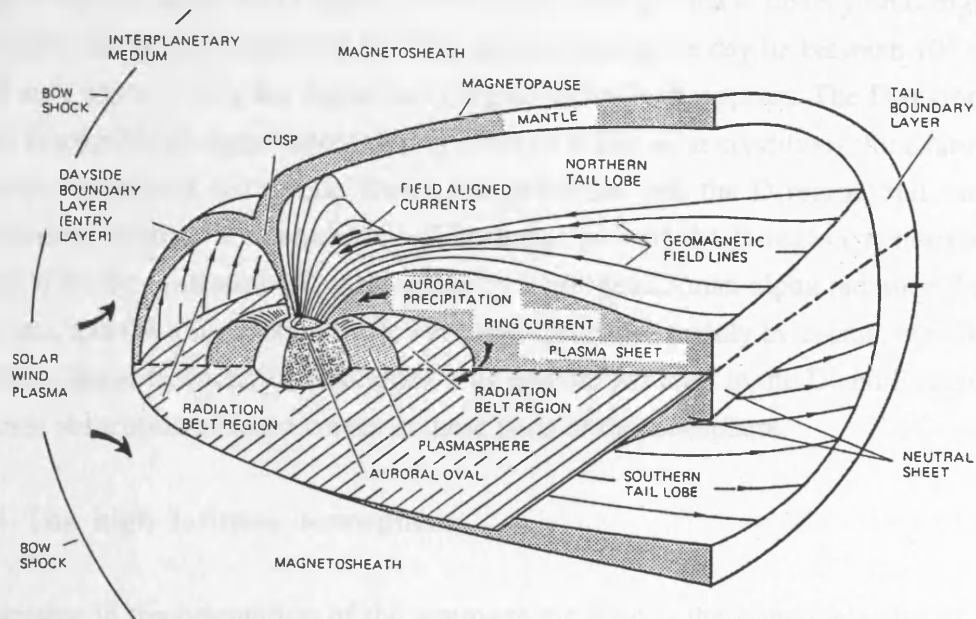


**Figure 1.2.** A three dimensional schematic of the Earth's magnetosphere (after Kelley, 1989).

begins at around 150 km. Ionisation here is produced by soft X-rays and extreme ultraviolet radiation from the sun. The first ionospheric reflections of radio waves were observed from this region, and it was given the name “E” for “Electrified”. Reflection also works above the E-region, where the auroral kilometric radiation (AKR), created by the precipitating particles above the ionosphere, does not reach the ground because of reflection from the E-layer. Between 50 and 80 km is the region usually called the D-region. The density of the plasma in this region is highly variable, but typical values for electron density during the day lie between  $10^8$  and  $10^9$  m<sup>-3</sup>, whilst during the night the D-region virtually disappears. The D-region is also susceptible to disturbances during times of active solar conditions, for example X-rays associated with solar flares can penetrate into the D-region and cause enhanced electron concentrations. The upper part of the D-region is normally caused by the ionisation of nitric oxide by hydrogen Lyman-alpha radiation from the sun, and the ionisation in the lower part is produced mainly by cosmic rays. The high collision frequency of electrons with heavier particles in the D and E regions causes absorption of radio waves in these parts of the ionosphere.

#### **1.4 The high latitude ionosphere**

Variation in the orientation of the geomagnetic field is the principle cause of the latitudinal variation in ionospheric structure. At equatorial latitudes the field lines are nearly parallel to the Earth’s surface and this geometry gives rise to the equatorial anomaly, a minimum in electron density caused by the electrodynamic lift of the plasma. The plasma lifted out of the equator in this way diffuses down field lines to create secondary maxima in the electron density either side of the equator.

The high latitude ionosphere is a particularly dynamic region, and one which has been the subject of intense scientific study. The geomagnetic field lines which thread the high latitude ionosphere extend far into the Earth’s magnetosphere, and some even open directly into interplanetary space. The region where the magnetic field lines are “open”, i.e. do not connect to a conjugate point in the opposite hemisphere, is known as the polar cap. The open field lines allow the transfer of solar wind particles into the ionosphere (polar rain) and the transfer of light ions out of the ionosphere (polar wind).

Neutral ionospheric species are excited by highly energetic (1-100 keV) particles which precipitate into the ionosphere from the magnetosphere. The excited neutrals decay by emitting visible photons, producing optical aurorae. Auroral activity occurs in an high latitude zone known as the auroral oval, which extends equatorward during periods of increased geomagnetic activity.

Electric fields are set up in the magnetosphere which map down the highly

conducting magnetic field lines into the high latitude ionosphere. In the F-region, where collision frequencies between the charged particles and the neutrals are low, the electrons and ions drift with the Hall velocity, which is determined by the vector product of the geomagnetic field and the externally applied electric field. In the E-region, the ions are collisionally restrained but the electrons continue to flow, producing a current known as the auroral electrojet. The flow of ions and electrons driven by these electric fields are routinely measured at speeds greater than  $500 \text{ ms}^{-1}$ , and flows as high as  $3000 \text{ ms}^{-1}$  are not uncommon.

### 1.5 Measurement techniques

Diagnostic tools for investigating the Earth's ionosphere fall into two basic categories, space based and ground based. Space based systems are mounted on satellites and make *in-situ* measurements of ionospheric parameters with probes such as magnetometers and mass spectrometers. Ground based equipment includes radio sounders, optical equipment and radars. In this thesis, only ground based observations are utilised, with particular emphasis on radars.

Radar measurements of the ionosphere involve scattering radio waves from plasma waves and instabilities, and can be classified into two main techniques: coherent and incoherent scatter. Incoherent scatter relies on the transmitted radio wave scattering from electron-acoustic and ion-acoustic waves, which occur naturally due to the thermal motion of the plasma. The scattering cross-section of these waves is very small, and only a tiny fraction of the transmitted power is scattered back to the radar. For this reason, incoherent scatter radars need powerful transmitters and sensitive receivers in order to receive detectable scatter.

Coherent scatter radars operate by scattering from density perturbations in the plasma. These perturbations can occur naturally, particularly during periods of disturbed ionospheric conditions, and can also be excited artificially. The frequency of the transmitted wave determines the wavelength of the irregularities which are observed. Incoherent scatter and coherent scatter represent complimentary techniques, and are very useful when combined in a single experiment, such experiments are possible in Northern Scandinavia, where the EISCAT incoherent scatter radar lies in the field of view of the CUTLASS coherent scatter radar.

### 1.6 Ionospheric modification

Artificial ionospheric modification is the deliberate perturbation of ionospheric plasma parameters. This includes bulk changes in the electron temperature and density, and the excitation of plasma waves and instabilities. Ionospheric

modification can be achieved by a number of different means, including explosions on the ground and in the ionosphere, emissions from rockets, both from exhaust gases and deliberate chemical releases, and high power radio waves. In this thesis only the modification of the ionosphere by high power radio waves (heating) is discussed. Heating experiments typically utilise radio waves in the range 3-15 MHz. These waves reflect within the ionosphere, and modification effects are maximised at the reflection point.

Ionospheric modification by high power radio waves provides a number of unique opportunities for scientific investigation. Changes in bulk parameters such as electron temperature and density can be achieved in a controllable manner, and through studying the response of the ionosphere to these changes a better understanding of natural ionospheric processes, such as recombination rates, can be achieved. In the context of modification experiments, the ionosphere can be regarded as a natural plasma laboratory. The ionospheric plasma has far greater scale sizes than anything achievable in a conventional laboratory, thus giving unique access to a range of plasma waves and instabilities.

### **1.7 Aims of the present investigation**

An ionospheric heater and many diagnostic tools, including incoherent scatter radars, are located at the EISCAT (European Incoherent SCATter) site at Tromsø in Northern Norway. EISCAT represents a world class facility for ionospheric research, and the University of Leicester has been associated with numerous experimental campaigns at EISCAT since the early 1980s. These campaigns have made use of the many diagnostic tools available, most notably the EISCAT incoherent scatter system. These experiments are continuing, and one of the aims of the current investigation has been to measure the response of the E-region to ionospheric modification, during periods of increased electron flow speed.

During quiet conditions, an artificial increase in electron temperature is often observed during heating experiments in the auroral E-region. When the plasma flow speed increases to a level above the threshold for the Farley-Buneman instability, a natural increase in electron temperature occurs. If the heater is turned on during these disturbed conditions, the theory of Robinson (1994) predicts a direct interaction between the heater wave and the instability which can cause quenching of the instability mechanism. The natural heating contribution can be reduced or eliminated, and the energy input from the heater wave is not enough to compensate, leading to an overall electron temperature decrease. In this thesis, incoherent scatter observations in the auroral E-region have been utilised to investigate the theory of Robinson (1994).

A self-consistent computer code has been developed which calculates the electron temperature and density perturbations produced by a high power radio wave propagating through the auroral D- and E-regions. For the first time, the model also includes the energy contribution due to Farley-Buneman heating in the electrojet, and frictional heating due to plasma flow.

The University of Leicester has recently built CUTLASS (Co-operative UK twin-located Auroral Sounding System), a new coherent scatter radar system, which looks out over the region of space above the EISCAT heating facility. This new facility is able to operate in high temporal and spatial resolution, and provides many new opportunities for the observation of plasma irregularities excited during modification experiments.

In this thesis, an experiment is described in which CUTLASS has been utilised to diagnose the horizontal spatial extent of the heated region over Tromsø. In order to establish the true size of the heated patch the pulse shape and the beam pattern of the radar have been deconvolved from the backscatter power as measured by the radar. The deconvolved data indicate that irregularities can be excited significantly outside the 3 dB point of the heater beam, which is often used to describe the width of the heated region.

The decay characteristics of artificial field aligned irregularities after heater-off have been diagnosed by CUTLASS. Artificially induced irregularities have been observed to remain in the ionosphere for a number of minutes after heater-off, and a distinct two stage decay process has been identified. The observations have been interpreted in terms of diffusion and mode conversion processes in the ionosphere.

## **1.8 Concluding remarks**

In this thesis, observations are presented of E-region electrons being cooled by ionospheric modification during disturbed conditions. A model of a high power radio wave propagating through the ionosphere during periods of high plasma flow speed is also presented.

In addition, results are presented from the CUTLASS coherent scatter radar. These results show the decay of artificial irregularities after heating. Observations of the spatial extent of the artificially heated region are also included.

## Chapter 2

# *Review of Large-Scale Artificial Ionospheric Modification*

### 2.1 Introduction

Ionospheric modification by high power radio waves originated with the first unintentional modification of the ionosphere in the early 1930s. Tellegen (1933) reported that the modulation of a high power radio transmitter in Luxembourg could be heard in the background of a programme transmitted from Beromünster and received at Eindhoven.

*“The modulation of the Luxembourg station could be heard on the background to such an intensity that during the weak passages of the programme of Beromünster the programme of Luxembourg was heard with annoying strength.”*

The effect was caused by the powerful Luxembourg transmitter modifying the radio propagation characteristics of the ionosphere. When the Beromünster signal passed through the modified region its propagation was affected by the modified ionospheric conditions, and in this way amplitude modulation from the Luxembourg signal was transferred to the Beromünster signal. Soon after this, scientists began to consider the prospect of intentional modification of the ionosphere. Bailey (1938) speculated that transmitting radio waves into the E-region at harmonics of the electron gyrofrequency could produce airglow to brighten the night sky. Later, Bailey (1959) suggested that utilising a high power radio wave close to the electron gyrofrequency could artificially increase the electron density in the ionosphere, facilitating radio communications

The early modification experiments were concerned with using high power radio waves to produce small changes in ionospheric properties, such as collision rates, and then investigating how this affected the propagation of low power diagnostic waves. From these experiments ionospheric heating developed. Here the high power radio wave was employed to produce large scale electron temperature enhancements. Showen (1972) found enhanced electron temperatures in measurements taken from the Arecibo incoherent scatter radar, when utilising a high power 40 MHz wave to modify the ionosphere. Experiments like this paved the way for modification facilities such as those at Platteville in Colorado, Arecibo in Puerto Rico, Tromsø in Norway, Sura in Russia and Fairbanks in Alaska.

This chapter presents an overview of the effects which have been observed during artificial modification experiments, with particular emphasis on heating of the auroral E-region. The production of artificial field aligned irregularities during heating is dealt with in chapter 3.

## 2.2 Plasma frequencies and gyrofrequencies

In a plasma, if the electrons are displaced by a small distance with respect to the ions the resulting motion is simple harmonic. The frequency of this motion is called the plasma frequency, and is given by

$$4\pi^2 f_n^2 = \frac{Ne^2}{\epsilon_0 m_e}, \quad (2.1)$$

where  $N$  is the electron density,  $e$  is the electronic charge,  $\epsilon_0$  is the permittivity of free space and  $m_e$  is the electron mass. The plasma frequency is an important quantity in radio wave heating of the ionosphere, as the radio wave is reflected when its frequency matches the plasma frequency. In addition, near the reflection point a strong interaction occurs between the radio wave and the plasma due to a resonance in the radio refractive index. This produces irregularities and an increased heating rate.

When a moving charged particle enters a region containing a magnetic field it describes a helical path. The motion parallel to the magnetic field is unaffected, whereas the motion perpendicular to the magnetic field produces a Lorentz force which causes the helical motion. The angular frequency of the particle is known as the angular cyclotron frequency or angular gyrofrequency. It has the form

$$\Omega = \frac{qB}{M}, \quad (2.2)$$

where  $q$  is the particle charge,  $B$  is the geomagnetic field and  $M$  is the particle mass. The gyroradius is the radius of the circle perpendicular to the magnetic field traced out by the moving particle. Due to their large mass, ions have a lower gyrofrequency than electrons, and therefore have a larger gyroradius for the same energy. The gyrofrequencies of ions and electrons are important quantities in many areas of ionospheric physics. For example, differences in ion and electron gyromotion and collision frequency are responsible for creating currents in the E-region, and diffusion rates are affected by the difference in electron and ion gyroradii.

### **2.3 Propagation of a radio wave in the ionosphere**

The radio refractive index is an important parameter in predicting the propagation of a radio wave through the ionosphere. The formula for the refractive index is often called the Appleton-Hartree formula (Budden, 1985). The equation has a number of forms, depending on the level of detail included. A simple version given by Davies (1990), when both collisions and magnetic effects are negligible, is

$$\mu^2 = 1 - k \frac{N}{f^2}, \quad (2.3)$$

where  $k$  is 80.5,  $N$  is the electrons per cubic metre, and  $f$  is the radio wave frequency in Hertz. For this simple case it can be seen that the refractive index decreases with increasing electron density, and it follows that the refractive index decreases up to the F-region peak where the electron density reaches a maximum. This means that the effect of the ionosphere on a radio wave increases as the wave propagates upwards. The refractive index depends inversely on the frequency of the radio wave, and this has implications for the choice of frequencies for waves transmitted through the ionosphere. Satellite communication systems, where it is important that the effect of the ionosphere is minimised, utilise frequencies far above the plasma frequency of the F-region peak to avoid refraction. In ionospheric modification experiments, where refraction within the ionosphere is desirable to produce a strong interaction, the frequency is chosen to produce reflection at the desired altitude. For HF coherent scatter radars, where a small amount of refraction is often utilised to bend the rays over the horizon, frequencies much higher than the peak plasma frequency are transmitted.

More information about the propagation of radio waves in the ionosphere can be gained by including the effects of collisions and the geomagnetic field in the Appleton-Hartree formula. Including collisions produces a complex refractive index, which means that the ionosphere becomes absorbing. Absorption effects are important in both modification experiments and HF communication systems. As might be expected, the ionosphere becomes more absorbing when the electron density is large. A high electron density in the D-region for example, can absorb a modifying radio wave before it reaches the higher ionospheric layers, reducing the effectiveness of certain experiments. However, high absorption is desirable in some experiments, where the absorption of the high power wave can produce significant heating in the lower ionosphere. Radio communication engineers need to “steer” the frequencies they utilise according to the prevailing ionospheric conditions. If the frequency is too low it is absorbed to an unacceptable level, if it is too high then it penetrates the ionosphere and will not be received on the ground.

## 2.4 O- and X-mode effects

Including the geomagnetic field in the derivation of the Appleton-Hartree formula gives rise to a quadratic term, the roots of which produce a bi-valued refractive index. The positive root leads to

$$X = 1, \tag{2.4}$$

and the negative root leads to

$$X = 1 - Y, \tag{2.5}$$

or

$$X = 1 + Y, \tag{2.6}$$

where

$$X = \frac{Ne^2}{\epsilon_0 m_e \omega^2}, \tag{2.7}$$

and

$$Y = \frac{eB}{m_e \omega}. \tag{2.8}$$

$\omega$  is the angular frequency of the electromagnetic wave. Equation 2.4 corresponds to a wave which reflects at the same height as it would without the influence of a magnetic field. For this reason the wave mode described by equation 2.4 is referred to as the ordinary or O-mode. Equations 2.5 and 2.6 describe the extraordinary or X-mode, this differs from the O-mode in that it has the opposite polarisation with respect to the geomagnetic field. In general, the parameter  $X$  increases with height up to a peak, so a wave propagating vertically will first encounter the  $X=1-Y$  level, where X-mode is reflected, and then the  $X=1$  level where the O-mode is reflected. In most cases, no energy reaches the  $X=1+Y$  level, since all the wave energy is reflected below this height. This rule is true at low and middle latitudes, but at high latitudes another mechanism is possible. The Z-mode (Mjølhus, 1990) results from the coupling of an O-mode into an X-mode wave at the  $X=1$  level, and gives reflection at the  $X=1+Y$  level.

The differing reflection points of O- and X-mode waves have a significant impact on artificial modification experiments. An important wave mode in the ionosphere is the electron acoustic wave mode, sometimes referred to as the Langmuir or plasma wave mode. By setting the k-vector in the electron acoustic dispersion relation to zero, it is possible to form the equation for the upper-hybrid frequency

$$\omega_u^2 = \omega_e^2 + \Omega_e^2, \quad (2.9)$$

where  $\omega_u$  is the upper-hybrid frequency,  $\omega_e$  is the angular plasma frequency and  $\Omega_e$  is the electron gyrofrequency. The upper-hybrid frequency has particular relevance to artificial modification experiments, because a resonance occurs where the radio wave frequency equals the upper-hybrid frequency (Hagfors, 1984). When this happens, mode conversion of the radio wave can take place to produce artificial plasma instabilities. As the plasma frequency is height dependent, the matching between the radio frequency and the upper hybrid frequency will occur at a specific height, the upper-hybrid height. This occurs when  $X=1-Y^2$ , and as  $Y$  is typically less than one, the upper-hybrid height occurs above the  $X=1-Y$  level where X-mode reflects and below the  $X=1$  level where O-mode reflects. This means that X-mode waves never reach the level where artificial instabilities are excited, and therefore only O-mode waves are utilised in experiments to excite instabilities. However, this is not necessarily a disadvantage and the contrasting properties of the two opposite polarisations can be useful in modification experiments. For instance, in D-region absorption experiments, X-mode is more readily absorbed than O-mode (Robinson, 1989), giving rise to larger heating effects. A typical modification campaign will utilise antenna arrays capable of producing either polarisation, depending on the experiment and the ionospheric conditions.

## 2.5 RF modification of the E-region

The E-region was the first ionospheric layer to be discovered, the 'E' standing for electrified. The ionosphere is horizontally stratified by gravity, and the E-region is generally considered to lie between 90 and 150 km above the ground, below lies the D-region and the F-region lies above. Within the D- and E-regions the neutral density is much higher than in the F-region, and as a consequence collision rates between charged particles and neutrals are high.

The D and E-regions provide the best starting point for modelling the effect of a high power radio wave propagating through the ionosphere. When a radio wave

has a frequency less than the plasma frequency of the ionospheric layer through which it is propagating, the propagation is underdense. Underdense propagation effects are easily modelled, as the effects can be calculated in a cumulative fashion as the wave propagates. In the ionosphere, the plasma frequency (which is dependent on the electron density) increases with height up to the F-region peak. When a radio wave propagating upwards reaches the point at which its frequency equals that of the plasma, the propagation is said to be overdense and the wave is reflected. At the reflection point a strong interaction occurs between the plasma and the wave which is difficult to model in a self-consistent way. This strong interaction manifests itself in non-straight line propagation of the radio wave and the production of artificial plasma instabilities. The plasma frequency is low in the D- and E-regions and so the more easily modelled underdense propagation is most likely in these layers. In addition to propagation effects, the collisional nature of the D- and E-regions means that plasma flowing out of the heated region need not be considered, which also makes modelling an easier task. The D- and E-regions also provide the opportunity to investigate the interaction of radio waves with a number of physical processes which only occur in these regions. For instance, a current system, known as the auroral electrojet, only occurs at E-region heights.

## 2.6 Theory of RF modification

The theory of RF modification has been extensively described in the literature (Gurevich, 1978; Tomko *et al.*, 1980; Meltz *et al.*, 1982; Milikh *et al.*, 1994). Consider the momentum balance equation for an electron acted on by an external electric field in the ionosphere. In the absence of the Earth's magnetic field we have

$$m_e \frac{dV_e}{dt} = -eE - m_e \nu_e V_e, \quad (2.10)$$

where  $\mathbf{E}$  is

$$\mathbf{E} = \mathbf{E}_0 e^{-i\omega t}. \quad (2.11)$$

$\mathbf{E}$  is the electric field due to the RF wave,  $\omega$  is the wave frequency,  $t$  is time,  $\nu_e$  is the electron neutral collision frequency,  $V_e$  is the electron flow speed,  $m_e$  is the electron mass and  $e$  is the electronic charge. The solution to this equation consists of a complimentary function which decays over time, and a particular integral which gives the steady state solution

$$\mathbf{V}_e = \frac{-\mathbf{E}e(v_e + i\omega)}{m_e(v_e^2 + \omega^2)}. \quad (2.12)$$

The heating rate due to an RF wave is given by

$$Q_{RF} = \langle \mathbf{E} \cdot \mathbf{J} \rangle, \quad (2.13)$$

where  $\mathbf{J}$ , the current density is given by

$$\mathbf{J} = N_e e \mathbf{V}_e. \quad (2.14)$$

Integrating over a period gives the steady state expression

$$Q_{RF} = \frac{N_e e^2 \mathbf{E}_0^2 v_e}{2m_e(v_e^2 + \omega^2)}, \quad (2.15)$$

where  $\mathbf{E}_0$  is the real electric field due to the RF wave,  $\omega$  is the wave frequency and  $e$  is the electronic charge. Including the effect of the Earth's magnetic field in the above calculation leads to  $\omega$  being replaced by  $\omega \pm \Omega_e$  where plus or minus refers to O- and X- mode respectively, and  $\Omega_e$  is the electron gyrofrequency.

## 2.7 The Farley-Buneman instability

HF modification experiments may produce electron temperature increases in the E-region of a few 100 K (Robinson *et al.*, 1995), but at auroral and equatorial latitudes natural heating effects occur which in some cases can produce far more significant changes.

At high latitudes and at heights of between 95 and 120 km, the ions are unmagnetized and the electrons are collisionless to zero order. Electric fields in this region can be as high as 100 mV/m and ExB drift causes the electrons to flow through the ions at up to 2000 ms<sup>-1</sup>. When the electron flow speed exceeds a certain threshold, enhanced electron temperatures can occur. This enhancement can be explained by a modified two-stream instability known as the Farley-Buneman (FB) instability.

The Farley-Buneman theory was developed by Farley (1963) using kinetic theory, and Buneman (1963) using a fluid based approach. The linear theory of the two-stream instability is outlined below.

The instability is caused by the differing responses of ions and electrons when acted upon by a combination of electric and magnetic fields in the electrojet region. We begin by considering the electron continuity equation

$$\frac{dn}{dt} + (\mathbf{V}_e \cdot \nabla n) + n(\nabla \cdot \mathbf{V}_e) = 0, \quad (2.16)$$

and the conservation of electron momentum

$$\left(\frac{-e}{m_e}\right)(\mathbf{E} + \mathbf{V}_e \times \mathbf{B}) - \left(\frac{k_B T_e}{m_e}\right)\left(\frac{\nabla n}{n}\right) - \nu_e \mathbf{V}_e = 0. \quad (2.17)$$

$n$  is the electron density,  $\mathbf{E}$  is the applied electric field,  $\mathbf{B}$  is the geomagnetic field strength,  $k_B$  is Boltzmann's constant,  $m_e$  is the electron mass,  $T_e$  is the electron temperature,  $\nu_e$  is the electron-neutral collision frequency and  $\mathbf{V}_e$  is the electron velocity. The first term in the momentum equation is due to the action of electric and magnetic fields on a moving charged particle, the second term is a pressure term and the third term is due to collisions.

The ion continuity and momentum balance equations have a similar form, the main difference being that the ions are assumed to be at rest to zero order. By expressing the electron momentum balance equation in component form to create two equations, and by utilising the electron continuity equation and the two ion equations, it is possible to form a 5 by 5 determinant. By evaluating the determinant and simplifying we get

$$(\omega - kV_e) = \left(\frac{-\psi_0}{\nu_i}\right) [\omega(i\omega + \nu_i) - ik^2 C_s^2], \quad (2.18)$$

where

$$\psi_0 = \frac{\nu_e \nu_i}{\Omega_e \Omega_i}, \quad (2.19)$$

and

$$C_s^2 = k_B \frac{(T_e + T_i)}{m_i}. \quad (2.20)$$

If we now allow the frequency of the perturbation to be complex,  $\omega = \omega_1 - i\gamma$ , then the imaginary term represents growth or decay, and the real part represents the oscillatory motion. The waves will grow when  $\gamma$  is positive, this happens when

$$\omega_1^2 > k^2 C_s^2. \quad (2.21)$$

This inequality can be re-written as

$$V_e > (1 + \psi_0) C_s. \quad (2.22)$$

The instability is excited at heights around 100 km, where  $\psi_0$  is small, around 0.1, so the inequality can be simplified to say that the electrons must drift through the ions with a velocity greater than the sound speed,  $C_s$ .

At 100 km,  $\psi_0$  is typically 0.1 and  $C_s$  is  $400 \text{ ms}^{-1}$ . This gives a threshold flow speed of about  $440 \text{ ms}^{-1}$ . When this flow speed is exceeded, the growth rate for the waves is positive and the instability grows.

When the instability is excited and Farley-Buneman waves are formed, wave drag produces frictional heating of the electrons. This heating takes the form (Robinson, 1994)

$$Q_w = N_e m_e v^* (V_D - c)^2, \quad (2.23)$$

where the anomalous collision frequency  $v^*$  is given by

$$v^* = \frac{\Omega_i \Omega_e}{\nu_i} \left( \frac{V_D - c}{C_s} \right) - \nu_e. \quad (2.24)$$

$N_e$  is the electron density,  $m_e$  is the electron mass,  $\Omega_i$  is the ion gyrofrequency,  $C_s$  is the ion acoustic speed,  $\nu_i$  is the ion-neutral collision frequency,  $V_D$  is the electron drift speed and  $c$  is the wave phase speed.  $c$  and the ion acoustic speed are equal in the rest frame of the ions. The collision frequency term is referred to as anomalous because it is not concerned with electron-neutral collisions, but with the interaction of the Farley-Buneman waves with the electrons. The name collision frequency is retained because of the analogy between particle scattering by wave turbulence, and classical collisions which involve particle-particle scattering.

## 2.8 Other heating and loss processes

Besides the terms already mentioned, there is a small amount of frictional heating between electrons and neutrals in the electrojet (Robinson, 1986)

$$Q_{en} = N_e m_e v_e V_D^2. \quad (2.25)$$

There are also energy loss processes which act to cool the electrons. (Schunk and Nagy, 1978). These consist of a variety of different mechanisms involving the transfer of energy from the electrons to ion and neutral species. The energy loss rate is dependent on the number density of the ion or neutral species and the electron and neutral temperatures. The loss rates take the form (Schunk and Nagy, 1978)

$$Q_{N_2,rot} = \frac{2.9 \times 10^{-14} N(N_2)(T_e - T_n)}{T_e^{0.5}}, \quad (2.26)$$

$$Q_{O_2,rot} = \frac{6.9 \times 10^{-14} N(O_2)(T_e - T_n)}{T_e^{0.5}}, \quad (2.27)$$

$$z = 5 + 3 \exp\left(\frac{-228}{T_n}\right) + \exp\left(\frac{-326}{T_n}\right), \quad (2.28a)$$

$$Dx_1 = \exp\left(\frac{-228}{T_n}\right), Dx_2 = \exp\left(\frac{-326}{T_n}\right), Dx_3 = Dx_2, \quad (2.28b)$$

$$Ex_1 = \exp\left(\frac{-228}{T_e}\right), Ex_2 = \exp\left(\frac{-326}{T_e}\right), Ex_3 = \exp\left(\frac{-98}{T_e} - \frac{228}{T_e}\right), \quad (2.28c)$$

$$Ee_1 = 228, Ee_2 = 326, Ee_3 = 98, \quad (2.28d)$$

$$Ep_1 = 0.02, Ep_2 = 0.028, Ep_3 = 0.008, \quad (2.28e)$$

$$A_1 = 8.58 \times 10^{-6}, A_2 = 7.201 \times 10^{-6}, A_3 = 2.463 \times 10^{-7}, \quad (2.28f)$$

$$Be_1 = 1.019, Be_2 = 0.8998, Be_3 = 1.268, \quad (2.28g)$$

$$Bfac_1 = 1.008, Bfac_2 = 0.9617, Bfac_3 = 1.1448, \quad (2.28h)$$

$$Q_{O_{fine}} = \sum_{j=1}^3 \frac{8.629 \times 10^{-6} N(O) A_j B_{fac_j} T_e^{(B_{e_j}-0.5)}}{Z} \times \left[ E p_j (D x_j - E x_j) + 5.91 \times 10^{-9}, \right. \\ \left. \times \left\{ (1 + B_{e_j}) D x_j + E x_j \left[ \frac{E e_j}{T_e} + 1 + B_{e_j} \right] \right\} \right] \quad (2.28i)$$

$$F = 1.06 \times 10^4 + 7.51 \times 10^3 \tanh(1.10 \times 10^{-3} (T_e - 1800)), \quad (2.29a)$$

$$G = 3300 + 1.233(T_e - 1000) - 2.056 \times 10^{-4} (T_e - 1000)(T_e - 4000), \quad (2.29b)$$

$$Q_{N_2,vib} = -2.99 \times 10^{-12} N(N_2) \exp \left[ \frac{F(T_e - 2000)}{2000 T_e} \exp \left( \frac{-G(T_e - T_n)}{T_e T_n} \right) - 1 \right]. \quad (2.29c)$$

The above rates represent the rotational excitation of  $N_2$  and  $O_2$ , the fine structure excitation of  $O$  and the vibrational excitation of  $N_2$ , respectively. These four rates are those deemed most significant by Tomko *et al.* (1980), and these authors utilised these rates in their model of a radio wave propagating through the ionosphere. In addition to these rates, Schunk and Nagy (1978) describe the following loss processes

$$H = 3300 - 839 \sin(1.91 \times 10^{-4} (T_e - 2700)), \quad (2.30a)$$

$$Q_{O_2,vib} = -5.196 \times 10^{-13} N(O_2) \exp \left( \frac{H(T_e - 700)}{700 T_e} \right) \left( \exp \left( \frac{-2770(T_e - T_n)}{T_e T_n} \right) - 1 \right), \quad (2.30b)$$

$$D = 2.4 \times 10^4 + 0.3(T_e - 1500) - 1.947 \times 10^{-5} (T_e - 1500)(T_e - 4000), \quad (2.31)$$

$$Q_{O_{elec}} = -1.57 \times 10^{-12} N(O) \exp \left( \frac{D(T_e - 3000)}{3000 T_e} \right) \left[ \exp \left( \frac{-22713(T_e - T_n)}{T_e T_n} \right) - 1 \right], \quad (2.31b)$$

$$Q_{N_2,elastic} = 1.77 \times 10^{-19} N(N_2) (1 - 1.21 \times 10^{-4} T_e) T_e (T_e - T_n), \quad (2.32)$$

$$Q_{O_2,elastic} = 1.21 \times 10^{-18} N(O_2) (1 + 3.6 \times 10^{-2} T_e^{0.5}) T_e^{0.5} (T_e - T_n), \quad (2.33)$$

$$Q_{O,elastic} = 7.9 \times 10^{-19} N(O) (1 + 5.7 \times 10^{-4} T_e) T_e^{0.5} (T_e - T_n), \quad (2.34)$$

$$Q_{\text{Heelastic}} = 2.46 \times 10^{-17} N(\text{He}) T_e^{0.5} (T_e - T_n), \quad (2.35)$$

$$Q_{\text{Helastic}} = 9.63 \times 10^{-16} N(\text{H}) (1 - 1.35 \times 10^{-4} T_e) T_e^{0.5} (T_e - T_n), \quad (2.36)$$

The loss rates,  $Q$ , are in  $\text{eVs}^{-1}$ ,  $N(x)$  is the density of species  $x$  in  $\text{cm}^{-3}$ ,  $T_e$  and  $T_n$  are the electron and neutral temperatures respectively. Equations 2.30-2.36 represent the vibrational excitation of  $\text{O}_2$ , electronic excitation of  $\text{O}$ , and elastic collisions with  $\text{N}_2$ ,  $\text{O}_2$ ,  $\text{O}$ ,  $\text{He}$ , and  $\text{H}$ . The mechanisms have a variety of functional forms, but all increase with increasing electron and neutral temperature. The various loss rates become significant under specific conditions and at different altitudes in the ionosphere. For example, the vibrational excitation of  $\text{N}_2$  is an important sink only for electron temperatures above 1500 K, and the vibrational excitation of  $\text{O}_2$  is most significant in the E-region.

The terms describing heating and cooling processes can be combined to produce an overall expression describing the energy sources and sinks for electrons in the ionosphere. Assuming a balance between the various heating and loss processes we find

$$Q_{\text{RF}} + Q_w^* + Q_{en} - \text{LOSS} = 0. \quad (2.37)$$

Equation 2.37 is the basis for producing a model of RF heating in the ionosphere. The various terms are electron temperature dependent, and an iterative method can be utilised to determine the optimum temperature for a particular point in the ionosphere.

## 2.9 Artificial heating of E-region irregularities

In the above analysis, heating rates due to RF heating and Farley-Buneman wave heating have been described. These rates are valid when the RF heating is underdense, but when the frequency of the RF wave is close to the plasma frequency, and the RF electric field is large, the RF wave will directly affect the instability, producing a modified wave heating rate.

Sharma (1989) discusses the direct effect of an RF wave on a natural gradient drift instability in the equatorial electrojet. This author considers the coupling of a low-frequency mode  $(\omega, k)$  to a high amplitude electrostatic pump wave  $(\omega_0, k_0)$  and two high frequency sidebands  $(\omega_{1,2}, k_{1,2})$ . The high power electrostatic pump wave is produced by mode conversion of the transmitted radio wave. The electrostatic mode has a higher amplitude than the electromagnetic wave, even at

low levels of mode conversion, and is therefore more likely to produce a strong effect. The pump and the sidebands heat the electrons with a component given by Sharma (1989) as

$$-\frac{e}{2}(\mathbf{E}_0 \cdot \mathbf{v}_1 + \mathbf{v}_0 \cdot \mathbf{E}_1 + \mathbf{E}_0^* \cdot \mathbf{v}_2 + \mathbf{E}_2 \cdot \mathbf{v}_0^*), \quad (2.38)$$

where  $\mathbf{E}$  represents electric field and  $\mathbf{v}$  represents the linear response of the electrons to the high-frequency fields, and is proportional to the corresponding wave number. The starred terms are complex conjugates. When the RF pump is turned on, the growth rate of the instability tends to be increased, leading to an increase in the fluctuation level.

Other instabilities can be directly affected by an RF wave, but the effect is not necessarily to increase the fluctuation level. For the case described by Robinson (1994), the RF wave reduces the heating due to the FB instability and the overall effect is a reduction in the heating efficiency of the RF wave. It is also possible for the RF wave to completely shut off the heating due to the instability. When this happens, the overall effect of turning on the heater is actually a reduction in electron temperature. This is because  $Q_{RF}$  is not enough to make up for the heating lost by shutting off the instability.

Chaturvedi and Ossakow (1990) identify a number of E-region instabilities which may be directly affected by a high power radio wave. As described above, the Farley-Buneman instability is excited at high-latitudes at around 110 km altitude, during times when the electron drift speed exceeds the sound speed. In regions where the ionosphere is stable to this instability, an energy contribution from another source, such as a high power radio wave, may produce favourable conditions for the onset of the instability. Hoeg *et al.* (1986) describe an E-region modification experiment diagnosed by the STARE coherent radar. These authors observed artificial two-stream-like irregularities during times of natural Farley-Buneman activity.

The gradient drift instability may be excited at electron drift velocities below the threshold of the Farley-Buneman instability. The instability has a characteristic growth time of order tens of seconds, and has been suggested as a possible mechanism when growth times of this order have been observed during E-region modification experiments (Hoeg *et al.* 1986; Djuth *et al.*, 1985). The gradient drift instability linearly generates irregularities of order 100s of metres, which may then nonlinearly generate metre-scale irregularities which are visible to coherent radars. Chaturvedi and Ossakow (1990) suggest that the combination of a natural electric field of 10 mV/m and an artificial RF wave of 15 mV/m, easily achieved in recent modification experiments, is enough to excite the gradient drift instability. At higher

altitudes, where the electrojet is less significant, a higher artificial electric field may be required. However, there is another mechanism which may be responsible for the generation of slow-growth-time irregularities outside the electrojet region. Chaturvedi and Ossakow (1990) suggest that at high latitudes, and outside the electrojet region, the presence of field aligned currents may interact with the pump wave to produce a gradient instability known as the current convective instability. These authors also suggest that a high power pump may be able to directly generate metre-scale irregularities by exciting the ion acoustic and electrostatic ion cyclotron instabilities.

Schlegel *et al.* (1987) observed artificial modification in the E-region with the EISCAT UHF radar. These authors found that the observed backscatter power could not be explained by the normal incoherent scatter process. They did not find a correlation between the excitation of the unstable waves and the background electric field, and concluded that the unstable waves were probably produced by direct conversion of the artificial HF wave.

## 2.10 Previous modelling studies

Tomko *et al.* (1980) produced a computer code to model the effect of a high power radio wave propagating through the ionospheric D-region. These authors considered an HF wave propagating upwards, which was absorbed as it passed through the ionosphere. The radio wave provided an additional source of energy in the electron energy balance equation, and by considering temperature dependent cooling rates, the authors were able to calculate modified values for electron temperature due to the artificial wave. The authors found that a high power radio wave could increase the D-region electron temperature by almost a factor of ten (Fig. 2.1a). This occurred because the low electron density in the D-region meant that only a small amount of RF energy was required to give a large increase in electron temperature.

Meltz *et al.* (1982) performed a similar calculation to that of Tomko *et al.* (1980) to model the effects of artificial modification experiments at Platteville, Colorado. These authors found a similar increase in D-region electron temperature, and also presented graphs of the artificial change in electron density. The electron density was modified by a change in electron temperature, due to the effect of temperature dependent recombination rates. Meltz *et al.* (1982) found that the electron density was reduced below 80 km, and was increased by up to 70 % above 80 km.

More recently, Milikh *et al.* (1994) have utilised calculations similar to those of Tomko *et al.* (1980) and Meltz *et al.* (1982) in order to estimate the expected performance of the new HF Active Auroral Research Program (HAARP) facility in

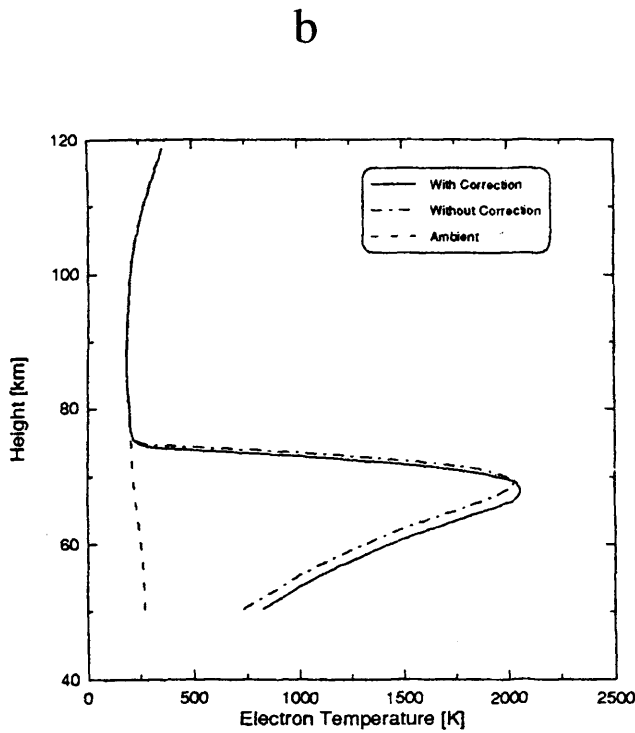
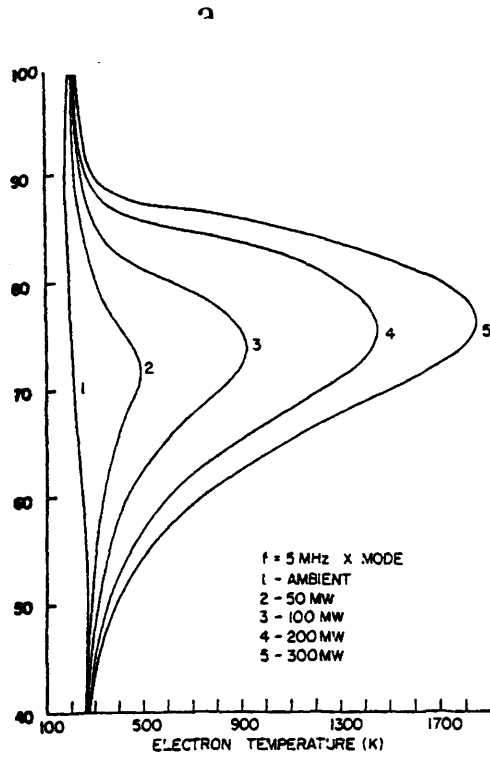


**Figure 2.1.** a) Model electron temperature profiles for various heating powers (after Tomko *et al.*, 1980). b) Model electron temperature profiles for a heater ERP of 95 dB W and a frequency of 3 MHz (after Milikh *et al.*, 1994).

Fairbanks, Alaska. These authors introduced a kinetic correction factor in order to achieve a more accurate picture of the heating effect of the wave although this only modified the resulting profiles slightly (Fig 2.1b).

### 2.11 Electron temperature modification

Heater induced electron temperature changes were first reported by Gordon *et al.*, (1971) and Gordon and Carlson (1974). These experiments were performed at Arecibo, where an incoherent scatter radar facilitated direct measurement of the temperature enhancement. Gordon and Carlson (1974) superimposed a number of heater cycles, in order to clearly show the response to heating, and found an electron temperature increase of around 200 K. These early studies were followed by attempts to measure the heating and cooling responses of the ionosphere (Meltz *et al.*, 1974; Gurevich, 1978; Mantas *et al.*, 1981). These authors typically found response times of 10s.of seconds for both growth and decay.

The EISCAT incoherent scatter system in northern Norway has been employed to measure artificial temperature enhancements in a number of experimental campaigns (Jones *et al.*, 1986; Stocker *et al.*, 1992; Robinson 1989; Robinson *et al.*, 1996; Robinson *et al.*, 1997). Robinson 1989 reported EISCAT observations of heater induced electron temperature enhancements. During a heating campaign in 1985, enhancements of around 400 K were observed at 202 km, close to the reflection point, and enhancements of around 200 K were observed at 256 km (Fig. 2.2a). The 1985 results correspond to a percentage increase of around 10 %, and a further campaign in 1987 found peak increases of around 40 % (Robinson, 1989). This difference could be due to solar cycle variation, and differences in electron temperature enhancement tend to be a feature of successive heating campaigns. Djuth *et al.*, (1987) observed a 150 % enhancement in the nighttime electron temperature over Arecibo. These observations have been attributed to low cooling rates (Newman *et al.*, 1988).

Most investigations of heater induced electron temperature enhancement have focused on studies of the F-region, with relatively few E-region studies. Robinson *et al.* (1995) presented results in which the EISCAT UHF radar was utilised to measure the E-region electron temperature response above Tromsø during a variety of electrojet conditions. These authors observed a tendency for larger increases in electron temperature to occur during periods of lower electron drift (Fig. 2.2b). The results provide support for the view presented by Robinson (1994), that Farley-Buneman heating plays a significant role in the electrojet response to RF heating.

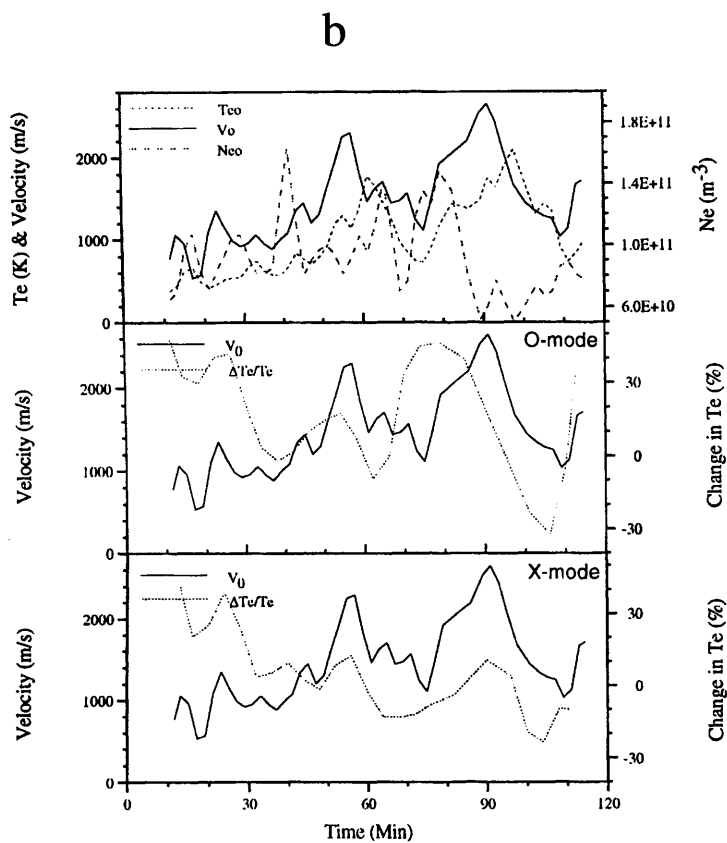
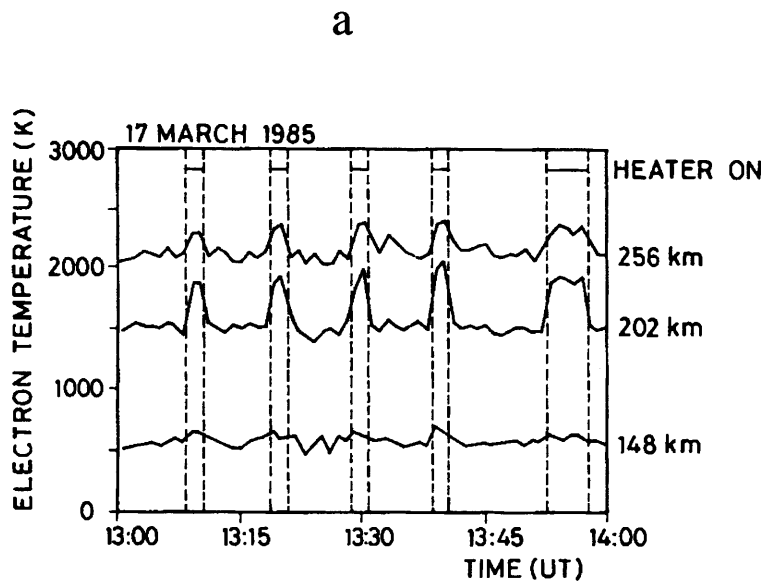


**Figure 2.2.** a) Electron temperature enhancements measured by EISCAT at 3 different altitudes, on March 17, 1985, during heating at 4.544 MHz. (after Robinson, 1989). b) (Top) electron drift speed, temperature and density as a function of time, in the E-region during heater-off periods. (Centre) Fractional increase in electron temperature during O-mode heating. (Bottom) As central panel but for X-mode heating (After Robinson *et al.*, 1995).

## 2.12 Electron density modification

Consider the following equation for the change in electron density

$$\frac{dN_e}{dt} + N_e \nabla \cdot \mathbf{V} = q_n - l_n. \quad (2.39)$$

$\frac{dN_e}{dt}$  is the rate of change in electron density.  $N_e \nabla \cdot \mathbf{V}$  is the change due to transport effects, and this can be ignored in the D and E-regions.  $q_n$  and  $l_n$  are the production and loss rates respectively. When there is balance between these terms, the change in density is zero and production equals loss. The production rate is controlled by solar radiation and is not affected by the RF wave, but the loss rate is temperature dependant, and is affected by RF heating. The loss rate is given by

$$l_n = \alpha N_e^2, \quad (2.40)$$

where  $\alpha$  is the recombination rate. This rate is temperature dependant and depends on the ion species present, (Bailey and Sellek, 1990).

Experimental and theoretical investigations of heater induced density changes have been undertaken for a variety of ionospheric conditions. The observed changes in density depend on the ion composition and the time of day of the measurements, and consequently, many different density effects have been reported. Meltz *et al.* (1974), solved equations for continuity and momentum, and predicted a density depletion of about 3 % near the reflection point. Gurevich (1978) also predicted density depletion. Observation of density depletions have been reported by Utlaut and Violette (1972), who found 7 % depletion at Platteville. Measurements at Arecibo have predominantly revealed density depletions of a few percent (Djuth *et al.*, 1987).

Density enhancements have been observed by Jones *et al.* (1982) and Robinson (1989). Jones *et al.* (1982) measured the change in phase in a low power diagnostic wave, which varied due to the plasma refractive index dependence on electron density. Growth and decay times of approximately 40s were reported. Robinson (1989) reported changes in the EISCAT power profile, which indicated an electron density enhancement of a few tens of percent.

## 2.13 Concluding remarks

This review highlights the bulk ionospheric effects of heating the ionosphere with high power radio waves, with particular emphasis on modification of the auroral E-

region. The currents which flow at around 100 km altitude to form the electrojet make the auroral E-region an interesting subject for study in its own right. Natural turbulence is produced when the electron flow speed is high, creating natural turbulent heating. This combines with artificial heating both indirectly, as an additional heat source, and directly, in an interaction between the high power wave and the Farley-Buneman instability. The results of an experimental campaign in which the auroral E-region was heated under a variety of natural conditions, are presented in chapter 5. A model of an RF wave propagating through the auroral D- and E-regions is also presented in chapter 5.

## **Chapter 3**

# ***Review of Previous Work on Artificial Field Aligned Irregularities***

### **3.1 Introduction**

When high power radio waves, operating in ordinary polarisation, are beamed vertically and at an angle within a few tens of degrees of the geomagnetic field, they strongly excite plasma density irregularities in regions where the wave frequency is close to the local upper-hybrid frequency (Stubbe *et al.*, 1982; Robinson, 1989 and references therein). These plasma irregularities are highly elongated in the direction of the geomagnetic field, as a consequence of the highly anisotropic nature of electron transport in the ionosphere.

The special issue of Radio Science (November 1974) describes the first experiments made with the Platteville ionospheric modification facility (or heater) in Colorado. Early theories (e.g. Bailey 1938) suggested that experiments of this kind would produce electron density and temperature changes, but did not predict additional processes which were observed in the early experiments at Platteville. The observations, including scatter from field aligned irregularities, absorption of diagnostic waves and artificial spread-F, were indicative of another type of phenomena, that of nonlinear excitation of instabilities in the plasma. Subsequent theoretical work has focused on explaining the observations associated with these nonlinear effects.

### **3.2 Parametric instabilities**

In a tuned circuit, it is possible to excite the natural oscillations by varying the capacitance or inductance at twice the natural frequency of the circuit. In such a circuit, termed a parametric oscillator, the high amplitude input frequency is known as the pump, and the natural oscillations will grow if the pump exceeds the power dissipated in the circuit. In the ionosphere, the nonlinear properties of the medium make it possible to transfer energy from a high power wave (the pump) to weaker waves, which will grow if the transferred power exceeds the dissipation. This analogy between tuned circuits and high power waves in the ionosphere has led to the term parametric being used to describe a plasma instability excited by an oscillating electric field.

Three wave interactions can occur in the ionosphere which give rise to parametric instabilities. A strong wave (the pump, wave 0) decays into two weaker

waves (waves 1 and 2) according to matching conditions in wave number ( $k$ ) and angular frequency ( $\omega$ ).

$$\omega_0 = \omega_1 + \omega_2 \quad \mathbf{k}_0 = \mathbf{k}_1 + \mathbf{k}_2. \quad (3.1)$$

The strong pump wave is a high frequency electromagnetic wave (the transmitted radio wave). This wave undergoes a nonlinear interaction through the pondermotive force with a weak high frequency wave, which is initially present as noise. This interaction produces a force on the electrons, giving rise to a low frequency wave. The weak high frequency wave is due to the pump wave scattering from the density perturbations of the low frequency wave.

Three parametric processes have been identified as significant in ionospheric experiments. In each case, wave 0 is the transmitted electromagnetic wave. In stimulated Brillouin scattering, wave 1 is another electromagnetic wave, and wave 2 is an ion acoustic wave. In stimulated Raman scattering, wave 1 is again an electromagnetic wave and wave 2 is a langmuir wave. In the parametric decay instability, wave 1 is a Langmuir wave and wave 2 is an ion acoustic wave.

For typical ionospheric parameters the threshold electric field for the parametric decay instability is around  $0.1 \text{ Vm}^{-1}$  (Stubbe and Kopka 1981). This electric field is easily within reach of heating facilities such as EISCAT, and the parametric decay instability or PDI is certainly excited during ionospheric modification. The plasma waves produced during excitation of the PDI can be detected by an incoherent scatter radar. The artificially stimulated Langmuir wave appears in the returned spectrum as an echo offset from the radar frequency by the heater frequency minus the ion-acoustic frequency. The ion-acoustic wave appears as an enhanced line in the normal ion line spectrum. However, there is a problem in interpreting the PDI as the mechanism for the production of artificial field aligned irregularities. The PDI has a growth time of order milliseconds, and so it does not explain why field aligned irregularities are excited with a growth time of seconds. The fast saturation of the PDI is due to the pondermotive force. Thermal effects act more slowly and this is considered in another instability mechanism, the thermal parametric instability or TPI.

### **3.3 The thermal parametric instability**

Following the discussion in Robinson (1989), consider a periodic number density given by

$$n_2 = n_{20} e^{-ik_2 z}, \quad (3.2)$$

where  $\xi$  is in the direction perpendicular to the geomagnetic field. A high power radio wave has an electric field given by

$$\mathbf{E}_0 = \mathbf{E}_{00} e^{-i\omega_0 t} \quad (3.3)$$

An interaction occurs between the high power EM wave and the density perturbations to produce a periodic current density, which in turn generates a Langmuir wave with a periodic electric field,  $\mathbf{E}_1(\omega_0, \mathbf{k}_2)$ . The three wave matching condition (equation 3.1) also applies to the TPI. The wave number of the high power radio wave is negligible compared to the wave number of the density perturbation, so  $\mathbf{k}_0 = 0$  and the wave number of the Langmuir wave is given by the wave number of the density perturbation. The density perturbation is not time varying, and so  $\omega_2 = 0$ , and the frequency of the Langmuir wave is the same as that of the EM wave. So the matching conditions are

$$\omega_0 = \omega_1 + \omega_2 \Rightarrow \omega_0 = \omega_1 + 0, \quad (3.4)$$

and

$$\mathbf{k}_0 = \mathbf{k}_1 + \mathbf{k}_2 \Rightarrow 0 = \mathbf{k}_1 + \mathbf{k}_2 \Rightarrow \mathbf{k}_1 = -\mathbf{k}_2. \quad (3.5)$$

The density perturbation is enhanced by the interference between the electric fields of the high power EM wave and the Langmuir wave. The electric field density is proportional to

$$|\mathbf{E}_0 + \mathbf{E}_1|^2 \equiv |\mathbf{E}_0|^2 + 2|\mathbf{E}_0 \cdot \mathbf{E}_1| + |\mathbf{E}_1|^2. \quad (3.6)$$

The first term is the collisional heating term due to the EM wave. The second term is a zero frequency term which is periodic in space with wave number  $\mathbf{k}_2$ , it therefore matches the FAI periodicity and can cause enhancement. The third term represents energy dissipated to the Langmuir wave, and accounts for the anomalous absorption of EM waves. The heat input into the FAI, through simply considering the interference of waves 0 and 1, is zero. However, if the fact that the pump can form a standing wave pattern below its reflection height is taken into account, then net heating can occur. A density perturbation is associated with the temperature change brought about by the heating. The linear threshold electric field to excite the instability is given by Robinson (1989)

$$E_i = \frac{2.44(T_{eo}k_B)^2 \omega_0^2 k_2 e^{-\frac{2\nu H}{c}} \cos \theta}{\nu \Omega_e e^2 H}. \quad (3.7)$$

$k_B$  is Boltzmann's constant,  $\theta$  is the angle of the heater beam to the geomagnetic field,  $H$  is the scale height,  $\omega_0$  is the angular frequency of the heater wave,  $T_{eo}$  is the undisturbed electron temperature,  $\nu$  is the electron-neutral collision frequency,  $e$  is the electronic charge,  $k_2$  is the wave number of the FAIs,  $c$  is the speed of light and  $\Omega_e$  is the electron gyro frequency.

The above discussion only considers the primary Langmuir wave produced by scattering of the EM wave. Secondary Langmuir waves can be produced from scattering of the primary Langmuir wave. Inhester *et al.* (1981) suggest a mechanism which may increase the efficiency of the HF heating under certain conditions, through multiple scattering of plasma waves. The threshold electric field for this mechanism is nonlinear, it depends on the initial FAI amplitude. This could produce a two stage excitation, in which a linear growth mechanism enhances FAI amplitude until the nonlinear threshold is reached. The threshold electric field for a mechanism of this type would be determined by the threshold of the initial linear growth. Both the TPI (Robinson, 1989) and coupling of parametric decay instability waves (Coster *et al.*, 1985) have been suggested as candidates for this initial phase.

### 3.4 Theory of FAI decay

Electromagnetic heating of the ionospheric plasma can cause fluctuations to grow to amplitudes much greater than the thermal level. Coherent scatter from these fluctuations can be detected if the transmitted radar wavelength is twice that of the ionospheric irregularities, and the radar beam is orthogonal to the irregularities. Ionospheric fluctuations are typically aligned along the geomagnetic field, and so it is important for coherent scatter radar beams to achieve orthogonality with the magnetic field. At auroral latitudes the radar must be located several hundred kilometres away from the region of interest, and to make observations in the F-region it is necessary to make use of an HF radar beam, which undergoes refraction to achieve orthogonality.

The backscatter power received by an HF radar is proportional to the square of the density perturbation from which the radar beam is being scattered.

$$P = constant \times \Delta N^2, \quad (3.8)$$

where  $P$  is the linear power received by the radar,  $\Delta N$  is the ionospheric density perturbation at the frequency isolated by the radar and *constant* is a constant of proportionality which will depend on a number of parameters, including electron density and the radar cross-section. After the heater is turned off, the irregularities will decay. If the data indicate that a two stage decay process is involved (Minkoff and Kreppel, 1976; Belenov *et al.*, 1977; Hysell *et al.*, 1996), then this can be expressed by

$$\Delta N = Ae^{-\frac{t}{\tau_1}} + Be^{-\frac{t}{\tau_2}}. \quad (3.9)$$

From equation 3.8, power is proportional to the square of the irregularity amplitude. The decay of the irregularities can be treated as 2 separate regimes if the two time constants in equation 3.9 are sufficiently different, and so the power returned to the radar will have the form

$$P = \text{constant} \times \Delta N^2 \propto Ae^{-\frac{2t}{\tau_1}} + Be^{-\frac{2t}{\tau_2}}. \quad (3.10)$$

If the sum of 2 exponential functions is fitted to the decay curve of the returned power, so that

$$P = A'e^{-\frac{t}{\tau_1}} + B'e^{-\frac{t}{\tau_2}}, \quad (3.11)$$

then the time constants corresponding to the decay of the irregularities will be given by

$$\begin{aligned} \tau_1 &\approx 2\tau_1 \\ \tau_2 &\approx 2\tau_2 \end{aligned} \quad (3.12)$$

Once a dual time constant regime has been identified in the data, the next step is to explain the nature of the decay in terms of plasma diffusion along and across the geomagnetic field. The equations of motion, perpendicular to a magnetic field  $B_z$ , for a species  $j$  can be written (Kelley, 1989)

$$0 = -KT_j \frac{\partial n_j}{\partial x} + n_j q_j E_x + n_j q_j V_{jy} B_z - n_j M_j v_j V_{jx}, \quad (3.13)$$

$$0 = -KT_j \frac{\partial n_j}{\partial y} + n_j q_j E_y - n_j q_j V_{jx} B_z - n_j M_j v_j V_{jy}, \quad (3.14)$$

where  $K$  is Boltzmann's constant,  $q_j$  is the charge on each particle,  $E_y$  is the electric field,  $n_j$  is the number density,  $M_j$  is the mass and  $V_j$  is the velocity. The first term in each equation is due to pressure, the second term is due to electric fields, the third term is due to the magnetic field and the last term is due to collisions. Effects due to gravity and neutral winds are ignored. By substituting for  $V_{jy}$  in the first equation an expression involving only  $V_{jx}$  can be derived

$$V_{jx} \left( 1 + \frac{q_j^2 B_z^2}{M_j^2 v_j^2} \right) = \frac{-KT_j}{M_j v_j n_j} \frac{\partial n_j}{\partial x} + \frac{q_j}{M_j v_j} E_x - \frac{q_j B_z K T_j}{M_j^2 v_j^2} \frac{\partial n_j}{\partial y} + \frac{q_j^2 B_z^2}{M_j^2 v_j^2} E_y, \quad (3.15)$$

$$V_{jy} \left( 1 + \frac{q_j^2 B_z^2}{M_j^2 v_j^2} \right) = \frac{-KT_j}{M_j v_j n_j} \frac{\partial n_j}{\partial y} + \frac{q_j}{M_j v_j} E_y + \frac{q_j B_z K T_j}{M_j^2 v_j^2} \frac{\partial n_j}{\partial x} + \frac{q_j^2 B_z^2}{M_j^2 v_j^2} E_x. \quad (3.16)$$

The  $\mathbf{ExB}$  and diamagnetic drift velocities can be written

$$\begin{aligned} \mathbf{V}_{Ej} &= \frac{\mathbf{ExB}}{B^2} \\ \mathbf{V}_{Dj} &= \frac{-KT_j}{q_j B_z^2 n_j} \nabla n_j \times \mathbf{B}. \end{aligned} \quad (3.17)$$

By substituting for the  $\mathbf{ExB}$  and diamagnetic drift velocities, equations 3.15 and 3.17 can be combined to give an expression for the velocity of a species perpendicular to the magnetic field

$$\mathbf{V}_{j\perp} \left( 1 + \frac{q_j^2 B^2}{M_j^2 v_j^2} \right) = \frac{-KT_j}{M_j v_j n_j} \nabla_{\perp} n_j + \frac{q_j}{M_j v_j} \mathbf{E}_{\perp} + \frac{q_j^2 B^2 K T_j}{M_j^2 v_j^2} \mathbf{V}_{Dj} + \frac{q_j^2 B_z^2}{M_j^2 v_j^2} \mathbf{V}_{Ej}. \quad (3.18)$$

The first term on the right hand side of equation 3.18 is the contribution to the perpendicular velocity from motion antiparallel to the density gradient.

$$\mathbf{V}_{grad} \left( 1 + \frac{q_j^2 B^2}{M_j^2 v_j^2} \right) = \frac{-KT_j}{M_j v_j n_j} \nabla_{\perp} n_j. \quad (3.19)$$

Applying equation 3.19 to ions and electrons and adding gives

$$\mathbf{V}_{grad} \left( M_e v_e + \frac{q_e^2 B^2}{M_e v_e} + M_i v_i + \frac{q_i^2 B^2}{M_i v_i} \right) = \frac{-K(T_e + T_i)}{n} \nabla_{\perp} n. \quad (3.20)$$

The perpendicular diffusion coefficient for motion antiparallel to a density gradient can be defined by an expression of the form

$$\mathbf{V}_{grad} = -D_{\perp} \frac{\nabla_{\perp} n}{n}. \quad (3.21)$$

Substituting equation 3.20 into 3.21 gives a plasma diffusion constant

$$\frac{1}{D_{\perp}} = \frac{M_e v_e \left(1 + \frac{\Omega_e^2}{v_e^2}\right)}{K(T_e + T_i)} + \frac{M_i v_i \left(1 + \frac{\Omega_i^2}{v_i^2}\right)}{K(T_e + T_i)}. \quad (3.22)$$

The first term in equation 3.22 is due to electron diffusion and is smaller than the second term, determined by ion diffusion, because the ions tend to diffuse faster due to their larger gyroradius. However, when this happens an electric field will build up parallel to the density gradient (the ambipolar field) which will act to retard the ions. The result is that the plasma tends to diffuse with the slower rate governed by the electrons. With this in mind, and remembering that  $\Omega_e \gg v_e$  in the F-region, then the diffusion coefficient perpendicular to a magnetic field can be written

$$D_{\perp} = \frac{K v_e (T_e + T_i)}{M_e \Omega_e^2}. \quad (3.23)$$

In order to determine the parallel diffusion coefficient we need to consider the momentum balance equation parallel to the magnetic field

$$0 = -KT_j \frac{\partial n_j}{\partial z} + n_j q_j E_z - n_j M_j v_j V_{jz}. \quad (3.24)$$

Applying equation 3.24 to ions and electrons and then adding gives

$$0 = -K(T_e + T_i) \frac{1}{n} \frac{\partial n}{\partial z} - V_z (M_i v_i + M_e v_e). \quad (3.25)$$

The parallel diffusion coefficient can be defined by an expression of the form

$$\mathbf{V}_z = -D_{\parallel} \frac{\nabla_{\parallel} n}{n}. \quad (3.26)$$

By substituting equation 3.26 into 3.25, the parallel plasma diffusion coefficient is given by

$$\frac{1}{D_{||}} = \frac{M_e v_e}{K(T_e + T_i)} + \frac{M_i v_i}{K(T_e + T_i)}. \quad (3.27)$$

As this diffusion occurs perpendicular to the wave vector of the irregularities, the ambipolar electric field in the parallel direction does not restrict the diffusion. The first term in equation 3.27 dominates as this corresponds to the fastest diffusion. Equation 3.27 can be simplified to

$$D_{||} = \frac{K(T_e + T_i)}{M_e v_e}. \quad (3.28)$$

Diffusion can be represented by the equation

$$\frac{d^2 \Delta N}{dx^2} D = \frac{d \Delta N}{dt}. \quad (3.29)$$

If the decaying irregularities can be represented by

$$\Delta N = A e^{ikx} e^{-\frac{t}{\tau}}. \quad (3.30)$$

Then the time constant can be written as

$$\tau = \frac{1}{k^2 D}. \quad (3.31)$$

The diffusion will have contributions from parallel and perpendicular to the magnetic field. Substituting from equations 3.28 and 3.23 gives (Hysell *et al.*, 1996)

$$\frac{1}{\tau} = \frac{K(T_e + T_i)}{M_e v_e} k_{||}^2 + \frac{K v_e (T_e + T_i)}{M_e \Omega_e^2} k_{\perp}^2. \quad (3.32)$$

The time constant defined by equation 3.32 has a value of a few seconds. Where a two time constant regime is observed in coherent scatter data, as described by equation 3.9, the first decay is attributed to the diffusion mechanism described above (Hysell *et al.*, 1996). The second, longer time constant which is sometimes observed represents the decay of large-scale irregularities, which undergo mode

conversion and are therefore visible to an HF radar ( Belenov *et al.*, 1977; Coster *et al.*, 1985; Hysell *et al.*, 1996).

### **3.5 Review of experimental work**

Ionospheric modification experiments began in the early 1970s, and the first major work to be published on the topic was the special issue of *Radio Science* (November, 1974). In this journal the first experiments performed with the Platteville ionospheric facility (Carroll *et al.*, 1974) are described. The Platteville facility was utilised in a number of different experiments, beginning in 1970. Utlaut and Violette (1974) observed the effects of ionospheric modification with vertical incidence radio sounders. These authors reported that O-mode diagnostic waves were subject to anomalous absorption during O-mode heating, and that airglow increased during times of high absorption. Another early experimental result was that ionospheric modification could produce ionogram traces which were indistinguishable from naturally occurring spread-F (Allen *et al.* 1974). These observations were accounted for by the mechanism of heater induced field aligned irregularities causing scatter of the ionosonde rays.

A useful diagnostic technique for investigating field aligned irregularities is coherent scatter, which provides a direct method for measuring field aligned irregularities. Small-scale field aligned irregularities (FAI) with scale sizes of a few metres to tens of metres across the geomagnetic field coherently backscatter radar signals when the radar beams are directly orthogonal to the geomagnetic field. Fialer (1974) measured scatter between a transmitter receiver pair in the HF and low VHF bands. The irregularities were found when the heater was operating in O-mode polarisation and reflecting within the ionosphere (Fig 3.1a). By considering the geometry of the scatter it was determined that the irregularities were highly elongated along the magnetic field. Minkoff *et al.* (1974) made measurements of scatter in the VHF and UHF bands. These authors noted two distinct scattering modes. The first mode, known as centre-line scatter, returns scatter at a frequency close to that of the transmitted frequency, and can be understood in terms of scattering from electron density perturbations. The second type of scatter, plasma-line scatter, is seen as side-bands displaced either side of the transmitted radar frequency by the heater frequency. These authors also present observations of heating close to the peak plasma frequency of the ionosphere. During heating under these conditions it is possible to penetrate the ionosphere at the centre of the heater beam, leaving only oblique heater rays to reflect within the ionosphere.

The high power RF modification facility near Tromsø, in northern Norway (Stubbe and Kopka, 1979; Rietveld *et al.*, 1993) was completed in 1980 and

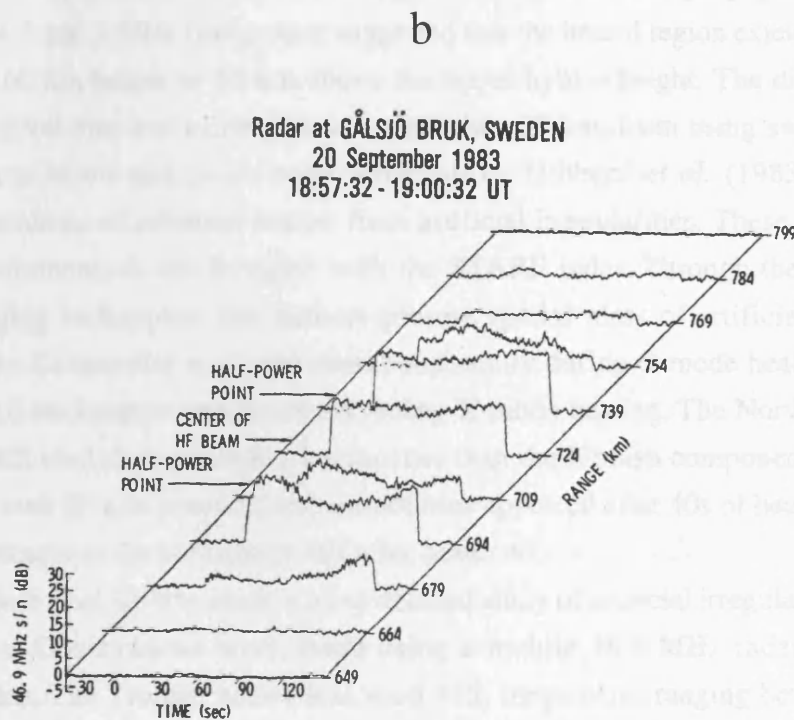
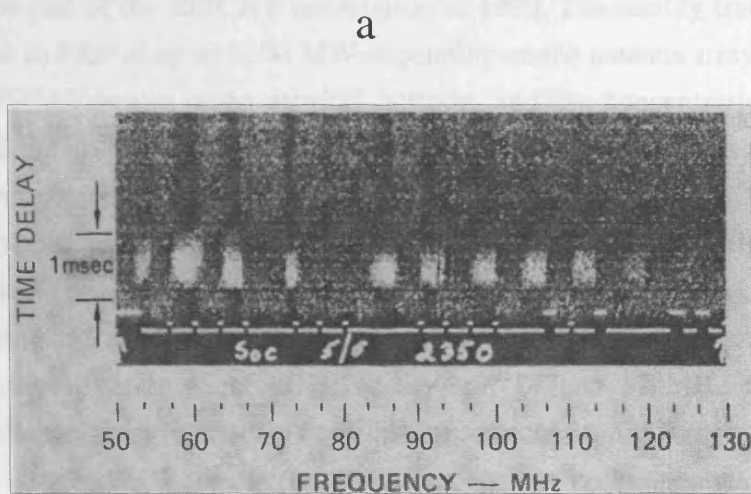


**Figure 3.1.** a) Observations of F-region irregularities during 5-sec on 5-sec off heater pulsing. The gaps are where the transmitter was disabled at certain frequencies (after Fialer, 1974). b) Radar power versus time for 11 adjacent radar ranges (after Djuth *et al.*, 1985).

became part of the EISCAT association in 1993. The facility transmits in the HF band at an ERP of up to 1200 MW depending on the antenna array. The position of the EISCAT heater at an auroral latitude, and the concentration of diagnostic equipment in the surrounding region has given rise to many investigations, beginning soon after the heater was completed in the early 1980s. Hedberg *et al.* (1983) observed coherent backscatter from artificially produced irregularities over Tromsø. These authors observed backscatter at Kiruna with a coherent radar operating at 3 and 7 MHz, and at Lycksele (using the Swedish and French auroral radar investigation (SAFARI) facility) on 14 and 17 MHz (Fig. 3.2b). The irregularities were excited to equilibrium in seconds, and had a decay constant of order 10 seconds. These constants were found to be frequency dependent, being longer at lower radar frequencies. The strongest echoes were found when the pump frequency was close to the F-region peak, and echoes were absent during X-mode heating. Variation in heater output gave a corresponding change in echo amplitude, with no threshold effects seen. Using estimations of wave propagation limitation for the 3 and 7 MHz backscatter suggested that the heated region extended vertically from 60 km below to 20 km above the upper hybrid height. The diameter of the heated volume was estimated to be less than 75 km, from using swinging of the antenna beam and pulse echo information. Hibberd *et al.* (1983), also made observations of coherent scatter from artificial irregularities. These authors made measurements in the E-region with the STARE radar. Through the use of beam swinging techniques, the authors present spatial plots of artificial and natural scatter. Backscatter was seen most consistently during O-mode heating, although limited backscatter was observed during X-mode heating. The Norwegian half of STARE tended to see better backscatter than the Finnish component. The spatial plots took 20 s to produce, and instabilities appeared after 40s of heating and were still present in the ionosphere 40s after heater off.

Djuth *et al.* (1985) made a more detailed study of artificial irregularities in the E-region. Observations were made using a mobile 46.9 MHz radar deployed in Sweden. The Tromsø heater was used with frequencies ranging between 2.8 and 4.9 MHz, chosen to give O-mode reflection in the E-region. The scattering cross sections observed were found to be less than those measured in the E-region over Platteville at 47 MHz but much greater than those obtained at Arecibo with a 50 MHz radar. The authors found that allowing for differences in absorption and HF power that this was consistent with FAIs being more strongly excited when the dip angle is large. The growth time of the echoes was found to be 100 ms for strong echoes and tens of seconds for weak echoes. Spectral analysis showed that the FAI signals had spectral widths of 15 Hz, broader than previous measurements made at Arecibo, This could be due to bulk plasma motion along the radar line of site and

random motion of “scattering centres” in the heated volume. The radar echoes (from around 115 km altitude) had a typical width 30 to 75 km or more in the North-South direction and were often detected outside the half-power point (Fig. 3.1b). The authors thought that this could be due to horizontal gradients refracting the rays. The work of Djuth *et al.* (1985) was extended by Noble *et al.* (1987). These authors considered multifrequency observations at 21.4-143.8 MHz and incorporated past results obtained at Arecibo (Coster *et al.*, 1985). They concluded that in the E-region, instabilities operating at the upper hybrid level such as the thermal parametric instability (Lee and Kuo, 1983) and the resonance instability (Inhester *et al.*, 1981) were in closer agreement with the observations than instabilities which operate at the reflection point, such as the parametric decay instability (Stubbe and Kopka, 1981). However, they point out that any of these mechanisms could contribute to irregularity production, particularly in the F-region.

### **3.5.1 Observations of decaying FAI**

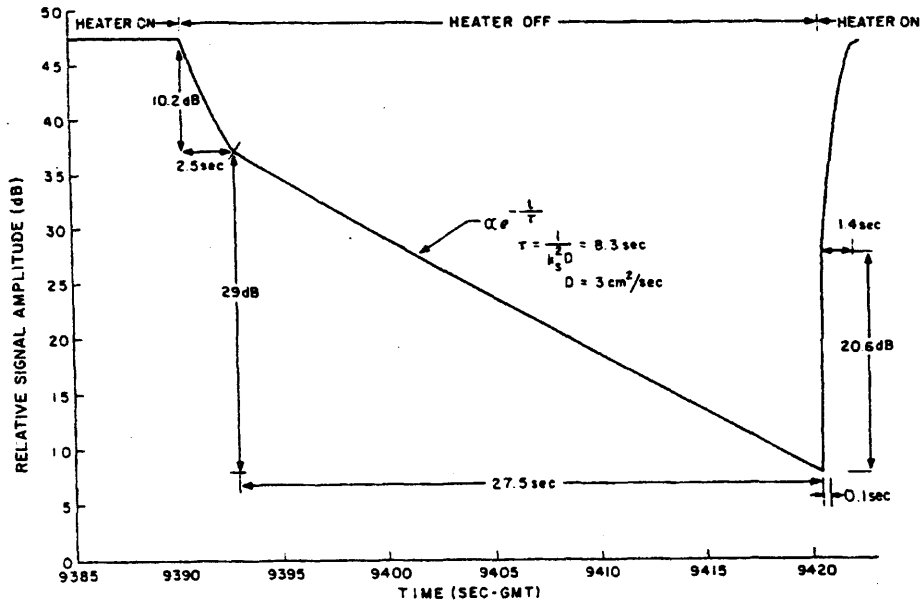
Artificial field aligned irregularities remain in the ionosphere for some time after the high power radio beam has been turned off, and gradually decay over periods as long as a few minutes. Investigation of the decay of these irregularities is particularly suited to coherent radar techniques, which can be utilised to select specific instability scale sizes. The nature of the decay reveals the diffusion processes which occur after heater-off.

Minkoff and Kreppel (1976) identified two decay stages in data obtained with a VHF backscatter system over Platteville, Colorado (Fig. 3.2a). These authors found that there was an initial fast decay with a time constant of a few seconds, followed by a slower decay with a time constant of 10s of seconds. Early experiments at the Sura heating facility in Russia also identified a two stage decay processes for the irregularities. Belenov *et al.* (1977) associated the first decay with cross-field diffusion and the longer time constant with the decay of large scale irregularities.

Hedberg *et al.* (1983) made observations of irregularities produced by the EISCAT high power facility at Tromsø, Norway (Rietveld *et al.* 1993). These authors employed HF radars located at Kiruna, Lycksele and Uppsala, operating on frequencies between 3 and 15.6 MHz. Their decay curves are presented in Fig. 3.2b. The irregularities decay over tens of seconds, and a two stage decay is visible.

Coster *et al.* (1985) observed artificial irregularities produced by the Arecibo heater with a 50 MHz radar. These authors attributed the observed decay times to electron diffusion across field lines. They did not observe a two stage decay (Fig.

a



b

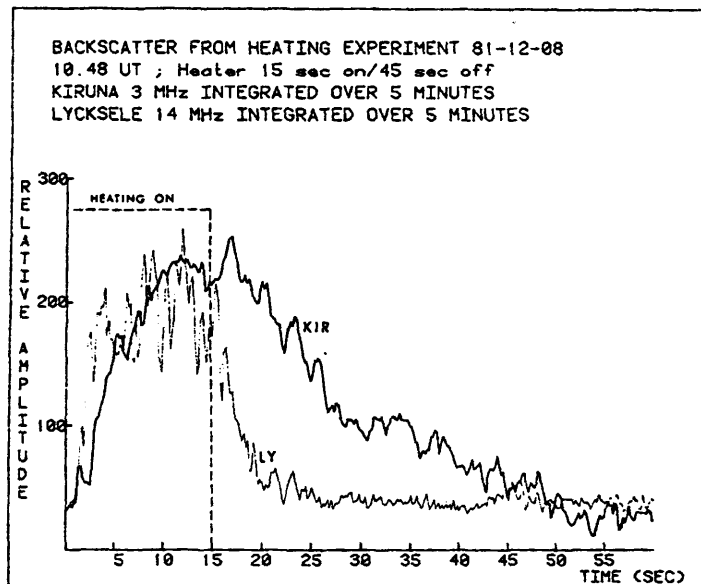


**Figure 3.2.** Coherent radar observations of the decay of artificial FAI after heater-off. a) After Minkoff and Kreppel, 1976. b) After Hedberg *et al.*, 1983.

3.3a), and suggested that their observations may not have been sensitive enough to measure the second decay rate. For 3m striations in the F-region these authors observed a decay time constant of 1s.

Hysell *et al.* (1996) made observations of irregularities produced by the Sura heating facility situated near Nizhny Novgorod, Russia. These authors utilised the UTR2 radio telescope as a bistatic HF radar in order to measure coherent scatter from the irregularities produced at Sura. They made observations at frequencies between 12 and 20 MHz and observed a decay which consisted of two time constants (Fig 3.3b). The first decay ranged from about 6s for 20 MHz observations to 10s at 12 MHz. The second decay constant was around 30s.

### **3.6 Concluding Remarks**

Previous work on artificial field aligned irregularities has been reviewed. A number of mechanisms have been proposed for the production of artificial FAIs, all of which may be excited under certain conditions. They include the thermal parametric instability (Lee and Kuo, 1983), the resonance instability (Inhester *et al.*, 1981) and the parametric decay instability (Stubbe and Kopka, 1981). The irregularities can be excited over a wide area, often outside the half-power point of the heater beam (Djuth *et al.*, 1985), and at low levels of heater power (Stubbe *et al.*, 1982; Coster *et al.*, 1985). The CUTLASS coherent scatter radar has been utilised to investigate the spatial extent of the heated region, and to estimate the power required to excite the instabilities. These results are discussed in chapter 6. Artificially produced irregularities remain in the ionosphere for some time after the high power transmitter has been turned off, and the decay is indicative of the properties of the plasma (Hedberg *et al.*, 1983, Coster *et al.*, 1985; Hysell *et al.*, 1996). CUTLASS measurements of heater-induced backscatter after heater-off are presented in chapter 7.

a

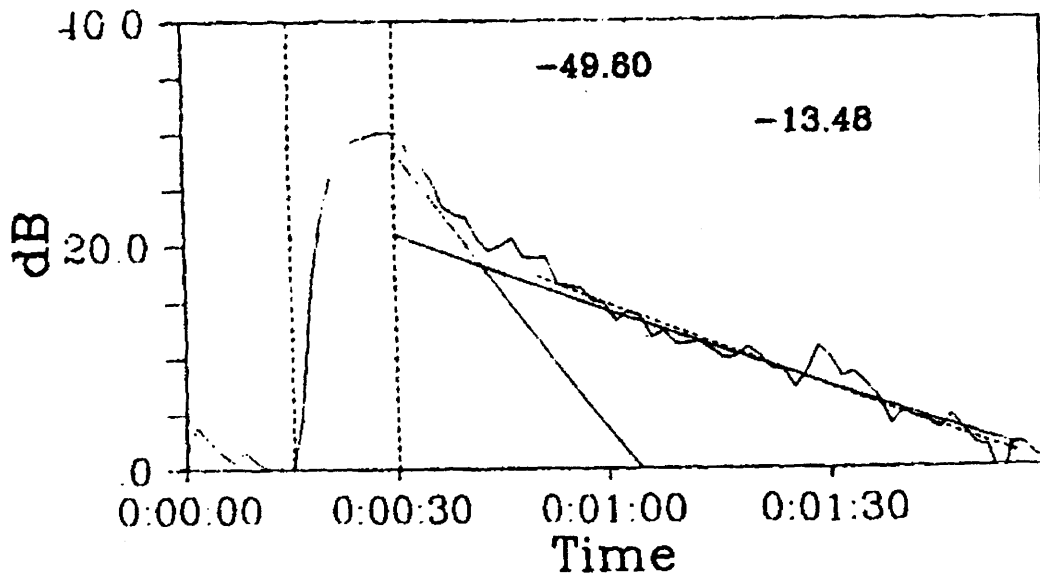
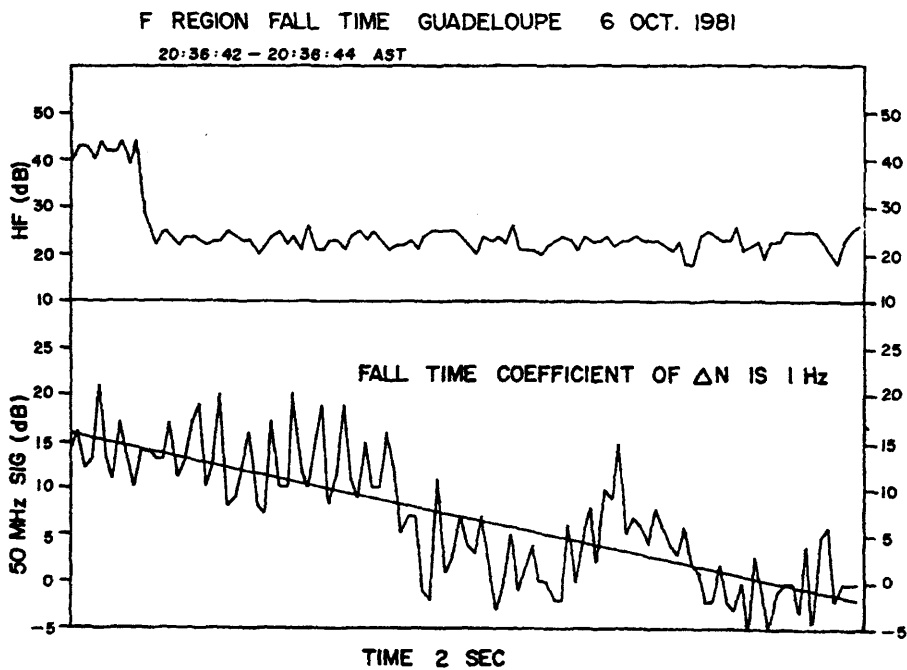


Figure 3.3. Coherent radar observations of the decay of artificial FAI after heater-off. a) After Coster *et al.*, 1985. b) After Hysell *et al.*, 1996.

## Chapter 4

# *Instrumentation*

### 4.1 Introduction

High power radio waves are capable of producing field aligned irregularities in the ionosphere. These irregularities provide backscatter targets for coherent scatter radars (Fialer, 1974) and also produce anomalous absorption of both low power diagnostic signals and the heater wave itself (Jones *et al.*, 1982; Stubbe *et al.*, 1982; Robinson 1989). Large scale changes are also observed, in particular changes in electron temperature and density are well documented, and can be measured by incoherent scatter radars (Gordon *et al.*, 1971; Utlaut and Violette, 1972; Gordon and Carlson, 1974; Jones *et al.*, 1986; Djuth *et al.*, 1987; Stocker *et al.*, 1992; Robinson 1989; Robinson *et al.*, 1996; Robinson *et al.*, 1997). In addition, changes can occur in ion temperature and possibly composition.

This thesis contains observations from 2 experimental campaigns involving the EISCAT ionospheric modification facility (heater) at Tromsø, Northern Norway. The first campaign, in February 1995, involved incoherent scatter observations of E-region heating. The other campaign in April 1996, concentrated on F-region heating, and the CUTLASS coherent scatter radar was utilised to observe the field aligned irregularities produced during artificial modification experiments. In this chapter the experimental equipment and techniques utilised during these campaigns are discussed.

### 4.2 HF artificial modification

The energy radiated into the ionosphere during modification by high power radio waves is usually described in terms of the effective radiated power, or ERP, of the transmitting facility. The ERP is equal to the transmitted power multiplied by the antenna gain. The electric field,  $E$  (V/m), produced by a heater beam with  $ERP$  in kW, at an altitude,  $R$  (km), is (Walker, 1979)

$$E = \frac{0.25\sqrt{ERP}}{R}. \quad (4.1)$$

This equation ignores D-region absorption (which is a good approximation for nighttime experiments). For a modification facility with an ERP of 300 MW the electric field calculated from the above equation will have a value of around 1.3  $\text{Vm}^{-1}$  at 100 km. However, a radio wave reflecting in the ionosphere can produce

a standing wave pattern below its reflection height which can significantly increase this value (*e.g.* Rietveld *et al.*, 1993). This is known as amplitude swelling and can increase electric fields at vertical incidence by a factor of 5 or more.

The plasma frequency of the ionosphere is a characteristic frequency of the plasma which is proportional to the square root of the electron density. It is a useful quantity in the context of modification experiments as it represents the frequency of a radio wave which will reflect at that point in the plasma. Heating experiments can be classified into two types, underdense and overdense. In underdense heating, the frequency of the modifying wave is above the peak plasma frequency and the radio wave penetrates the ionosphere. Underdense experiments produce a weak interaction between the radio wave and the plasma. In overdense heating the frequency of the radio wave is below the peak plasma frequency and the radio wave reflects within the ionosphere. The overdense case represents a strong interaction between the radio wave and the ionosphere. The most intense effects during modification experiments are seen close to the reflection point.

### **4.3 The EISCAT RF modification facility**

The high power RF modification facility at Ramfjordmoen, near Tromsø, in northern Norway (69.6 °N, 19.2 °E, L= 6.2, magnetic dip angle I= 78 °) (Stubbe and Kopka, 1979; Rietveld *et al.*, 1993) was constructed jointly by the Max-Planck-Institut für Aeronomie, Lindau and the University of Tromsø (Fig 4.1). The first low power tests commenced in August 1979 and full operation began in September 1980. A review of experiments which have been performed with the Tromsø heater has been written by Stubbe (1996).

After an offer from the Max-Planck-Institut für Aeronomie, it was decided that the ownership and the responsibility for the operation of the heater would be transferred to EISCAT. The facility officially became part of the EISCAT association in 1993.

#### **4.3.1 Heating facility transmitters**

The heater can generate up to 1.2 MW of continuous wave power from a total of 12 transmitters. The transmitters were originally specified at 125 kW each, but in fact have a maximum power output of 100 kW each. Each of the transmitters is driven by a solid state wideband exciter, which means that matching and tuning is only required at the output. The tuning and matching is achieved automatically



**Figure 4.1.** The EISCAT site at Tromsø, Northern Norway. The UHF transmitting antenna is in the top right of the picture and the VHF is in the top left. The heater array is in the bottom left of the picture.

through the use of phase and voltage discriminators. An iterative process is utilised, which is required due to the close coupling between the antennas. The amplitude and phase are adjusted for one transmitter whilst the others are kept at constant amplitude and phase, and this process is then repeated for all the other transmitters. Convergence is reached after around 5 steps, which can take a few minutes. The process is much faster if fewer transmitters are in use.

Each transmitter is linked to a synthesiser/function generator which produces the RF source. The synthesisers are locked to a frequency reference which is in turn locked to the clock utilised by the EISCAT radars. This aids synchronisation during experiments, which is particularly useful for short modulation times. An old Commodore PET computer is employed to programme the frequency, amplitude and phase for the synthesisers, although in the near future this is to be replaced by a PC based system.

The impedance of the antennas suppresses the level of harmonic radiation produced by the system. Measurements near the antenna arrays indicate that the second harmonic and 50 Hz noise from the mains supply are both around 55 dB below the fundamental.

The individual antennas in the heater array are linear full-wave dipoles. The dipoles are arranged in rows of crossed pairs. Two transmitters are linked to each row, each feeding one half of the cross in a row of antennas. Circular polarisation in either O- or X-mode is achieved by introducing a 90° phase shift between the two halves of each row at the synthesiser stage. The antenna beam is formed in a similar manner, only in this case the phase is altered between adjacent crossed dipoles, rather than between the two halves of a cross.

The heater is very flexible in its ability to transmit different frequencies. In addition to simply tuning all the transmitters to the same frequency, it is possible to tune different transmitters to different frequencies. As there are a total of 12 transmitters it is possible to tune to a maximum of 12 frequencies and then transmit those frequencies simultaneously. However, as explained above, in order to achieve circular polarisation it is necessary to have two transmitters feeding each row of crossed dipoles. Therefore, a maximum of 6 frequencies on 6 pairs of transmitters can be transmitted if circular polarisation is required.

#### **4.3.2 The heater antenna arrays**

The heater is capable of transmitting from three different heater arrays, which were originally designed to cover the frequencies 2.75-8 MHz. Each transmitter can be separately connected to any one of the three antenna arrays through the use of remotely controlled coaxial switches. This allows great flexibility when

designing experiments, as it is possible to transmit simultaneously from antennas in each of the arrays.

Before a storm in 1985, array 1 was the lowest frequency array. It has since been rebuilt with 12 rows of 12 antennas. It has a gain of 30 dB which corresponds to 1200 MW of ERP and has a frequency range of 5.5-8 MHz. The array produces a beam width of 7°.

Arrays 2 and 3 each contain 6 rows of 6 crossed dipoles and operate in the frequency ranges 3.85-5.65 and 5.5-8 MHz respectively. They have a maximum ERP of 300 MW, corresponding to a gain of 24 dB. The beamwidth for these arrays is 14.5°. Array 2 previously had additional phasing to allow the heater beam to intercept the path of rockets from the Andøya range, but this capability has since been removed. The antennas are designed to have a standing wave ratio of less than 2, although this is normally less than 1.5. During winter, high standing wave ratios can result from severe weather conditions and the weight of snow on the transmission lines. Under these conditions it is sometimes necessary to shut down the affected transmitters, resulting in a lower ERP and a wider beamwidth.

### **4.3.3 Heater modulation**

The ability to modulate the output from the heater is very important in modification experiments, and a variety of complicated on-off patterns can be achieved. In addition, it is often desirable to alter other parameters during an experiment, such as power, polarisation or beam angle.

Actually turning the heater on and off, between full and zero power, cannot be achieved quickly and is impractical for most experiments. An alternative is to utilise the lowest possible synthesiser voltage, which is 37.5 dB below full power, and this is off for most purposes. For experiments where an even lower power “off” is required it is possible to reduce the power level by another 70 dB by utilising attenuators after the synthesisers.

Most modulation sequences are programmed on a Texas-Instruments computer. This allows complicated modulation cycles to be carried out accurately. The minimum heater-on time is governed by the rise time for the output power of the transmitters. This rise time is around 5  $\mu$ s, which in practice sets a lower limit for heater-ons of around 20  $\mu$ s. There is no upper limit, and so heater-on times of hours are possible. The only frequencies which should not be utilised for modulation are those which can cause resonances with the power supply, for this reason frequencies between 15 and 200 Hz are avoided.

The Texas-Instruments computer is also employed when experiments require the heater power to be varied. This is achieved by varying the amplitude modulation voltage to the synthesisers. A calibration process is utilised, as each synthesiser requires a different voltage. The program allows 40 power intervals at 2.5 % steps, which is ample for most experimental purposes. This method of stepping the heater power avoids the need to re-tune the transmitters when a different power setting is required.

Changing the polarisation between O- and X-mode is a relatively simple task which can be performed with either the Texas-Instruments or the Commodore computer. On the Texas-Instruments computer it is necessary to programme a 1 V signal to be sent to the phase modulation input of the synthesisers. The Commodore programme has an option which allows the phase to be changed.

The antenna rows lie in the East-West direction, and so phasing allows the heater beam to be steered in the North-South meridian. This is most easily done during the tune-up process, but can be achieved without the need for tuning if fast switching between directions is required. A specially built voltage source is available for this task. The most common beam directions are pointing vertically or along the geomagnetic-field line

The high latitude location of the HF facility is well suited to modification experiments involving the auroral electrojet. In addition, the EISCAT UHF incoherent radar facility is located nearby.

#### 4.4 Incoherent scatter

##### 4.4.1 Development of incoherent scatter

Incoherent scatter is a very powerful technique, which uses the scatter of radio waves from the acoustic waves generated in a plasma to measure a variety of plasma parameters. The European Incoherent Scatter (EISCAT) facility in northern Scandinavia, is one of the most advanced facilities of its type in the world today.

It is possible to derive a classical interaction cross-section for an electromagnetic wave incident on an electron. For direct backscatter this is approximately:

$$\sigma_e = 10^{-28} m^2 \quad (4.2)$$

Although it was suggested in the late 1920s that this phenomenon might be used for ionospheric experiments, it was not until much later (Gordon, 1958), that the

idea was taken seriously. Up until this time the main diagnostic for studying the ionosphere was the ionosonde. This technique uses the fact that a radio wave reflects from the ionosphere when its frequency matches the plasma frequency. The plasma frequency is a function of the electron density, so an ionosonde can be used to create an electron density profile for the ionosphere. The major drawback with this technique is that it is not possible to receive information from above the peak density of the ionosphere. Incoherent scatter does not suffer from this limitation, and in addition the returned incoherent spectrum can be used to find many ionospheric parameters.

Simple incoherent scatter theory considers a radio wave scattering from a population of independent electrons, with the returned signal power being proportional to the electron density. In this situation the returned signal will have a Doppler-broadened spectrum from the random thermal motions of the electrons, and a Doppler shift corresponding to the bulk motion. Early experiments (Bowles 1958) demonstrated that this is not the case, and that in fact the returned spectrum corresponds to the thermal motions of the ions rather than the electrons.

Later experiments (e.g. Dougherty and Farley 1960) illustrated that the characteristics of the returned signal are governed by the ions as long as the radar wavelength is much greater than the Debye length, which is a characteristic scale size of the plasma. For wavelengths below the Debye length, true incoherent scatter occurs from the electrons. Radars such as EISCAT typically operate at wavelengths much greater than the Debye length, and so they measure the ion dominated spectrum, but rather confusingly this is still referred to as incoherent scatter. The spectrum produced has a distinct double-humped shape, which is caused by Bragg scatter from the up-going and down-going ion-acoustic waves.

#### **4.4.2 Parameters determined by incoherent scatter**

A number of plasma parameters can be derived from the returned signal. The ionospheric electron density profile may be determined from the total power of the returned signal. Returned power is proportional to electron density, and so to give an absolute value a system constant is required. This can be determined by calibrating the measured density with an independent diagnostic such as an ionosonde.

The ion-lines are caused by scatter from the up-going and down-going ion-acoustic waves, and so the separation between the lines in the spectrum is approximately twice the ion-acoustic frequency. The ion-acoustic frequency is given by the ratio of the ion temperature to the ion mass, so this ratio can be determined from the separation of the ion-line maxima. An absolute value for ion

temperature can be determined by assuming a value for ion mass, and the electron temperature can be established by using the temperature ratio found from the broadening of the ion-lines. As the value of ion mass is assumed, the accuracy with which the temperatures can be determined depends greatly upon the quality of the ion composition model employed.

The ion lines which make up the doubled humped spectrum are broadened by Landau damping to a degree which depends on the ratio of the electron and ion temperatures. When the ratio increases, the ion-acoustic velocity changes and this reduces the attenuation of the wave, which in turn produces less broadening of the ion lines in the spectrum. The ratio of the peak power of the spectrum to the power at the central minimum is a measure of this broadening, and can be used to calculate the temperature ratio.

A Doppler shift occurs in the frequency of the incoherent scatter spectrum due to the bulk motion of the plasma. For a monostatic system, the Doppler shift corresponds to the component of the plasma velocity along the radar beam. For a multistatic system, such as the EISCAT UHF system, the Doppler shift corresponds to the plasma velocity along the mirror direction, which is the bisector of the angle between the transmitter and the receiver beams. The advantage of a multistatic system is that it allows the plasma velocity to be determined in three dimensions.

As well as the parameters described above, there are a number of other parameters that can be derived from the incoherent scatter spectrum under restricted conditions and height ranges, and others that can be estimated if certain variables are assumed (Fig. 4.2).

#### **4.4.3 The EISCAT radars**

The European Incoherent SCATter (EISCAT) facility (Rishbeth and Williams, 1985) began operation in 1982 (Fig. 4.1). The facility comprises two radars, a monostatic VHF radar and a tristatic UHF system. The transmitter and receiver for the VHF radar are co-located in Tromsø, northern Norway, although this system was not utilised for any of the experiments described in this thesis. The transmitter of the UHF radar system is located at Tromsø, with receivers at Tromsø, Kiruna in Sweden and Sodankylå in Finland.

The UHF antenna system comprises of three fully steerable 32 m diameter parabolic antennas, one located at each of the three sites. The UHF transmitter is capable of providing a peak power of 2 MW and an average power of around 250 kW. The transmitter operates on a central frequency of 931 MHz, and can switch

*Parameters measured by incoherent scatter*

(i) *Directly measured*

Electron concentration,  $N$

Electron temperature,  $T_e$

Ion temperature,  $T_i$

Ion composition

Ion drift velocity,  $V_i$

Ion-neutral collision frequency,  $\nu_{in}$

Photoelectron flux

(ii) *Derived indirectly*

Neutral particle density,  $\rho$

Neutral gas temperature,  $T$

Neutral air velocity,  $U$

Pedersen and Hall conductivity,  $\Sigma_P$ ,  $\Sigma_H$

Electric current

Heat flux

**Figure 4.2.** Parameters measured by incoherent scatter  
(after Rishbeth and Williams, 1985)

between 16 frequencies around the central frequency on a time scale of microseconds.

#### **4.4.4 Incoherent scatter measurement techniques**

The simplest form of pulse transmitting technique involves sampling the pulse when it is received by the radar, and forming an autocorrelation function (ACF). The ACF is the Fourier transform of the incoherent scatter power spectrum, from which the ionospheric parameters are retrieved. To form the ACF, cross-products are calculated for the samples from the radar. The time delay between two samples in a cross-product is called the lag and by evaluating many cross-products, and hence lag estimates, an average lag is found. Many average lags are put together to form the ACF. In early EISCAT experiments, the receiver was 'gated', which meant that samples were between two specific times which corresponded to the range required. This gated technique produced a closed set of samples, and so there were many estimates for short lags, and fewer estimates for longer lags, the longest lag being derived from a single estimate. This produced a reduction the effective signal to noise ratio, and an uneven spatial distribution for the different lags. The problem was solved by the implementation of new correlator programmes (Turunen, 1986) which introduced the concept of gating after the evaluation of cross-products.

Designing pulse schemes for incoherent scatter involves an element of compromise. To produce the best spatial resolution, short pulses are required. These ideally need to represent a distance less than the scale height of the ionospheric region being considered, and even shorter if smaller-scale structure is to be resolved. However, short pulses provide poor spectral resolution, and the pulse must be long enough to allow an accurate spectrum to be determined. In the F-region of the ionosphere these factors do not present a significant problem. In this region the scale size is of the order 50 km, and so a single pulse technique can be utilised without compromising spatial or spectral resolution. In addition, because the time-of-flight is long in this region, the fact that the radar cannot transmit and receive at the same time does not pose serious difficulties. In the E-region the problem is more significant. The scale height in this region is only few km, and the length of pulse is further constrained by the time-of-flight.

An alternative method is to employ multi-pulse techniques (Farley, 1969, 1972). In a multi-pulse regime, a series of sub-pulses is transmitted within a time envelope. The length of the sub-pulses is short enough to provide adequate spatial resolution, whilst the length of the envelope provides the required spectral resolution. An extra pulse is transmitted at a slightly different frequency to

provide the zero lag, sometimes referred to as a power profile. A disadvantage with multi-pulse is that the codes produce self-clutter which reduces the signal-to-noise ratio. Self-clutter occurs because echoes from different sub-pulses at different heights are received simultaneously. This problem can be relieved by another pulse technique, called alternating code. An alternating code is a series of pulses, each comprising a sequence of coded sub-pulses. On decoding, all self-clutter is cancelled out, and only a single lag at a single range remains. This is known as strong condition alternating code. For weak condition code, not all self-clutter is removed, and this can be resolved by the use of more frequencies or further coding. Another advantage of alternating code is that, unlike multi-pulse, it utilises a high proportion of the available duty cycle.

#### **4.4.5 EISCAT programmes**

EISCAT programmes are divided into two principle types, each utilising about half of the observing time. The first type are common programmes, these are routine experiments which provide a common source of data for scientists from all associate countries. The second type are special programmes, which are designed for specific experimental objectives by scientists from individual associate countries. There are currently 7 different common programmes, 3 for the VHF system and 4 for the UHF radar. These experiments have been developed over a number of years and have very efficiently coded transmitter and correlator programmes. Heating experiments run as a special programme, but utilise much of the code developed for common programme 1 (CP-1).

CP-1 was designed for high time resolution studies of dynamic phenomena. The UHF transmitter beam is aligned along the local magnetic field direction near the F-region peak, which corresponds to an elevation of around  $77^\circ$  at Tromsø. For heating experiments, this is often modified to point the beam vertically. The remote site antennas are positioned to intersect the transmitter beam in the F-region. Long-pulse, two power profiles and alternating code scheme are transmitted. CP-1, as with all the common programmes, has evolved over the years as new techniques have been developed. The alternating code is one example of a new addition, as a multi-pulse scheme was previously in use.

#### **4.4.6 Incoherent scatter data analysis**

A number of techniques exist for maximising the accuracy of incoherent scatter data, and tailoring the nature of the data output for specific requirements.

Post-integration is often utilised as a way of reducing uncorrelated noise. It is basically a process of adding together successive ACFs, or ACFs measured on a different frequency, to provide a more accurate ACF. Adding together successive ACFs will obviously affect the temporal resolution of the data, and post-integration is most useful when changes in the ionospheric parameters only occur over relatively long time scales. This is often the case in heating experiments, where the heater can be switched on and off with a period of a few minutes. Post-integration over a heater-period can be employed to clearly demonstrate the difference between heater-on and heater-off conditions.

The ACF measured by the radar is a convolution of the transmitted pulse and the pulse scattered by the ionosphere. As the pulse is processed by the receiver it is further modified by the receiver filter. These instrumental effects need to be removed, along with an estimation of the background noise level, before the extraction of ionospheric parameters from the data can begin, employing the methods described in section 4.4.2.

#### **4.4.7 Incoherent scatter measurement errors**

A number of uncertainties can occur in the parameters derived from incoherent scatter. The most obvious source of error is that of noise, which will introduce random errors when the signal-to-noise ratio is poor. However, there are other error sources which can significantly effect results.

The plasma parameters are found from the raw data by fitting a theoretical function to the measured ACF. An error will be introduced because the theoretical curve will not exactly fit the measured curve, and this is referred to as the fit error. Further uncertainty can be introduced by the plasma velocity distribution. EISCAT analysis techniques assume a maxwellian thermal velocity distribution, which may not always be a suitable approximation, particularly under conditions of strong field-aligned current flow or high ion-neutral relative flow. This can lead to overestimates in ion temperature and underestimates in electron temperature.

An ion composition model is required to produce the theoretical ACFs utilised in analysis, and assumptions made in the formation of this model may not always be accurate. In addition, different ion species will have different temperatures, a difference that is particularly marked when comparing molecular and atomic ions. Care must therefore be taken when analysing ion temperature measurements, as the value given will not simply be the mean temperature of the species present, due to the non-linearity of the incoherent scatter spectrum.

## 4.5 Coherent scatter

### 4.5.1 Coherent scatter mechanisms

Instabilities in the ionospheric plasma can cause fluctuations to grow to amplitudes much greater than the thermal level. Coherent scatter from these fluctuations can be detected if their wave number conforms to the following equation (which also applies to incoherent scatter)

$$\mathbf{k}_T = \mathbf{k}_s + \mathbf{k}_m \quad (4.3)$$

Where  $\mathbf{k}_T$  is the transmitted radar wave number,  $\mathbf{k}_s$  is the scattered radar wave number, and  $\mathbf{k}_m$  is the wave number of the medium. As the scattered and transmitted radar waves have the same wave number we have

$$\mathbf{k}_m = 2\mathbf{k}_T \quad (4.4)$$

In other words, backscatter is observed by the radar when the transmitted radar wavelength is twice that of the ionospheric irregularities. For this reason coherent scatter is termed “Bragg like” as it is analogous to X-rays scattering from a crystal. In addition to finding the power scattered from irregularities, the Doppler spectrum from coherent scatter can be utilised to measure the phase velocity of the irregularities.

Ionospheric fluctuations are typically aligned along the geomagnetic field, and so it is important for coherent scatter radar beams to achieve orthogonality with the magnetic field. At low latitudes this is easily accomplished, as the magnetic field is approximately horizontal, and so backscatter can be observed at all elevations in the plane perpendicular to the geomagnetic field. At auroral latitudes the orthogonality condition is more difficult to achieve, as the geomagnetic field is almost perpendicular to the Earth. To satisfy the orthogonality condition the radar is often located over a thousand kilometres away from the region of study. HF radar beams can be utilised as this frequency range undergoes refraction in the ionosphere, which makes the orthogonality condition easier to achieve.

### 4.5.2 The CUTLASS radar

CUTLASS (Co-operative UK Twin Located Auroral Sounding System) (Greenwald *et al.*, 1995) is a twin-station HF coherent scatter radar, designed to study the high latitude ionosphere. The radars are located in Pykkvibær, Iceland

and in Hankasalmi, Finland (Figs. 4.3 and 4.4). The fields of view of the two radars intersect over a 3 million km<sup>2</sup> region to the north of Scandinavia, and this arrangement allows the horizontal velocity of the ionospheric plasma to be resolved. It is an international facility, funded in the U.K. by the Particle Physics and Astronomy Research Council (PPARC), with additional contributions being made by Sweden and Finland. Construction of the Finland antennas began at the end of 1994, and the Finland radar made its first observations in early 1995. Construction of the Iceland antennas was undertaken in late 1995, and the complete system became operational in early 1996.

CUTLASS is ideally positioned to monitor RF modification experiments performed with the EISCAT heater. The CUTLASS Finland radar lies approximately 1000 km to the south of Tromsø, and this position allows measurements to be taken over a horizontal cross-section in the F-region above the heater. This arrangement also allows simultaneous observations to be made with the EISCAT incoherent scatter radars.

As well as providing useful data in their own right, the CUTLASS radars form part of SuperDARN, an international network of coherent scatter radars. This network provides extensive coverage over the auroral region in the northern hemisphere and also includes conjugate stations in the Antarctic.

Both sites make use of 16 antennas in their main arrays, which are each connected to separate 600W RF power amplifiers. An interferometer at each site is formed from a further 4 antennas, and this allows the angle of arrival of the returned signal to be determined.

The beam formed by the 16 antenna is 3.24° wide, and can be steered in any combination of 16 directions. In standard mode, the radars point in each of the 16 beam positions in turn, dwelling on each position for 7.5 seconds. This gives a full sweep of the 50° field of view every 120 seconds. CUTLASS transmits 300 μs pulses in standard mode, giving a range resolution of 45 km. This resolution can be increased to 15 km by the use of 100 μs pulses.

### 4.5.3 Coherent scatter measurement techniques

In CUTLASS, pulses are produced in the receiver and then amplified before being fed into branching networks which form a different time delay for each of the 16 channels. When the pulses are transmitted, they constructively interfere and form the radar beam. By altering the order of the delays a total of 16 beam directions can be formed.

The process of extracting parameters from coherent scatter data is discussed in a number of papers (Greenwald *et al.*, 1985; Villain *et al.*, 1987; Hanuise *et al.*,

CUTLASS viewing areas

a



b



**Figure 4.3.** The CUTLASS antenna arrays at a) Pykkvibær, Iceland and b) Hankasalmi, Finland.

## CUTLASS viewing areas

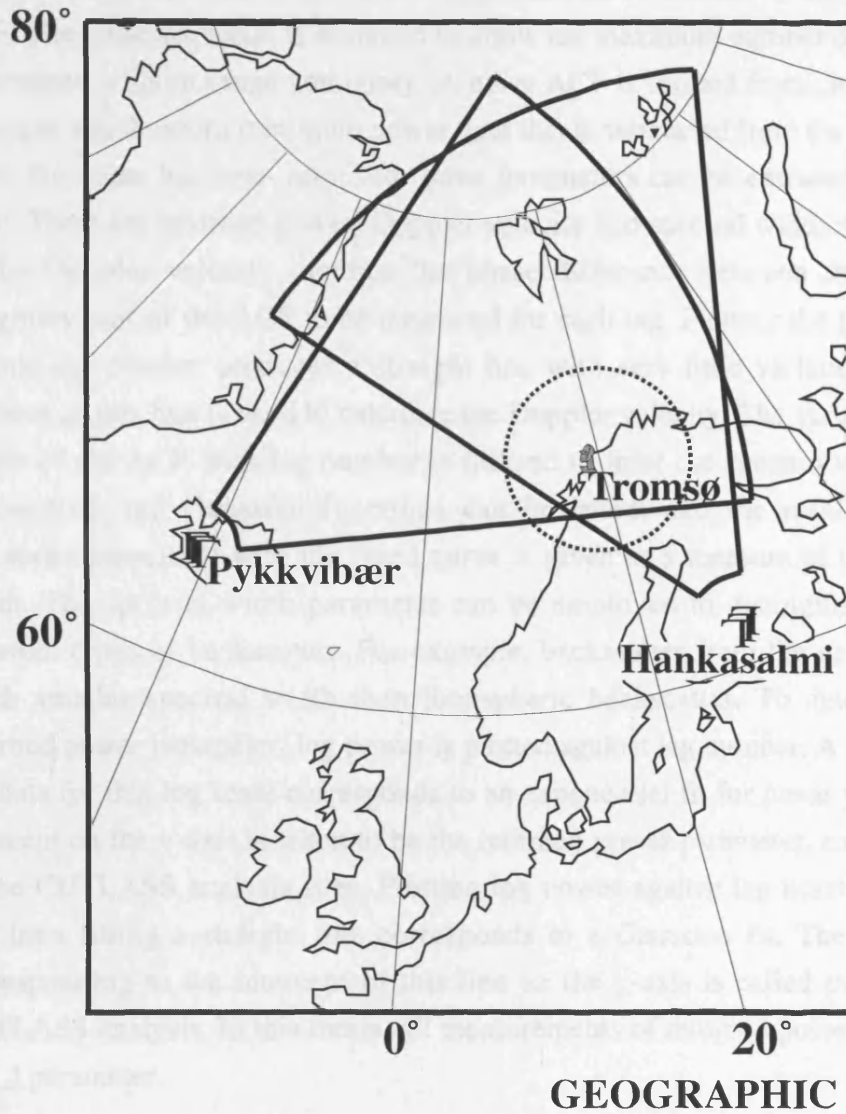


**Figure 4.4.** Schematic illustrating the positions and fields of view of the two CUTLASS radars in Hankasalmi and Pykkvibær. The location of the EISCAT heater and radar site is also indicated

1993). For CUTLASS and similar SuperDARN HF radars, a radar control program, RADOPS (now replaced with RADOPS2000), is employed to define the operational characteristics of the radar. In normal operation, a seven pulse sequence is transmitted which when received can be utilised to form a 17 lag ACF. The pulse sequence is designed to allow the maximum number of lags to be determined without range ambiguity. A noise ACF is formed from data recorded at ranges which return minimum power, and this is subtracted from the raw ACFs. After the noise has been removed, three parameters can be extracted from the ACF. These are returned power, Doppler velocity and spectral width. Calculation of the Doppler velocity requires the phase difference between the real and imaginary part of the ACF to be measured for each lag. Plotting the phase angle against lag number produces a straight line with very little variation, and the gradient of this line is used to calculate the Doppler velocity. The variation of the power of the ACF with lag number is utilised to infer the spectral width. Both exponential and Gaussian functions can be fitted, and the resulting width parameter associated with the fitted curve is given as a measure of the spectral width. The spectral width parameter can be employed to distinguish between different types of backscatter. For example, backscatter from the ground has a much smaller spectral width than ionospheric backscatter. To determine the returned power parameter, log power is plotted against lag number. A linear fit to the data for this log scale corresponds to an exponential fit for linear power. The intercept on the y-axis is taken to be the returned power parameter, called `pwr_l`, in the CUTLASS analysis files. Plotting log power against lag number squared and then fitting a straight line corresponds to a Gaussian fit. The parameter corresponding to the intercept of this line on the y-axis is called `pwr_s` in the CUTLASS analysis. In this thesis, all measurements of returned power utilise the `pwr_l` parameter.

#### 4.6 The low power diagnostic system

A low power diagnostic system built by the Radio and Space Plasma group at Leicester University has operated successfully during a number of ionospheric modification campaigns. In a typical experimental arrangement (*e.g.* Stocker *et al.* 1993) 4 transmitters for the low power diagnostic signals are co-located at a site about 50 km to the north of the heater, and 5 receivers are located about 40 km to the south. This arrangement ensures that the diagnostic waves travel only through the heated F-region and not the D- and E-region illuminated by the main lobe of the heater beam. The transmitters generate a continuous signal in the range 2.5-7 MHz, and at a power of 30 W. The antennas are inverted-V, and transmit signals

containing O- and X-mode components with equal strength. One of the receivers utilises a dipole antenna and is tuned to the heater frequency to monitor the heater status and ensure that timings between the heater and the diagnostics are synchronised. The other receivers use crossed active dipoles which enable either O- or X-mode waves to be recorded.

A high power radio wave can produce density striations in the ionosphere, and a low power radio wave travelling through this region will undergo anomalous absorption, resulting in a reduction in the received signal strength (*e.g.* Stubbe *et al.* 1982, Robinson 1989). In addition, an artificially produced density change can produce a phase shift in the received diagnostic signal (*e.g.* Jones *et al.*, 1982), and if the heater signal is modulated then cross-modulation can occur (*e.g.* Robinson, 1989).

Robinson *et al.* (1997) presented results from the first RF heating campaign at Tromsø in which the new CUTLASS HF radar, together with the EISCAT UHF radar and a low power HF diagnostic radio system were in simultaneous operation. Fig. 4.5 depicts observations during an RF heating sequence comprising 4 minutes O-mode, 3 minutes off, 4 minutes X-mode, 3 minutes off, 4 minutes O-mode. During O-mode heating backscatter was observed from CUTLASS, an electron temperature increase was recorded by EISCAT, and anomalous absorption was detected by the lower power diagnostic system. No effect was seen in any of the diagnostics during X-mode heating. These observations provide the first direct observational link between anomalous absorption and FAI. Now that this link has been demonstrated it is the intention of the Leicester University group to rely on CUTLASS to provide complementary diagnostic information to the EISCAT radars during modification experiments, and it is expected that the low power diagnostic system will have a more limited role in future campaigns.

#### 4.7 Concluding Remarks

The EISCAT high power transmitter provides a world class ionospheric modification facility. However, the usefulness of such a facility is entirely dependent on the range and quality of diagnostic equipment available. The EISCAT heater lies in one of the most heavily instrumented regions in the world. Of most significance to this thesis are the EISCAT UHF incoherent scatter radar and CUTLASS. These diagnostic tools provide complimentary information on both the natural and artificially modified ionospheric parameters during experiments. For the data presented in this thesis, the EISCAT radar has been utilised to provide measurements of ion and electron temperature, electron density

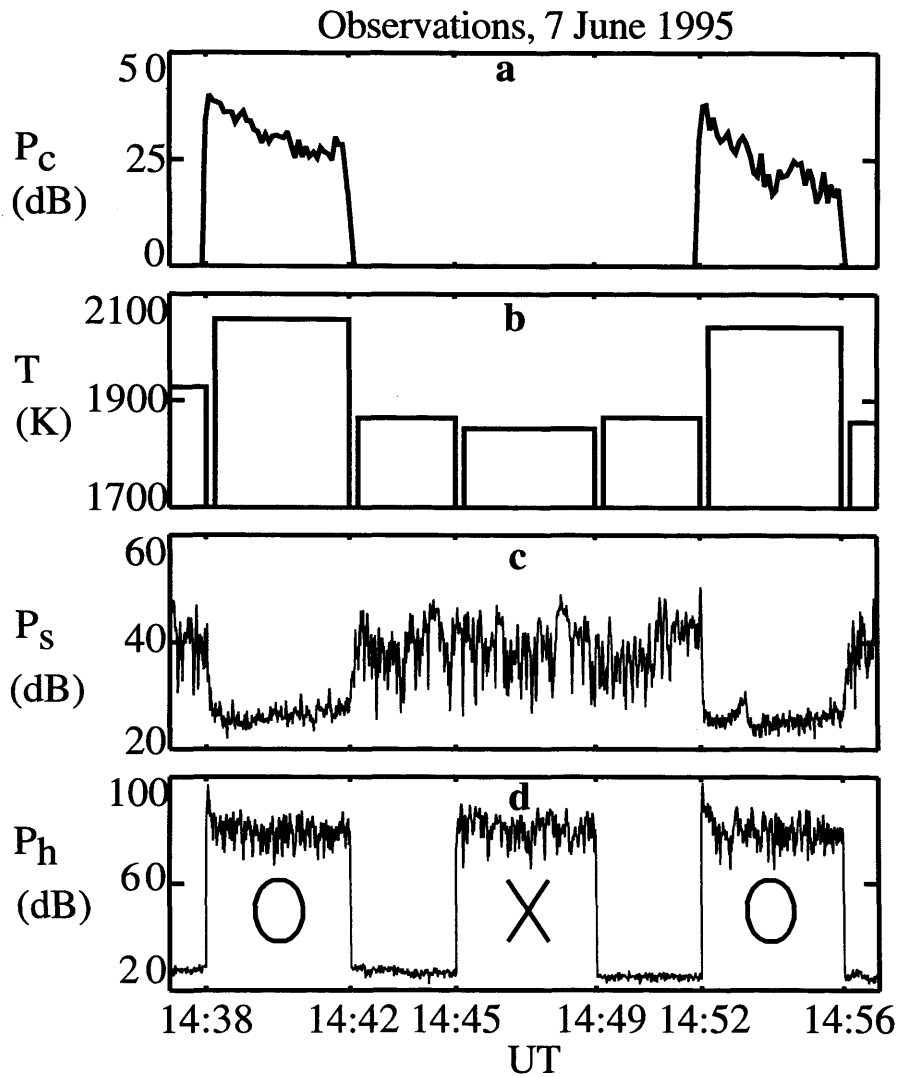


**Figure 4.5.** Data panels indicating, from the top, a) CUTLASS backscatter power, b) EISCAT UHF electron temperature measurements, c) 4.24 MHz diagnostic signal strength and d) the ionospherically reflected heater signal strength, all versus time (UT). (After Robinson *et al.* 1997).

and tristatic plasma flow velocity. The CUTLASS system has been utilised to measure backscatter power from both artificial and natural irregularities and line-of-sight flow velocity.

## Chapter 5

# *Artificial Modification of the Auroral E-region*

### 5.1 Introduction

The high-latitude E-region is a very dynamic and interesting region for study in its own right, where a number of natural plasma instabilities are excited in addition to the artificial modification effects which can be induced there. It is in the E-region that the properties of the constituent ions and electrons change with increasing altitude from a collisional to a collisionless regime. In addition, the orientation of the geomagnetic field in this region allows electric fields to map down to the E-region from the magnetosphere, and this has an important impact on the dynamics of the E-region and the currents that flow there.

At high latitudes and at heights of between 95 and 120 km, a current system known as the auroral electrojet flows in the ionosphere. Electric fields in this region can be as high as 100 mV/m and  $\mathbf{E} \times \mathbf{B}$  drift causes the electrons to flow through the ions at up to 2000 ms<sup>-1</sup>. When the electron flow speed exceeds a certain threshold, enhanced electron temperatures can occur. This enhancement can be explained by a modified two-stream instability known as the Farley-Buneman (FB) instability. One of the reasons for constructing the EISCAT heater at Tromsø, Norway, was that it lay directly beneath the auroral electrojet region. By operating the heater during a variety of natural conditions, the interaction between natural and artificial heating effects can be explored.

In this chapter, some recent results of high-latitude ionospheric modification experiments are presented. The European Incoherent SCATter (EISCAT) UHF radar was employed to measure electron temperature and density in the E-region, with electrojet electron flow speed being inferred from F-region measurements. A digital ionosonde facility at the EISCAT site known as a Dynasonde was utilised as an additional diagnostic. The results show significant artificial increases in electron temperature during times of low electron flow speed. There are also indications from the results that the ability of a high power radio wave to increase the electron temperature in the electrojet is reduced when the Farley-Buneman instability is excited. Furthermore, there is evidence that the radio wave can cause a reduction in electron temperature under certain conditions.

A self-consistent model of a high power radio wave propagating into the turbulent high latitude ionosphere is also presented. This model simulates a high power radio wave heating the lower ionosphere, utilising a similar method to previous authors (Tomko *et al.*, 1980; Meltz *et al.*, 1982; Milikh *et al.*, 1994). The

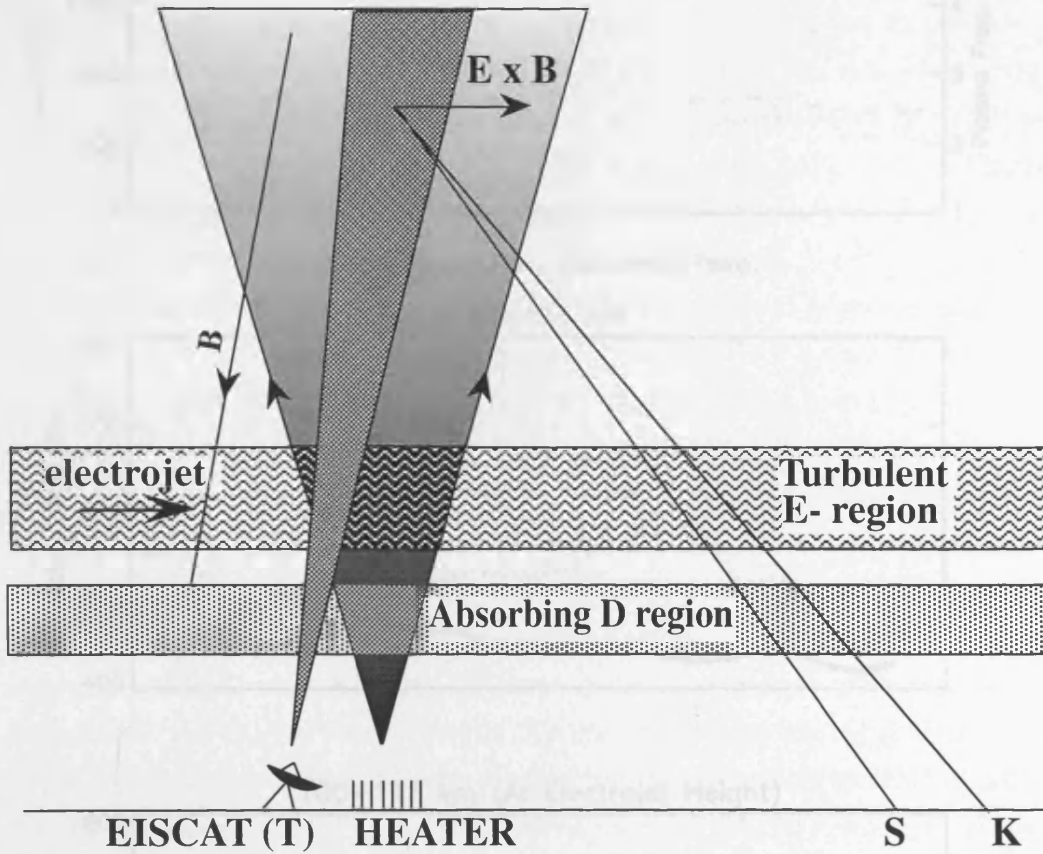
model presented here extends the work of previous authors by including the effect of natural electron heating in the auroral electrojet. The influence of this natural process on the efficiency of artificial radio wave heating has been investigated

## 5.2 Experimental procedure

Both the EISCAT UHF and the heating facilities were employed in an experimental campaign held between 5 and 8 February 1995. The experimental arrangement is depicted schematically in Fig. 5.1. The heater was operated with a power of between 80 and 90 kW per transmitter, which corresponds to 300 MW of ERP. The frequencies used were 4.04, 4.544 and 4.9128 MHz. A heater switching cycle of 2.5 minutes heater-on followed by 2.5 minutes heater-off was adopted. The polarisation was changed between O-mode and X-mode every 20 minutes. The response of the E-region to heating was monitored by the EISCAT UHF radar operating in a modified CP-1 mode. This mode points the transmitter vertically through the heated volume rather than along the field line, and the remote sites are utilised to intersect in the F-region. The alternating code from this program gave readings of electron density and temperature from 100 km upwards. The flow speed of the plasma in the F-region was determined using a tristatic measurement involving the EISCAT transmitter and receiver at Tromsø, and the two remote receivers at Sodankylå, Finland and Kiruna, Sweden. By assuming that the plasma in the F-region and the electrons in the E-region both move with the same  $\mathbf{ExB}$  drift velocity, the tristatic velocity is a measure of the electron flow speed in the electrojet.

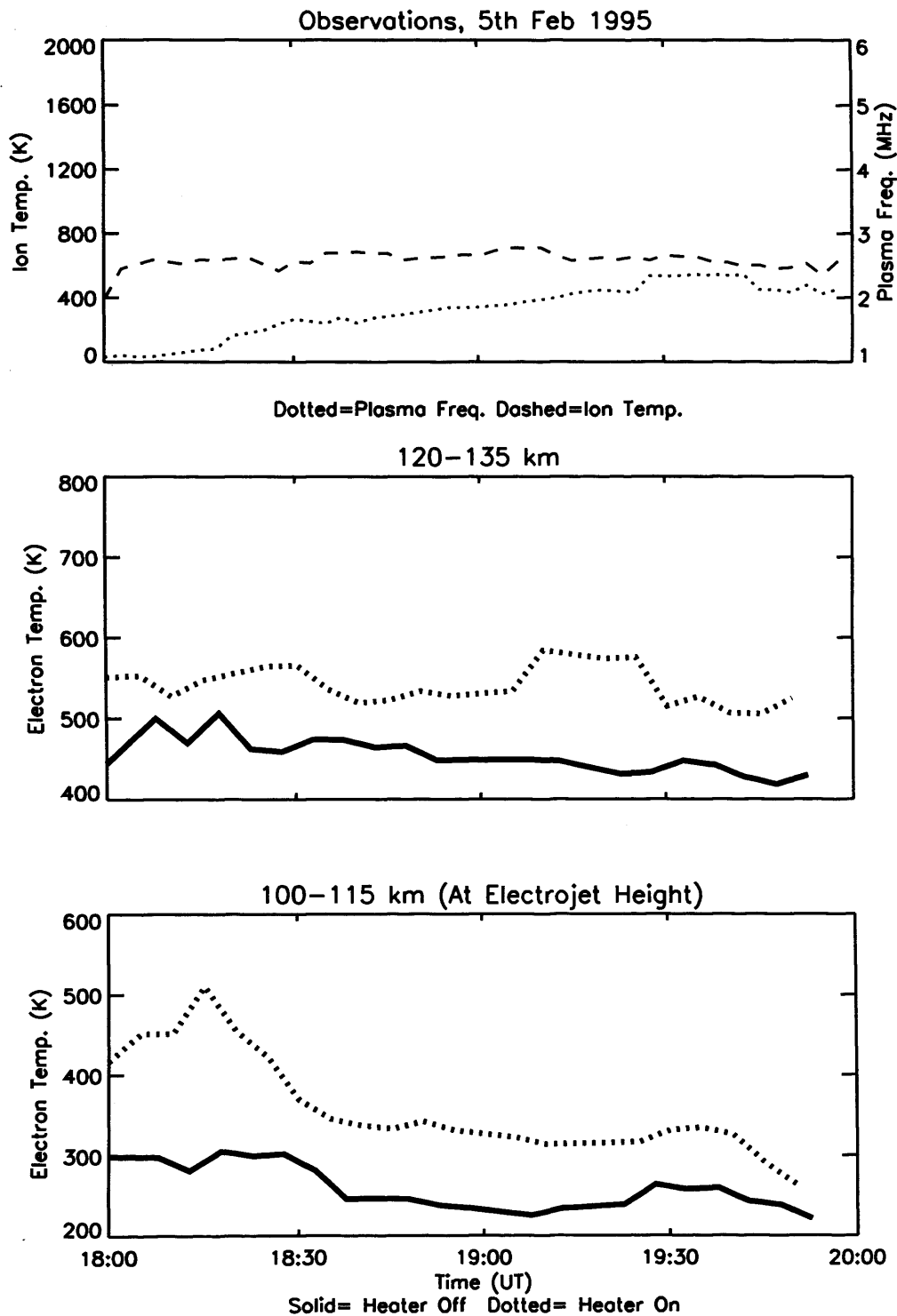
## 5.3 Experimental results

Fig. 5.2 presents results produced from EISCAT data for a heater experiment which ran from 1500 to 2000 UT on 5 February 1995. The bottom two panels display the electron temperature averaged over two height ranges: in the electrojet and just above the electrojet. The EISCAT data are integrated at 2.5 minute intervals to match the heater on-off cycle, and the graphs represent running averages over three of these intervals. The first 10 seconds of EISCAT data after each heater-on are not included in the integration, as ion-line overshoot (*e.g.* Robinson, 1989) can produce non-standard spectra which in turn give incorrect values. O- and X-mode heater cycles are not treated separately, as results obtained with the two different polarisations were similar. The solid lines are



**Figure 5.1.** Schematic representation of the experimental arrangement of the HF heater and the EISCAT UHF radars.

Figure 5.2. EISCAT observed ionospheric parameters from 1500 to 2000 UT on 22 February 1995. The dashed line is the 500 km virtual height, the temperature measured over height gates between 140 and 180 km. The dotted line in the top panel shows the plasma frequency from the 70 km height gate, normalized to ionospheric readings. The bottom two panels illustrate electron temperature over height ranges 120–135 km and 100–115 km. The dotted lines represent heater-on and the solid lines represent heater-off.

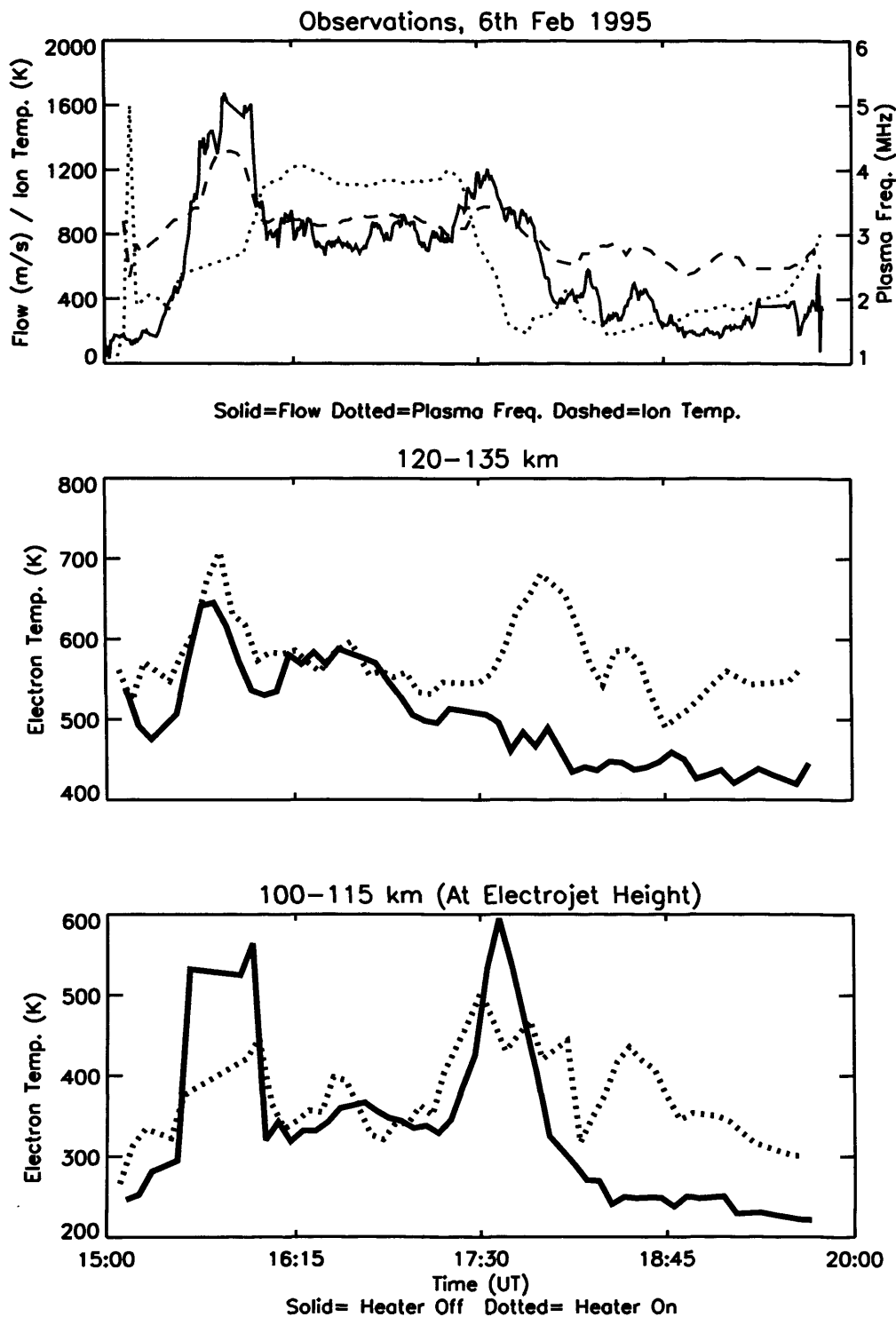


**Figure 5.2.** EISCAT alternating code measurements from 1800 to 2000 UT on 5 February 1995. The dashed line in the top panel presents ion temperature averaged over height gates between 140 and 180 km. The dotted line in the top panel represents the plasma frequency from the 111 km height gate, normalised to ionogram readings. The bottom two panels illustrate electron temperature over height ranges 120-135 km and 100-115 km. The dotted lines represent heater-on and the solid lines represent heater-off.

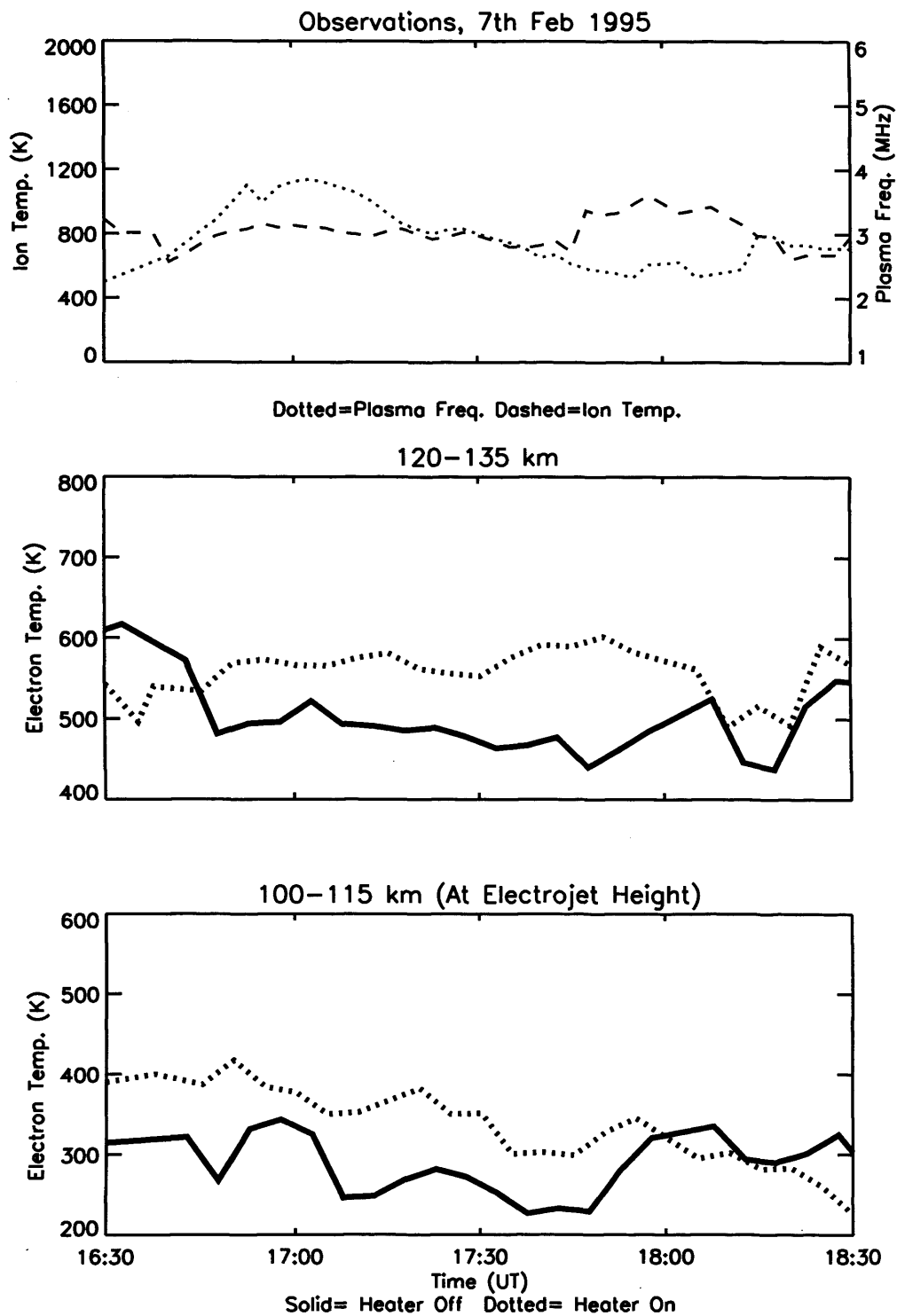
produced by joining together points representing data from heater-offs, and the dotted lines are produced by joining together points representing heater-ons. In this way simultaneous graphs are produced of natural conditions and artificially disturbed conditions. The dashed line in the top panel depicts ion temperature, averaged over height gates between 140 and 180 km, which acts as a guide to the flow speed during the experiment, as results for the tristatic velocity were not available. The dotted line in the top panel is the plasma frequency obtained from the alternating code data at the 111 km height gate. This parameter is plotted to indicate the nature of the propagation of the high power radio wave, as the wave will reflect when the frequency equals the plasma frequency. Absolute values of electron density or plasma frequency depend on the EISCAT system constant, so to obtain an accurate value the peak EISCAT plasma frequency is normalised to the peak obtained from ionogram data. Until about 1800 UT, the plasma frequency was very low in the electrojet, below 1 MHz. This resulted in a poor signal-to-noise ratio in the returned radar signal, and poor data was recorded as a consequence. After 1800 UT, the plasma frequency increased, and Fig. 5.2 displays the clearer results produced after this time. The heater produced electron temperatures above the background level in the E-region, as indicated by the bottom two panels. Between 120 and 135 km, the background temperature was about 450 K, and turning the heater on produced a temperature increase of order 100 K. At electrojet heights, the background temperature was low, about 250 K. The heater produced a similar effect to that at 120-135 km, increasing the background temperature by about 100 K.

Fig. 5.3 depicts the results for an experiment which ran from 1500 to 2000 UT on 6 February 1995. Tristatic velocities from the three EISCAT radars are utilised to provide a measurement of electron flow speed in the electrojet, smoothed by a running average over 10 minutes. The top panel shows the ion temperature and plasma frequency plotted with the flow speed. The ion temperature between 140 and 180 km peaked at 1550 and 1740 UT, which corresponded to the peak values of flow speed. Between 1530 and 1600 UT, and between 1725 and 1745 UT, the electron temperature in the electrojet fell by about 100 K when the RF heater was switched on. The top panel indicates that high flow speeds were present at these times. The heater frequencies used were 4.04 MHz between 1505 and 1717 UT and 4.544 MHz at all other times.

Fig. 5.4 presents the measurements for the heating experiment on 7 February 1995. The heater frequency was 4.544 MHz throughout, and the ERP was 300 MW. For most of this experiment the plasma frequency was very low, which produced a poor signal-to-noise ratio. The highest plasma frequency occurred



**Figure 5.3.** EISCAT measurements from 1800 to 2000 UT on 6 February 1995. The solid line in the top panel is the tristatic plasma speed. The dashed line in the top panel presents ion temperature averaged over height gates between 140 and 180 km. The dotted line in the top panel represents the plasma frequency from the 111 km height gate, normalised to ionogram readings. The bottom two panels illustrate electron temperature averaged over height ranges 120-135 km and 100-115 km. The solid lines indicate heater-off and the dotted lines indicate heater-on.



**Figure 5.4.** EISCAT alternating code measurements from 1630 to 1830 UT on 7 February 1995. The dashed line in the top panel presents ion temperature averaged over height gates between 140 and 180 km. The dotted line in the top panel represents the plasma frequency from the 111 km height gate, normalised to ionogram readings. The bottom two panels illustrate electron temperature averaged over height ranges 120-135 km and 100-115 km. The solid lines indicate heater-off and the dotted lines indicate heater-on.

around 1700 UT, and results for 1630 to 1830 UT are depicted in Fig. 5.4. During this time, temperatures were elevated by around 100 K in the electrojet and in the 120-135 km region, and the ion temperature was around 800 K.

Fig. 5.5 illustrates the results for 8 February. The heater was used at 300 MW ERP, and with frequencies of 4.04 MHz before 1717 UT, and 4.9128 MHz after 1730 UT. The ion temperature was very stable around 700 K, and the high plasma frequency produced a good signal-to noise ratio from the radar and because of this Fig. 5.5 depicts few missing data points. The heater caused an increase in temperature of about 50 K after 1700 UT, before 1600 there was little evidence of heating in or above the electrojet.

#### 5.4 Model calculations

A model has been developed to simulate the effect of RF heating on a naturally turbulent E-region. The model uses background density and temperature values from the MSIS 86 model for heights above 100 km, and values from Gurevich (1978) for lower heights. Electron density profiles are taken from Showen (1972) and Devlin *et al.* (1986). The model divides the ionosphere into a series of 1 km layers. For each layer the electron temperature is initially set equal to the background temperature and then the heating and cooling rates are calculated. Artificial heating is provided by the HF wave, natural heating effects are produced by frictional heating of the electrons as they flow through the neutrals and turbulent heating produced by the Farley-Buneman instability (see equations in chapter 2). Cooling effects are produced by the collisions of electrons with ions and neutrals (Schunk and Nagy, 1978). The rates are temperature dependent, either directly, as in the case of temperature dependent loss rates, or indirectly, through the temperature dependent collision frequency. The temperature dependent loss rates of Schunk and Nagy (1978) are contained in chapter 2. The temperature dependent electron neutral collision frequencies utilised in the model are

$$v_{N_2} = 2.33 \times 10^{-11} N(N_2) (1 - 1.21 \times 10^{-4} T_e) T_e, \quad (5.1)$$

$$v_{O_2} = 1.82 \times 10^{-10} N(O_2) (1 + 3.6 \times 10^{-2} T_e^{0.5}) T_e^{0.5}, \quad (5.2)$$

$$v_O = 8.9 \times 10^{-11} N(O) (1 + 5.7 \times 10^{-4} T_e) T_e^{0.5}, \quad (5.3)$$

$$v_H = 4.5 \times 10^{-9} N(H) (1 - 1.35 \times 10^{-4} T_e) T_e^{0.5}, \quad (5.4)$$

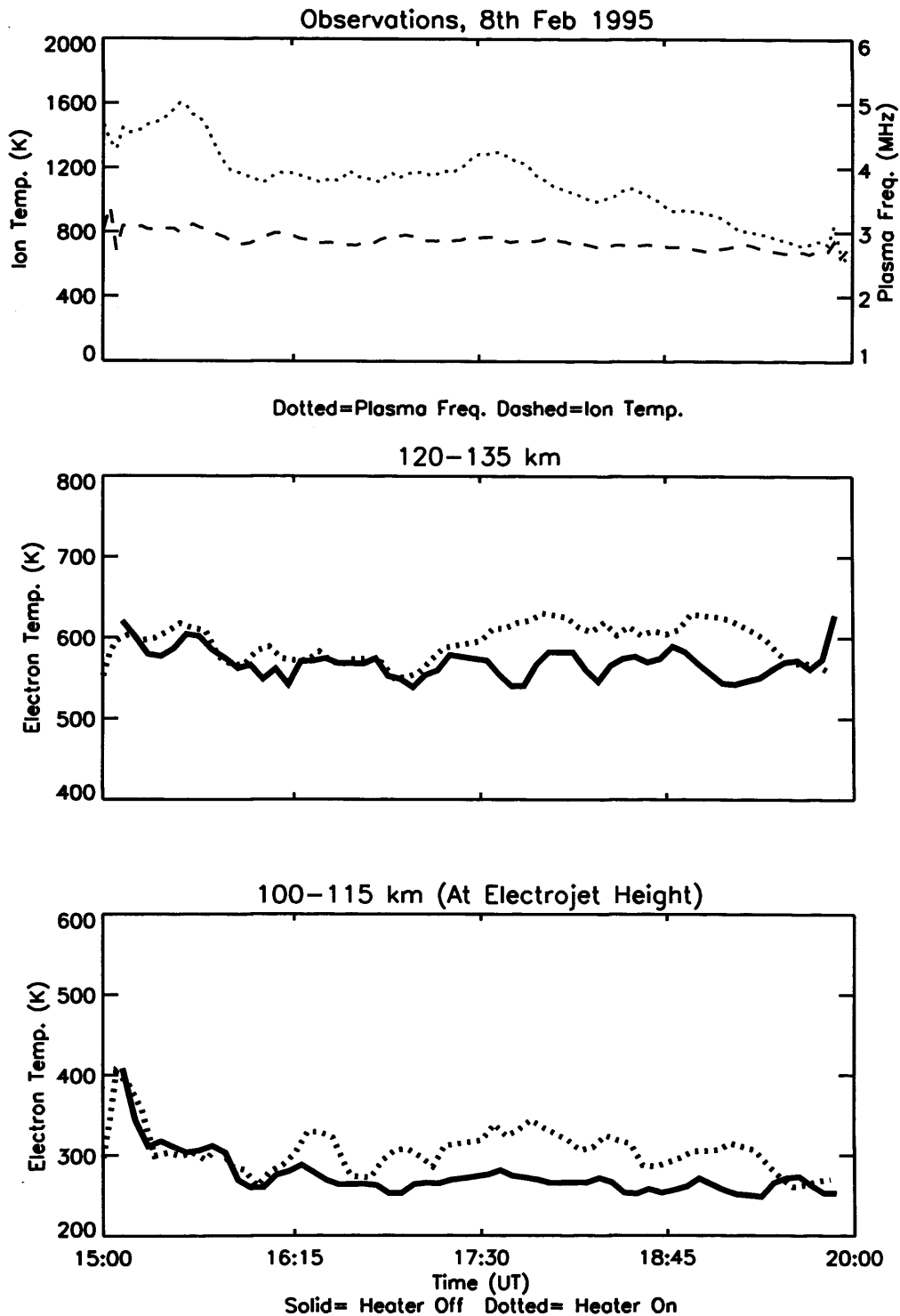


**Figure 5.5.** EISCAT alternating code measurements from 1500 to 2000 UT on 8 February 1995. The dashed line in the top panel presents ion temperature averaged over height gates between 140 and 180 km. The dotted line in the top panel represents the plasma frequency from the 111 km height gate, normalised to ionogram readings. The bottom two panels illustrate electron temperature averaged over height ranges 120-135 km and 100-115 km. The solid lines indicate heater-off and the dotted lines indicate heater-on.

$$v_{He} = 4.6 \times 10^{-10} N(He) T_e^{0.5}. \quad (5.5)$$

The rates are in  $\text{sec}^{-1}$  and  $N(x)$  is the density of species  $x$  in  $\text{cm}^{-3}$ . The electron neutral collision frequency is significant in a number of the elements of the model. It is contained in the artificial radio wave heating term, the Farley-Buneman heating term and the natural frictional heating term. The ion neutral collision frequency is significant for the calculation of the Farley-Buneman heating rate, and the terms utilised in the model are

$$v_{NO^+N_2} = 4.34 \times 10^{-10} N(N_2), \quad (5.6)$$

$$v_{NO^+O_2} = 4.28 \times 10^{-10} N(O_2), \quad (5.7)$$

$$v_{NO^+O} = 2.44 \times 10^{-10} N(O). \quad (5.8)$$

The model works in iterative steps, and the electron temperature is increased until a balance is reached between the heating and cooling terms, and a modified value for the electron density is calculated by considering temperature dependent recombination rates.

Consider the following equation for the change in electron density

$$\frac{dN_e}{dt} = q_n - l_n. \quad (5.9)$$

$\frac{dN_e}{dt}$  is the rate of change in electron density,  $q_n$  and  $l_n$  are the production and loss rates respectively. When there is balance between these terms, the change in density is zero and production equals loss. The production rate is controlled by solar radiation and is not affected by the RF wave, but the loss rate is temperature dependent, and is affected by RF heating. The loss rate is given by

$$l_n = \alpha N_e^2, \quad (5.10a)$$

$$\alpha = 8 \times 10^{-8} \left( \frac{300}{T_e} \right)^{0.55} + 2.1 \times 10^{-7} \left( \frac{300}{T_e} \right)^{0.85} \quad (5.10b)$$

where  $\alpha$  is the recombination rate. This rate is temperature dependant and depends on the ion species present, (Bailey and Sellek, 1990). As the production rate is unaffected by the heater, and production is equal to loss for equilibrium, the loss rates for heater on and heater off must be the same

$$\alpha_{T_{on}} N_{e_{on}}^2 = \alpha_{T_{off}} N_{e_{off}}^2, \quad (5.11)$$

and therefore

$$N_{e_{on}} = \sqrt{\frac{\alpha_{T_{off}}}{\alpha_{T_{on}}}} N_{e_{off}}. \quad (5.12)$$

Where the subscripts indicate heater on and off values. This formula is employed to calculate the heater modified density for each layer.

The absorption of the RF wave is calculated for each layer (Davies, 1990)

$$\kappa = 5.31 \times 10^{-6} \frac{N_e}{\mu} \frac{v}{v^2 + \omega^2}, \quad (5.13)$$

where  $\kappa$  is in  $m^{-1}$  and  $\mu$  is permeability of the medium. The density and collision frequency are increased by the RF wave, and in this way the wave causes increased absorption of itself, so-called self-absorption (e.g. Tomko, 1980). The electric field produced by the heater wave is given by

$$E = e^{-\int_{h_0}^h \kappa ds} \frac{9.5 \sqrt{ERP}}{H}, \quad (5.14)$$

where  $ERP$  is in MW and is typically 200-300 MW for the Tromsø heater.  $H$  is the height in km. The integral represents the absorption from the base of the ionosphere to the height being considered. In the model,  $\kappa$  is calculated for each level and multiplied by the layer thickness. Adding together these terms for all layers below the one being considered gives the total absorption. The calculated electric field is then used to give the heating rate due to the RF wave. A diagram representing the calculations involved in the model is presented in Fig. 5.6.

Fig. 5.7 presents three electron density profiles that are used with the model. The profiles are used to illustrate the effect of different ionospheric conditions. The 'nighttime' and the 'enhanced E-region' profiles provide a contrast in E-

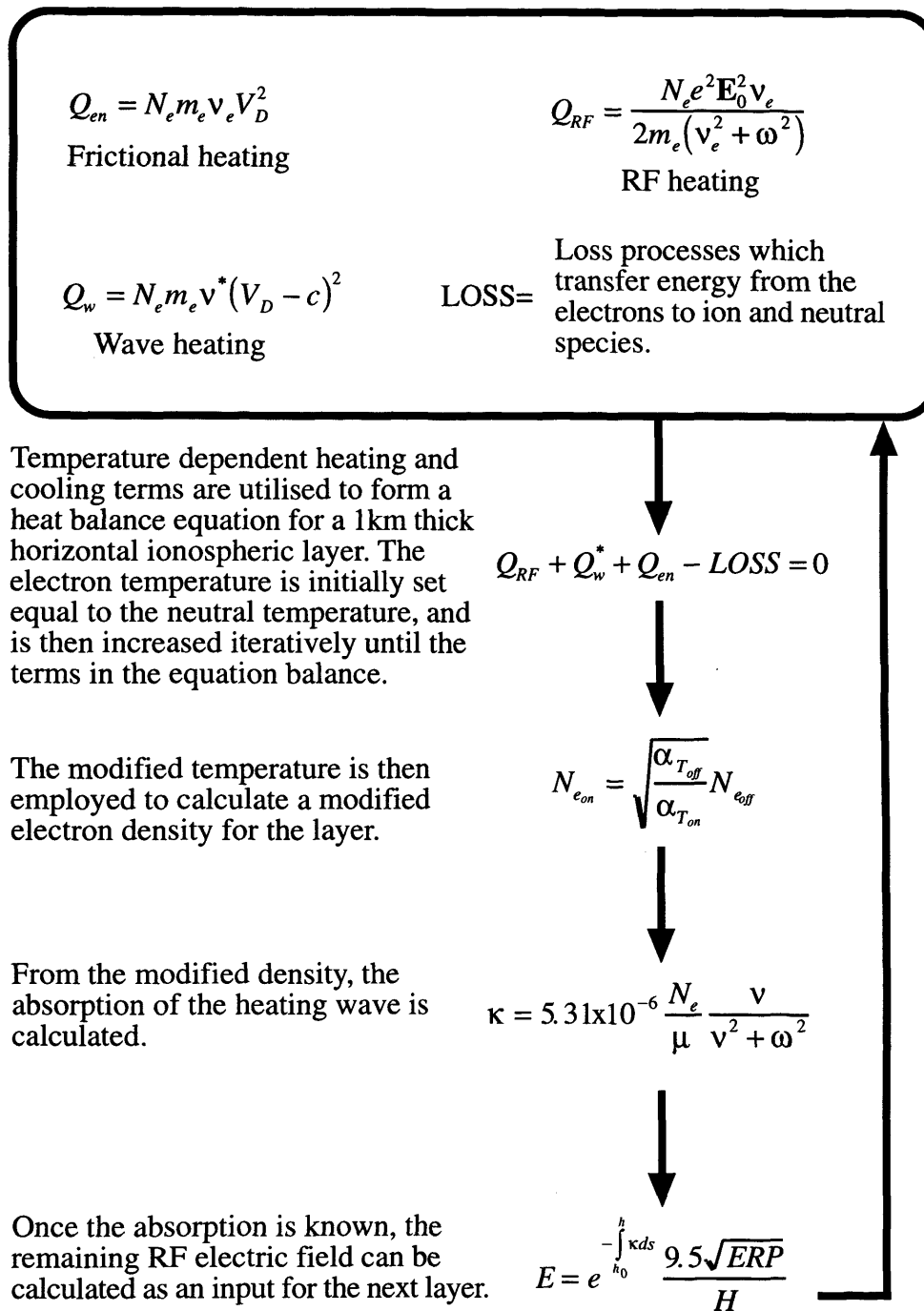


**Figure 5.6.** Diagram representing the calculations performed by the computer model. The model calculates values of electron temperature and density at 1km steps to produce vertical profiles through the ionosphere.

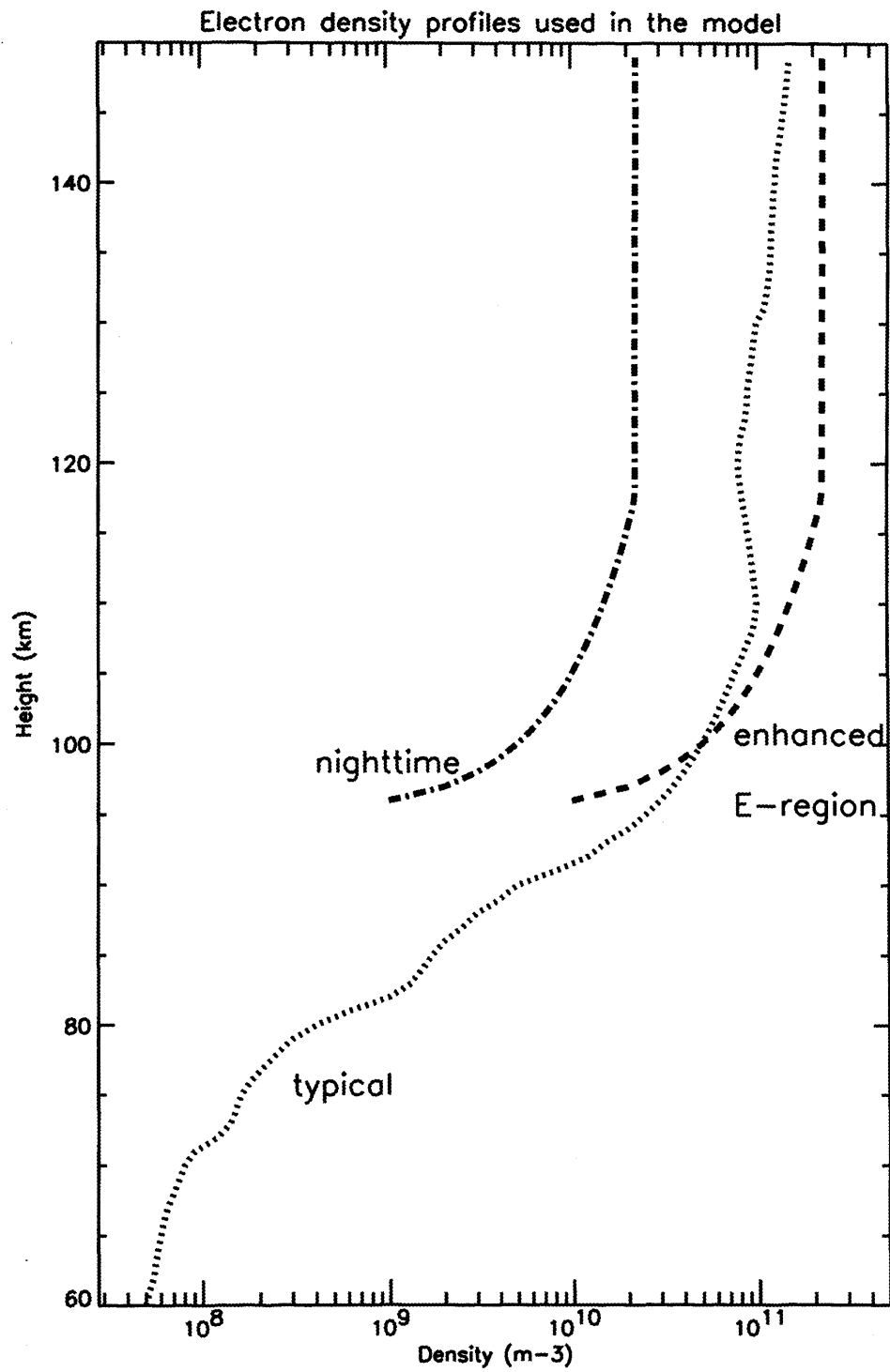


**Figure 5.7.** Electron density profiles. The 'typical' profile is from Showen (1972). The 'enhanced E-region' and 'nighttime' profiles are from Devlin *et al.* (1986).

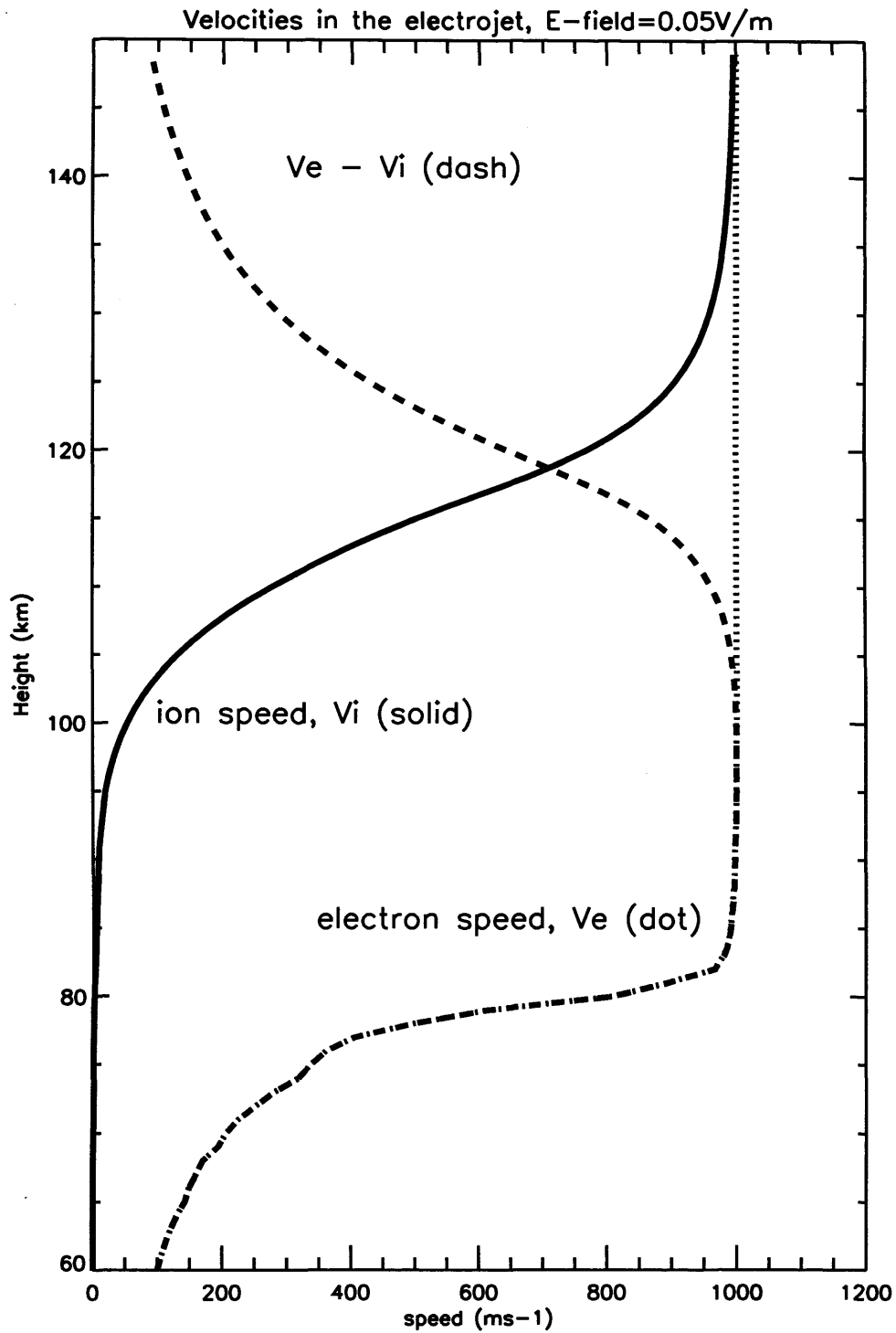
region densities, while the 'typical' profile depicts an ionosphere with a D-region present.

The model utilises the natural electric field in the ionosphere as an input, and calculates the drift of the electrons through the ions due to  $\mathbf{E} \times \mathbf{B}$  drift. Fig. 5.8 depicts the velocities of the ions and electrons when acted upon by a model electric field of 50 mV/m. The 'typical' model electron density profile, as depicted in Fig. 5.7, is utilised as it employs an ionosphere with a D-region present. In the D-region, the collision rates are high, and the electrons and the ions do not flow. With increasing height, the collision frequencies change. Above 70 km the electron flow speed increases considerably, saturating at the collisionless flow speed of  $1000 \text{ ms}^{-1}$  at around 85 km. The ion flow speed becomes significant at around 100 km, and reaches saturation at around 145 km.

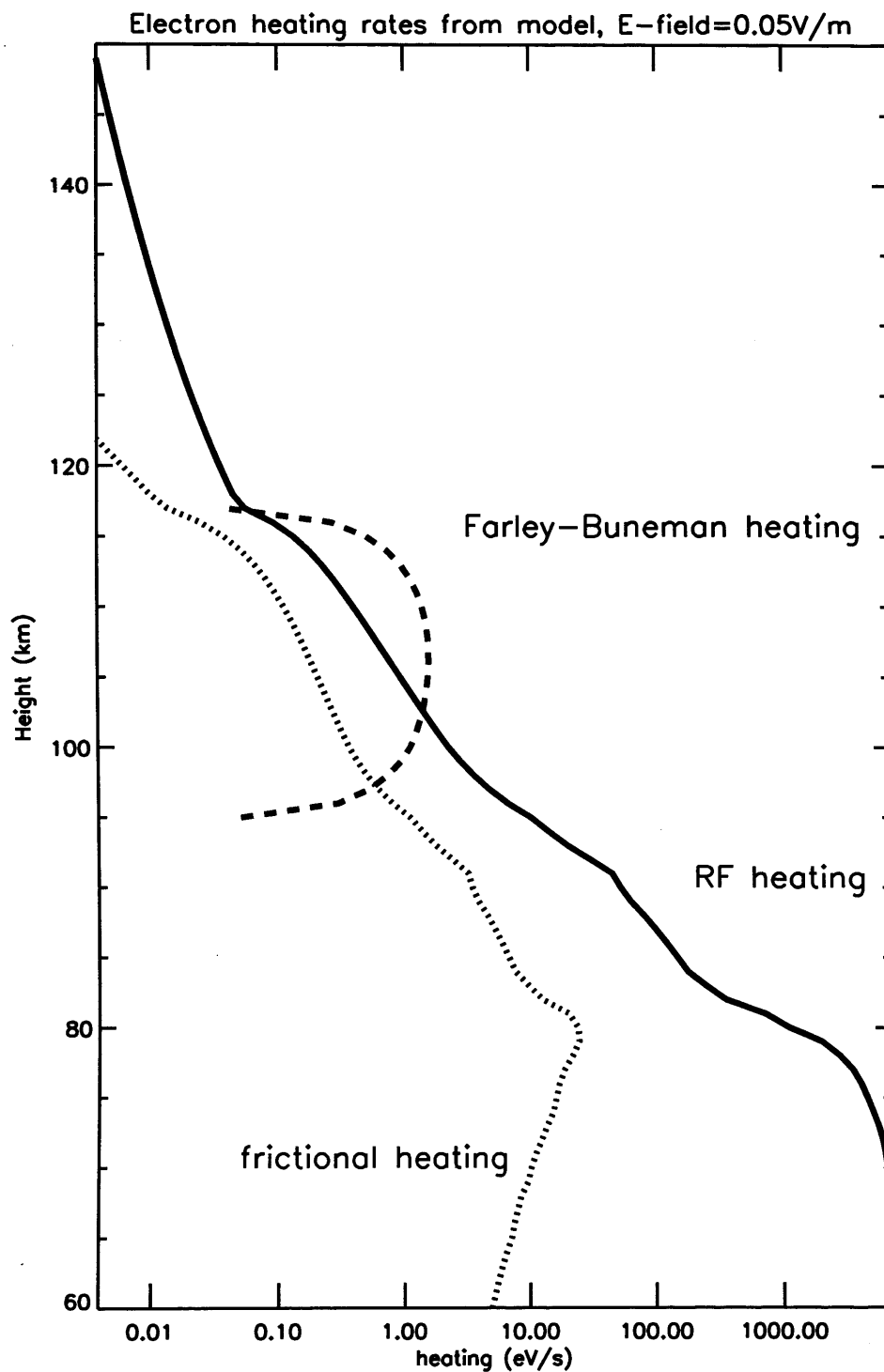
Fig. 5.9 illustrates the heating rates produced when the typical profile is utilised as a starting point for the model. The heater ERP is 300 MW, which corresponds to typical ERP values produced by the Tromsø heater, and the electric field is 0.05 V/m. The RF wave produces the most significant heating low down in the ionosphere, and this contribution becomes less significant with increasing height. The heating due to the FB instability is centred on 100 km, and becomes insignificant above and below this height. The frictional heating is largest in the D-region.

Fig. 5.10 depicts the electron temperature changes produced by the heating rates when employing the typical profile. The graph illustrates the background temperature, the electron temperature when there is only RF heating, the temperature when there is only natural heating, and the temperature when there is both RF and natural heating. The RF wave produces a 1000 K increase in the D-region, and at electrojet heights the FB heating causes a 200 K increase in electron temperature. When there is only RF heating present, there is a temperature increase of order 100 K at electrojet heights.

Fig. 5.11 depicts the fractional electron temperature change when the heater is switched on. The three panels are for the three different electron density profiles (Fig. 5.7), and all three demonstrate that the fractional temperature change is less when the heating due to the electrojet is included. The fractional temperature increase is greatest for the nighttime profile and the typical profile shows a smaller temperature increase. The graph for the enhanced E-region profile is the same as the nighttime profile at low altitudes, but indicates a smaller contribution from the RF wave as height increases. Fig. 5.12 presents the fractional density increase for the three profiles, and the graphs have a similar shape to those for temperature.



**Figure 5.8.** Model values of electron flow speed, ion flow speed and electron flow speed minus ion flow speed, under the influence of a natural electric field of 0.05 V/m.



**Figure 5.9.** Model values of electron heating rates, utilising a natural electric field of 0.05 V/m, the 'typical' profile, a heater frequency of 5 MHz and a heater ERP of 300 MW. The dashed line represents heating due to Farley\_Buneman turbulence, the solid line represents RF heating and the dotted line represents frictional heating between the electrons and neutrals.

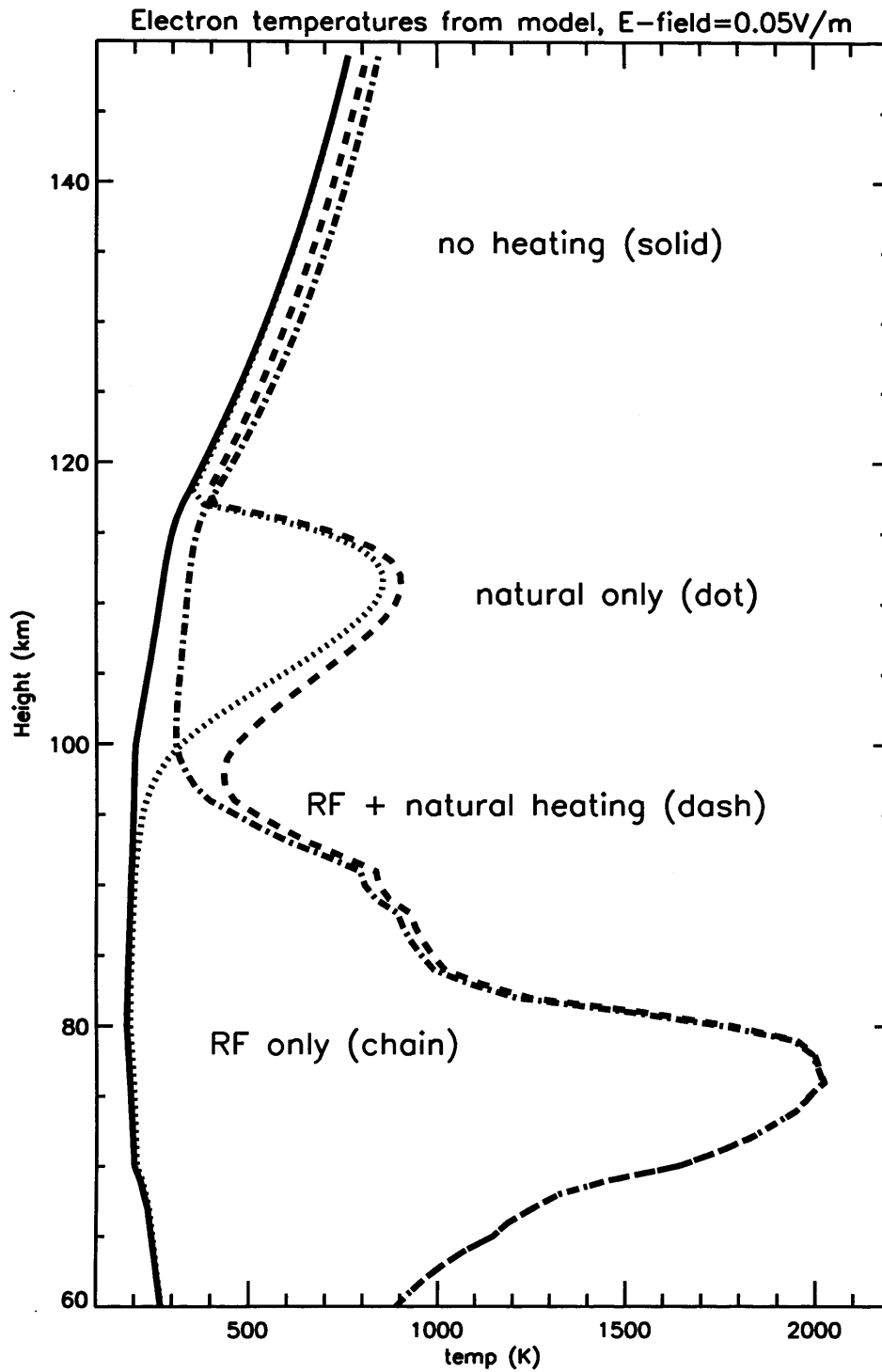


**Figure 5.10.** Model values of electron temperature, utilising a natural electric field of 0.05 V/m, the 'typical' profile, a heater frequency of 5 MHz and a heater ERP of 300 MW. The chained line represents the electron temperature when only RF heating is present, the dotted line represents the temperature when only natural turbulent heating is present, the dashed line represents the temperature when both natural and RF heating are present and the solid line represents the undisturbed background electron temperature.

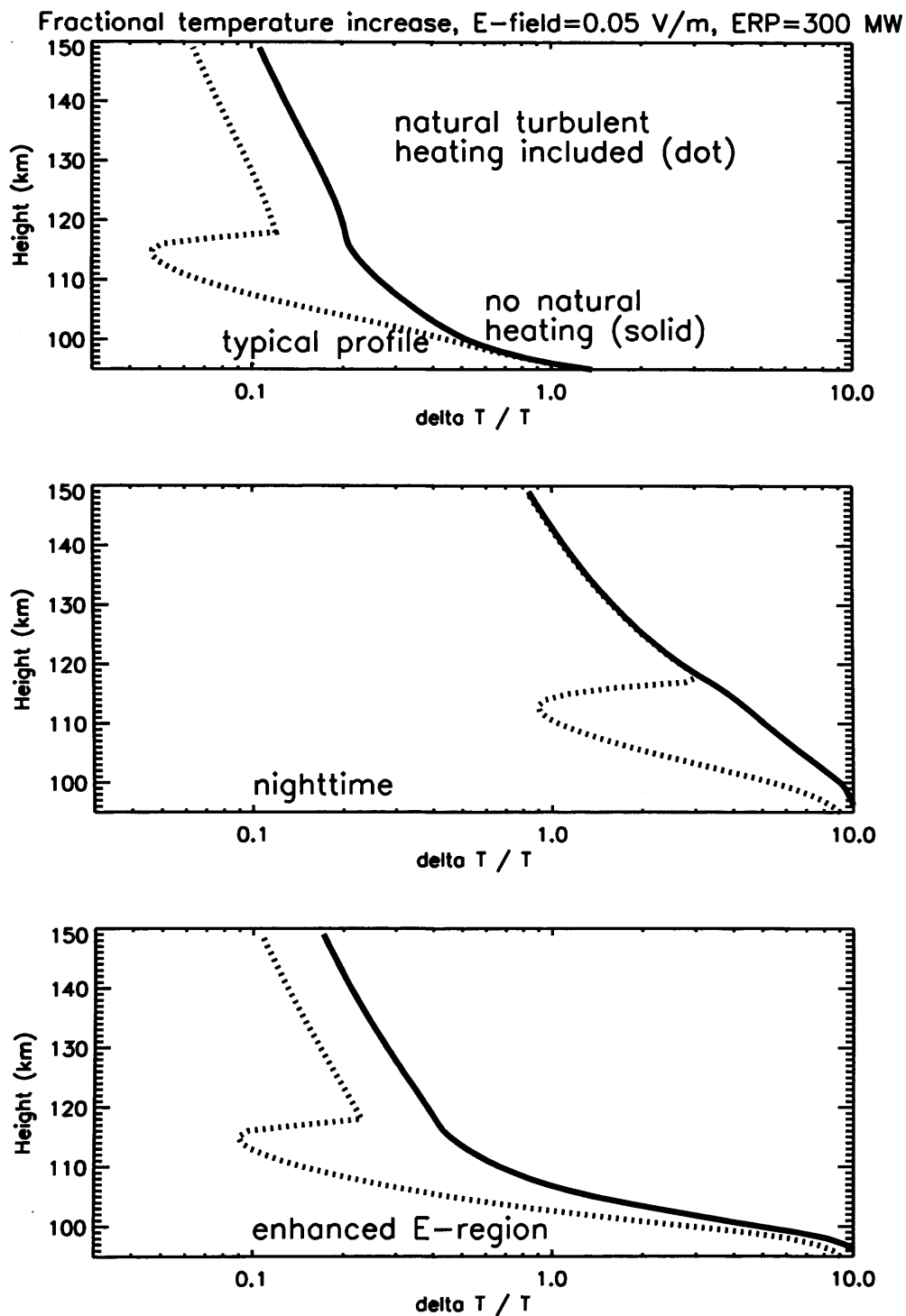


**Figure 5.11.** Model values of the fractional change in electron temperature when the heater is switched on, utilising a natural electric field of 0.05 V/m, a heater frequency of 5 MHz and a heater ERP of 300 MW. The top panel employs the 'typical' profile, the middle panel employs the 'nighttime' profile and the bottom panel employs the 'enhanced E-region' profile. The dotted lines indicate the change when natural turbulent heating is present and the solid lines indicate the change when only RF heating is present.

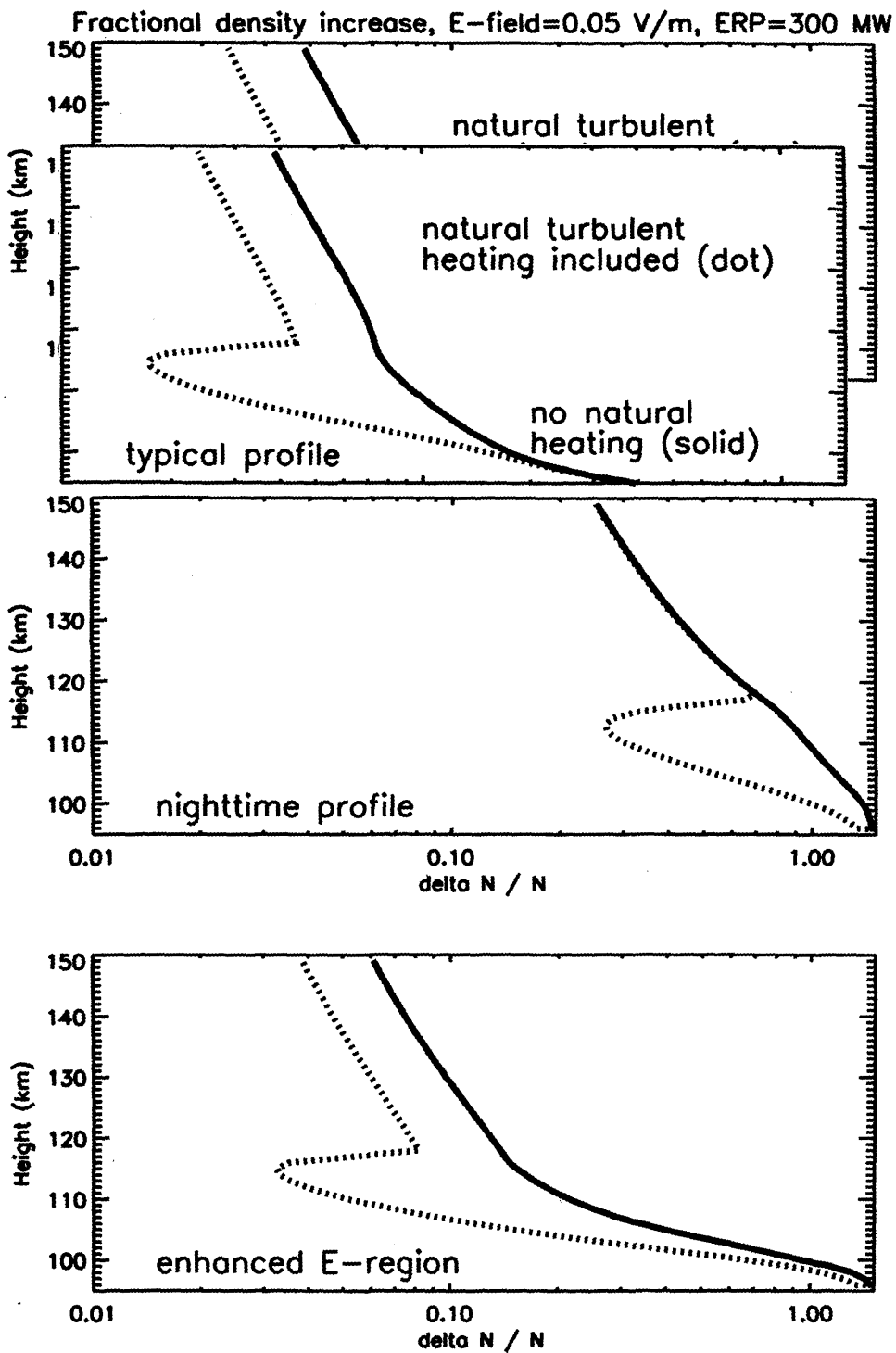


**Figure 5.12.** Model values of the fractional change in electron density when the heater is switched on, utilising a natural electric field of 0.05 V/m, a heater frequency of 5 MHz and a heater ERP of 300 MW. The top panel employs the 'typical' profile, the middle panel employs the 'nighttime' profile and the bottom panel employs the 'enhanced E-region' profile. The dotted lines indicate the change when natural turbulent heating is present and the solid lines indicate the change when only RF heating is present.

Fig. 5.13 illustrates the fractional increase in electron temperature when the heater is switched on, for a heater ERP of 1 GW. This is in contrast to the 300 MW ERP which is utilised to produce Fig. 5.11. Fig. 5.14 employs the same ERP as Fig. 5.11, but the electric field which produces the natural turbulent heating is set to  $0.1 \text{ Vm}^{-1}$  instead of  $0.05 \text{ Vm}^{-1}$ .

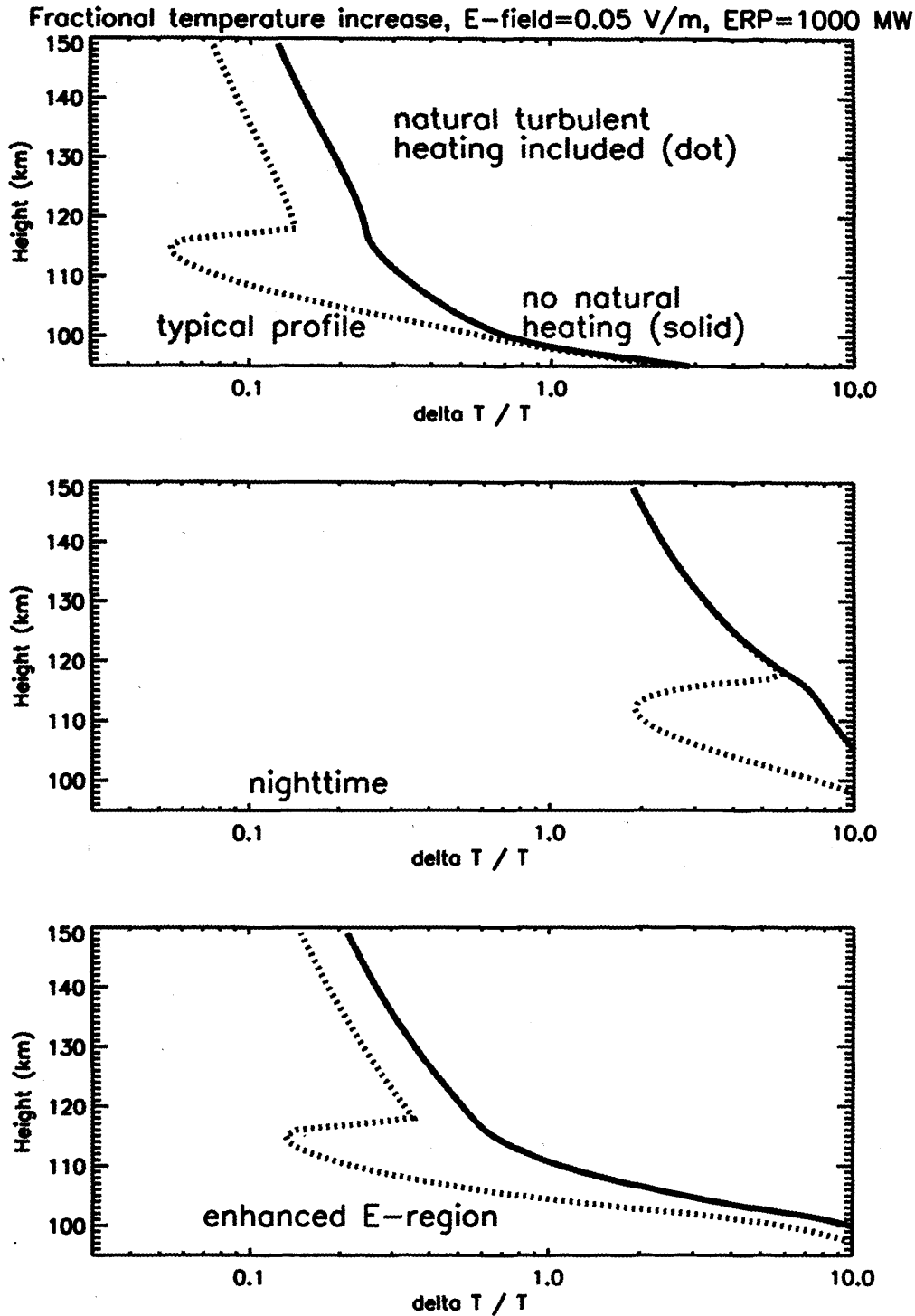
Fig. 5.15 illustrates a comparison between EISCAT and model values of electron temperature for 6 February 1995. The EISCAT values are 2.5 minute integrations of electron temperature for heater off, averaged over range gates between 100-115 km. In this case the model does not use a value for the natural electric field to work out the  $\mathbf{ExB}$  drift, but instead uses flow speed values produced by EISCAT at the same time as the temperature readings. Starting from model values of background electron temperature, the model produces values for naturally enhanced electron temperature by calculating the amount of frictional and Farley-Buneman heating.

## **5.5 Discussion and conclusions**

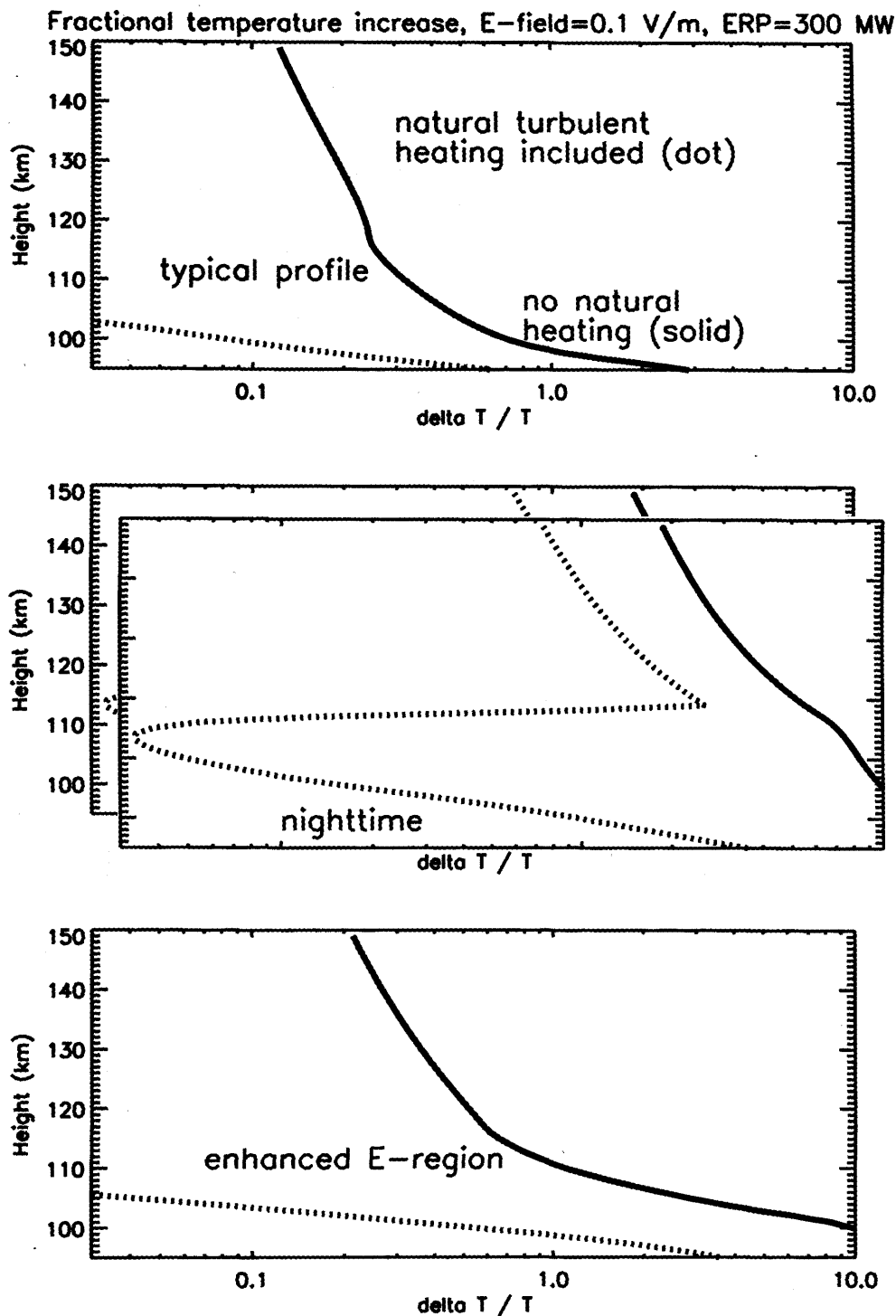
### **5.5.1 Discussion of observations**

Fig. 5.2 illustrates that plasma frequency reached 2 MHz at around 1830 UT on 5 February 1995. This corresponded to underdense heating, since the heater wave had a frequency of 4.544 MHz. The plot indicates a stable ion temperature, consistently below 1000 K, this suggests that the electrojet was not present, since high flow speeds lead to elevated ion temperatures. At electrojet heights, the background temperature was low, about 250 K. This lack of natural temperature enhancement is further evidence that the electrojet was not flowing. The heater produced a similar effect to that at 120-135 km, increasing the background temperature by about 100 K. This consistent temperature increase through the E-region is to be expected from underdense heating. The wave was not reflected and the low density does not cause significant absorption of the wave.

Fig. 5.3 indicates that the ion temperature between 140 and 180 km peaked at 1550 and 1740 UT on 6 February 1995, which corresponded to the peak values of flow speed. This supports the use of ion temperature as a guide to the strength of the flow when tristatic velocities are not available. Between 1530 and 1600 UT, and between 1725 and 1745 UT, the electron temperature was naturally increased by 200 K due wave turbulence produced by the excitation of the Farley-Buneman instability. However, when the heater was switched on during these naturally disturbed conditions, the electron temperature in the electrojet fell by about 100



**Figure 5.13.** Model values of the fractional change in electron temperature when the heater is switched on, utilising a natural electric field of 0.05 V/m, a heater frequency of 5 MHz and a heater ERP of 1000 MW. The top panel employs the 'typical' profile, the middle panel employs the 'nighttime' profile and the bottom panel employs the 'enhanced E-region' profile. The dotted lines indicate the change when natural turbulent heating is present and the solid lines indicate the change when only RF heating is present.



**Figure 5.14.** Model values of the fractional change in electron temperature when the heater is switched on, utilising a natural electric field of 0.1 V/m, a heater frequency of 5 MHz and a heater ERP of 300 MW. The top panel employs the 'typical' profile, the middle panel employs the 'nighttime' profile and the bottom panel employs the 'enhanced E-region' profile. The dotted lines indicate the change when natural turbulent heating is present and the solid lines indicate the change when only RF heating is present.

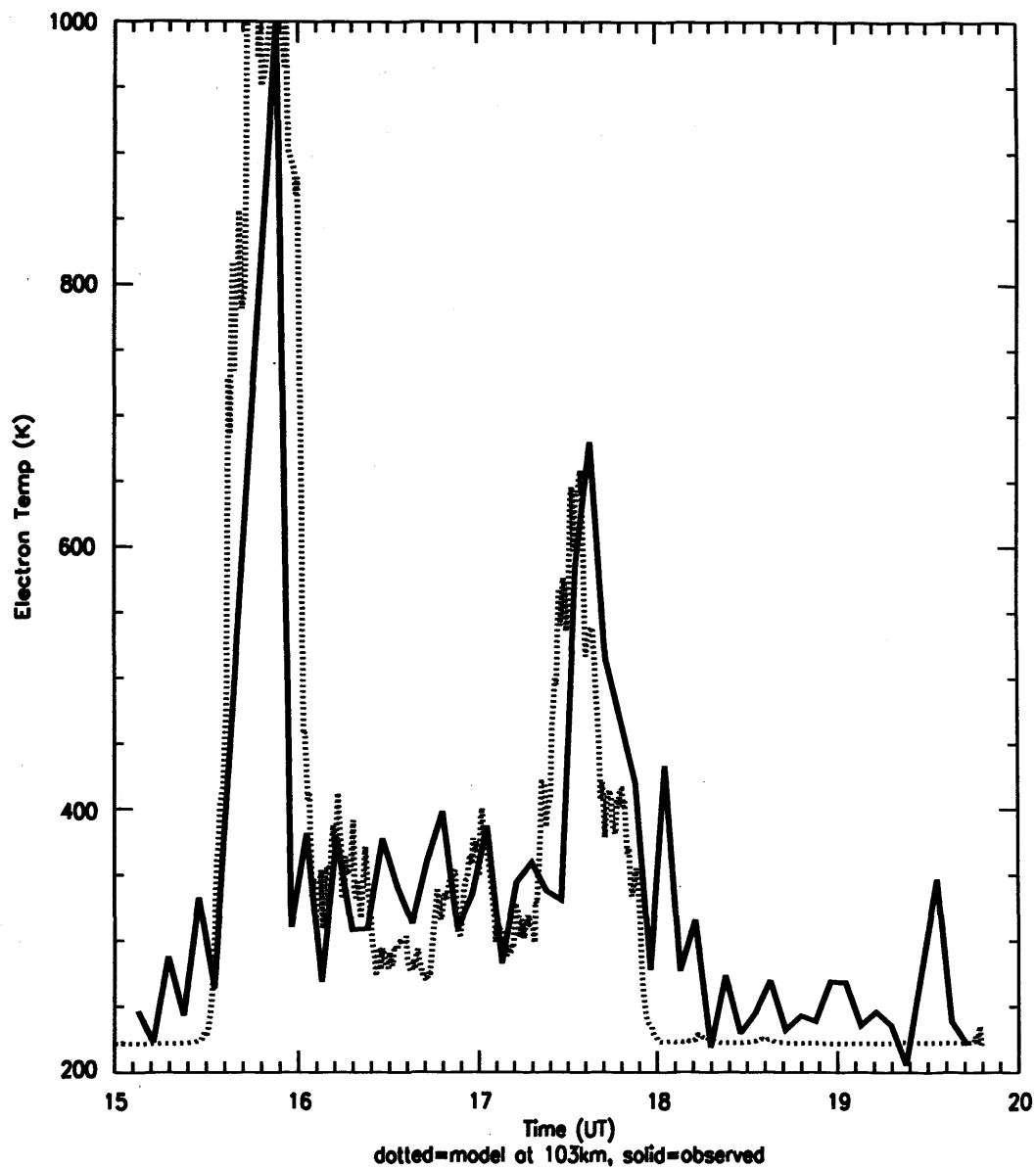


**Figure 5.15.** The dotted line depicts model electron temperature values calculated at 103 km, which utilise electron flow speed data in the electrojet, inferred from F-region measurements of plasma flow. The solid line illustrates naturally enhanced electron temperatures produced directly from analysis of EISCAT data.

K. This meant that the temperature was still around 400 K, and therefore still greater than the value during undisturbed conditions, but less than the naturally disturbed temperature. This is evidence of heater induced cooling. The theory of Robinson (1994) suggests that a high power radio wave can have a direct effect on the Farley-Buneman instability. When the heater was switched on the natural instability was quenched, and the naturally occurring temperature increase, for this data around 200 K, did not occur. The heater still provided an energy input into the ionosphere, and this still produced a temperature increase of around 100K, but this was insufficient to overcome the lack of natural heating and the net result was that an electron temperature decrease of around 100 K was observed by the radar. There is no problem of energy conservation, as the energy which usually produces the natural temperature increase was still contained within the electrojet, it was simply not converted into thermal energy.

The heater frequencies utilised on 6 February were 4.04 MHz between 1505 and 1717 UT and 4.544 MHz at all other times. Fig. 5.3 depicts plasma frequencies of this order in the electrojet between 1550 and 1740 UT. When cooling was detected, the electron concentration was in the process of changing across these densities, so the radio wave reflected over a range of heights in the electrojet. This produced a strong effect, which is consistent with cooling being seen at these times. Between 1550 and 1740 UT, the flow speed was above the threshold and the plasma frequency was consistent with a strong interaction. The graph does indicate that heating efficiency was reduced at this time but there is no cooling apparent. This is probably because the density was stable, and the radio wave reflected at a narrow height range. The radar has a resolution of around 5 km in alternating code mode, so if an interaction was occurring at a very narrow height range the effect would be smoothed out in the data. Before 1530 UT and after 1800 UT the flow speed dropped below the threshold. During these times conventional artificial heating of the electrons occurred, and the electron temperature increased by about 100 K when the heater was switched on.

The electron temperature plot between 120 and 135 km in Fig. 5.3 indicates no evidence of heater-induced cooling. This is to be expected, as the ions move with the electrons at this height and so the instability is not excited. This is further demonstrated by the fact that there is little evidence of natural turbulent heating at this height range. Between 1600 and 1730 UT, Fig. 5.3 illustrates that the plasma frequency in the electrojet region was high, around 4 MHz. This high density caused absorption and reflection of the RF wave in the electrojet. As a consequence, there was little artificial heating above the electrojet at this time, as depicted in the middle panel of Fig. 5.3. After 1730 UT, the plasma frequency in

the electrojet region dropped to around 2 MHz. This frequency was far below that of the wave and so very little absorption occurred in the electrojet. The heater wave was therefore able to propagate into the upper E-region, producing an increase in the natural temperature of order 100 K between 120 and 135 km.

Several interesting natural ionospheric phenomena are present in Fig. 5.3. The increase observed in plasma frequency, and hence electron density, which occurred in the E-region at around 1550 UT was accompanied by a significant increase in the flow speed. During the period 1550 to 1740 UT the flow speed fell but remained well above the threshold for the instability, while the density remained high. At around 1740 UT the density fell, and the flow speed increased. By about 1800 UT the flow speed fell below the threshold for the instability. These observations indicate that the changes in the natural electron density, both the increase at 1550 UT and the decrease at 1740 UT, were accompanied by a significant increase in the electron flow speed. This natural phenomenon provided an ideal environment for artificial cooling to occur. The high flow speed provided the natural turbulence and the electron density gradient produced a strong interaction in the electrojet. These natural conditions were not repeated at any other time during the campaign, and no other periods of artificial cooling were observed. It is possible that artificial cooling can only occur under these specific conditions, and that simply waiting for conditions of high electron flow are not enough to guarantee cooling when the heater is switched on,

Fig. 5.4. depicts an electron temperature increase of around 100 K in the electrojet and in the 120-135 km region, and the ion temperature was around 800 K. These observations are consistent with underdense heating of a quiet E-region, similar to the conditions seen after 1830 UT on 5 February.

The ion temperature depicted in Fig 5.5 is very stable at around 700 K, indicating that the flow speed in the electrojet was very small. The artificial increase in temperature of about 50 K was not as high as on previous days because the RF wave suffered absorption due to the high electron density. Before 1600 UT the plasma frequency was around 5 MHz, this caused reflection and high absorption of the RF wave, and the result is that there was little evidence of heating in or above the electrojet.

### **5.5.2 Discussion of model results**

In the D-region, both ions and electrons are collisional, and there is no flow. In the lower E-region, the ions are still collisional, but the electrons begin to move with an  $E \times B$  drift. Higher up in the E-region the ions become collisionless and

flow with the electrons. As Fig. 5.8 illustrates, the overall effect of this is to produce a region centred on 100 km where the electrons flow through the ions, this is the electrojet region. Values of up to  $100 \text{ ms}^{-1}$  are used in the model, and this produces a flow of  $2000 \text{ ms}^{-1}$ . The model considers the underdense heating case, where the RF wave does not have a direct effect on the instability. However, the RF wave still has an indirect effect on the instability because it changes the collision frequency.

Fig. 5.9 illustrates the heating rates produced when the typical profile is utilised as a starting point for the model. The RF wave produces the most significant heating low down in the ionosphere. This contribution to the overall effect gradually becomes less significant as the wave is absorbed with increasing height. The heating due to the FB instability only becomes significant at 100 km, where the electrons become collisionless. The frictional heating is largest in the D-region, but heating in that region is dominated by the RF wave, and so the frictional heating is the least significant of the heating rates.

Fig. 5.10 demonstrates that the RF wave produces a 1000 K increase in the D-region, and this agrees with previous models of artificial D-region heating (see chapter 2, Fig. 2.1). At electrojet heights the FB heating causes a 200 K increase in electron temperature. This is in agreement with the natural temperature increase observed on February 6 (Fig. 5.3). When there is only RF heating present, there is a temperature increase of order 100 K at electrojet heights. This is consistent with the experimental temperature increases seen on 5 and 7 February, when electron flow speeds were low.

In Fig. 5.11, the fractional temperature increase is greatest for the nighttime profile, because the low electron density means that the RF wave is not absorbed significantly. The typical profile has a low fractional increase in temperature at low E-region altitudes because of D-region absorption. The graph for the enhanced E-region profile is the same as the nighttime profile at 95 km, as there is no D-region present for either of these model profiles. Above 100 km, the typical and enhanced profiles produces similar effects, as the E-region electron densities for these two profiles are similar.

The artificial fractional increase in temperature is obviously highly sensitive to the initial natural temperature before heater on. If the initial temperature is very high, then a large artificial increase in temperature may only correspond to a small fractional temperature increase. When the Farley-Buneman instability is excited, it produces a large natural increase in the electron temperature, and so when the heater is switched on, a large artificial temperature increase may only result in a small fractional increase. Therefore, it is tempting to interpret the data

in Fig. 5.11 in terms of high background temperatures producing the low fractional temperature increase under naturally turbulent conditions, rather than an actual reduction in the efficiency of the HF heating. However, it can be demonstrated that this is not the case by considering the data in Fig. 5.12, where the fractional increase in density is plotted. Unlike electron temperature, the electron density is not significantly increased by natural turbulent heating. This means that any observed difference between RF heating during quiet and disturbed natural conditions is due to the efficiency of the RF heating. Fig. 5.12 demonstrates that the fractional increase in density is reduced under naturally disturbed conditions, thus confirming that the efficiency of the RF heating is reduced.

The increase in ERP illustrated in Fig. 5.13 causes an enhanced fractional temperature increase, although the effect is not linear. The ERP is increased by a factor of 3 compared to the ERP utilised to produce Fig. 5.11, but the enhancement in the fractional temperature increase is typically of order half. The height dependence of the fractional temperature increase is similar for 300 MW and 1 GW.

In Fig. 5.14 the value of the natural electric field is increased in comparison to the value utilised to produce Fig. 5.11. The heater produces a reduced fractional temperature increase for this high level of natural heating, demonstrating an even more marked difference between quiet and disturbed conditions. For the typical and enhanced profiles, an artificial temperature increase is no longer observed above 105 km.

The fractional changes in temperature and density illustrated in Figs. 5.11-5.14 are indicative of the conductivity changes which are induced by the RF wave in the electrojet. Modulation of the electrojet current produces artificial VLF, ELF and ULF waves. The amplitude of the resulting waves depends on the perturbation level of the density and the temperature. Figs. 5.11-5.14 indicate that under conditions of high flow, the perturbation level is suppressed, which could reduce the efficiency of the production of artificial low frequency waves.

Fig. 5.15 depicts good agreement with the data for a model height of 103 km. This is a good test of the effectiveness of the model in reproducing real effects. In addition, it provides confirmation that the natural electron temperature effects illustrated in Fig. 5.3 are correct. This is important because Fig. 5.3 represents a time interval when the ionosphere was disturbed, which can sometimes lead to inaccurate temperature estimates.

## 5.6 Summary

The artificially induced perturbation in bulk electron temperature in the auroral E-region has been measured under both disturbed and quiet periods of plasma flow. During quiet conditions the underdense artificial increase in electron temperature was found to be of order 100 K. When the plasma flow speed increased to a level above the threshold for the Farley-Buneman instability, a natural increase in electron temperature was recorded of around 200 K. When the heater was switched on during high plasma flow conditions a net decrease was observed in the electron temperature. This represents the first experimental confirmation of the theory of Robinson (1994), which predicts a direct interaction between the heater wave and the instability which can cause quenching of the instability mechanism. Robinson (1994) calculated that during artificial heating the natural heating contribution can be reduced or eliminated, and the energy input from the heater wave is not enough to compensate, leading to an overall electron temperature decrease.

The cooling was observed when the RF wave interacted strongly with a wide range of heights in the electrojet, and when there is little or no D-region absorption. When the RF wave interacted with the instability at a narrow height range, the data suggests that although there was no cooling, there was a reduction in the heating efficiency of the RF wave.

A self-consistent computer code has been developed which calculates the electron temperature and density perturbations produced by a high power radio wave propagating through the auroral D- and E-regions. The model results are in agreement with previous studies (Tomko *et al.*, 1980; Meltz *et al.*, 1982; Milikh *et al.*, 1995) which indicate that significant electron temperature enhancement occurs in the D-region, where the power of the HF wave is high, but the electron density is low. For the first time, the model also includes the energy contribution due to Farley-Buneman heating in the electrojet, and frictional heating due to plasma flow. During quiet conditions, *i.e.* with the natural electric field switched off, the heater wave produces an electron temperature enhancement of order 100 K at electrojet heights, which is consistent with the experimental observations reported in this chapter. When the natural electric field is introduced, the Farley-Buneman heating term becomes the most significant contribution to the overall heating effect between 105 and 120 km. When the heater is turned on during model disturbed conditions, the artificial fractional temperature and density increase is less than the corresponding artificial increase under quiet conditions.

This indicates that the efficiency of the RF heating is reduced under disturbed conditions.

Using experimental values for flow speed, the model gives quantitative agreement with the EISCAT values for naturally enhanced electron temperatures on February 6 1995. This result is important for two reasons. Firstly, it verifies that the heating results contained within the model are realistic, and provide a good approximation of actual natural heating. Secondly, the result confirms the EISCAT electron temperature data for a period when the signal to noise ratio was poor, allowing greater confidence in the conclusion that an artificial electron cooling event occurred.

## Chapter 6

# *CUTLASS Spatial Observations of the Artificially Modified Ionosphere*

### 6.1 Introduction

When high power radio waves, operating in ordinary polarisation, are beamed vertically and at an angle within a few tens of degrees of the geomagnetic field, they strongly excite short perpendicular scale plasma density irregularities in regions where the wave frequency is close to the local upper-hybrid frequency (Stubbe *et al.*, 1982; Robinson, 1989 and references therein). These plasma irregularities are highly elongated in the direction of the geomagnetic field, as a consequence of the highly anisotropic nature of electron transport in the ionosphere. Small-scale field aligned irregularities (FAI) with scale sizes of a few metres to tens of metres across the geomagnetic field coherently backscatter radar signals when the radar beams are directly orthogonal to the geomagnetic field. In early ionospheric modification experiments using the high power radio transmitter at Boulder, Colorado, Thome and Blood (1974) detected strong coherent backscatter at both VHF and HF frequencies. These experiments were followed by a number of Russian investigations (e.g. Belenov *et al.*, 1977; Korovin *et al.*, 1982). More recently, Hedberg *et al.* (1983,1986) and Hanuise *et al.* (1986) have detected HF backscatter from artificial FAI in the auroral F-region, produced by the EISCAT high power facility at Tromsø, Norway (Rietveld *et al.* 1993). In addition, Hibberd *et al.* (1983) and Djuth *et al.* (1985) have detected VHF backscatter from E-region FAI generated by the Tromsø heater. Coster *et al.* (1985) utilised a 50 MHz radar to measure the growth and decay times of irregularities in both the E- and F-regions, produced by the heating facility at Arecibo, Puerto Rico.

The CUTLASS Finland radar lies approximately 1000 km to the south of Tromsø, and from this position the radar can take measurements over a horizontal cross-section in the F-region above the EISCAT heater at Tromsø. The arrangement also facilitates simultaneous observations to be made with the EISCAT incoherent scatter radars (Rishbeth and Williams, 1985).

In this chapter, results are presented from an experimental campaign in April 1996, in which the CUTLASS coherent scatter radar was employed to observe artificial field aligned irregularities (FAI) generated by the EISCAT heating facility at Tromsø, Norway.

The distribution of backscatter intensity from within the heated region has been investigated both in azimuth and range with the Finland component of CUTLASS, and the first observations of artificial irregularities by the Iceland radar are also

presented. By measuring the extent of the heated region it has been possible to investigate the threshold electric field required to excite irregularities. Differences between field-aligned and vertical propagation heating are also presented.

## 6.2 Experimental arrangement

The arrangement of diagnostics and the heater for modification experiments carried out in April 1996 is depicted schematically in Fig. 6.1. The heater operated on frequencies between 3.9000 and 4.9128 MHz. Due to technical problems, only 6 of the 12 heater transmitters were available, along with half the dipole antennas. The six transmitters operated at 90 kW each, and the gain of the array was 21 dB, compared to 24 dB when the full array is in use. This gave a heater ERP of just under 70 MW, neglecting losses. Both the Iceland and Finland components of the CUTLASS system were operational, and transmitted frequencies between 8 and 20 MHz, along up to five adjacent beam directions positioned to intercept the heated region over Tromsø. The Finland CUTLASS radar was utilised in a high resolution mode which produced a temporal resolution as fine as 1 second per beam compared to the usual 7 seconds, and a nominal range resolution of 15 km compared to the standard 45 km resolution. For the CUTLASS high resolution scan mode, the range cells are 15 km long and approximately 45 km across the beams at Tromsø. The length of a cell along a beam is determined by the length of the pulse utilised by the radar, and the width of a cell across the beams is determined by the beam width of the radar.

The EISCAT UHF radar was also operational during the campaign, and these simultaneous observations are presented in chapter 7.

## 6.3 Observations

### 6.3.1 CUTLASS observations of the horizontal extent of the heated region

The map in Fig. 6.2 illustrates the relative positions of the two CUTLASS radars in Pykkvibær, Iceland and Hankasalmi, Finland. The region overlooked by the two radars includes the EISCAT heater and incoherent scatter radar at Tromsø. The data in panel *a* is for 1200<sup>33</sup> UT on 26 April 1996. The CUTLASS Finland radar was operating at 15 MHz along beams 3-7 and the heater pointed vertically, transmitting at 4.04 MHz in O-mode polarisation. The scatter depicted in panel *a* provides evidence of artificial FAIs. This is confirmed in Panel *b*, which illustrates the absence of backscatter in the CUTLASS field of view during the following heater-

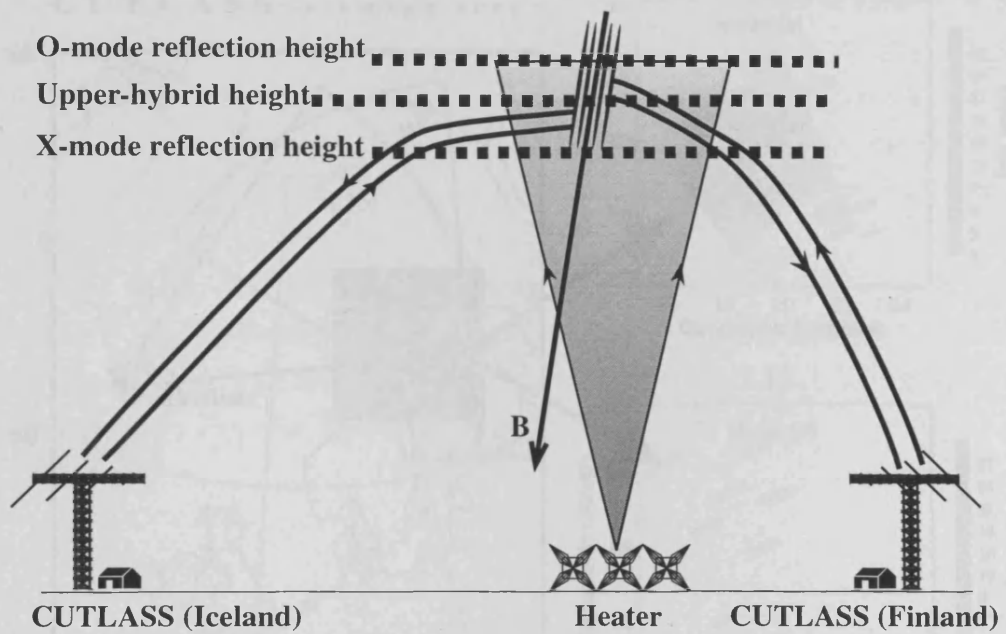


**Figure 6.1.** A schematic illustrating the relative beam geometry of the EISCAT heater and the CUTLASS radars.

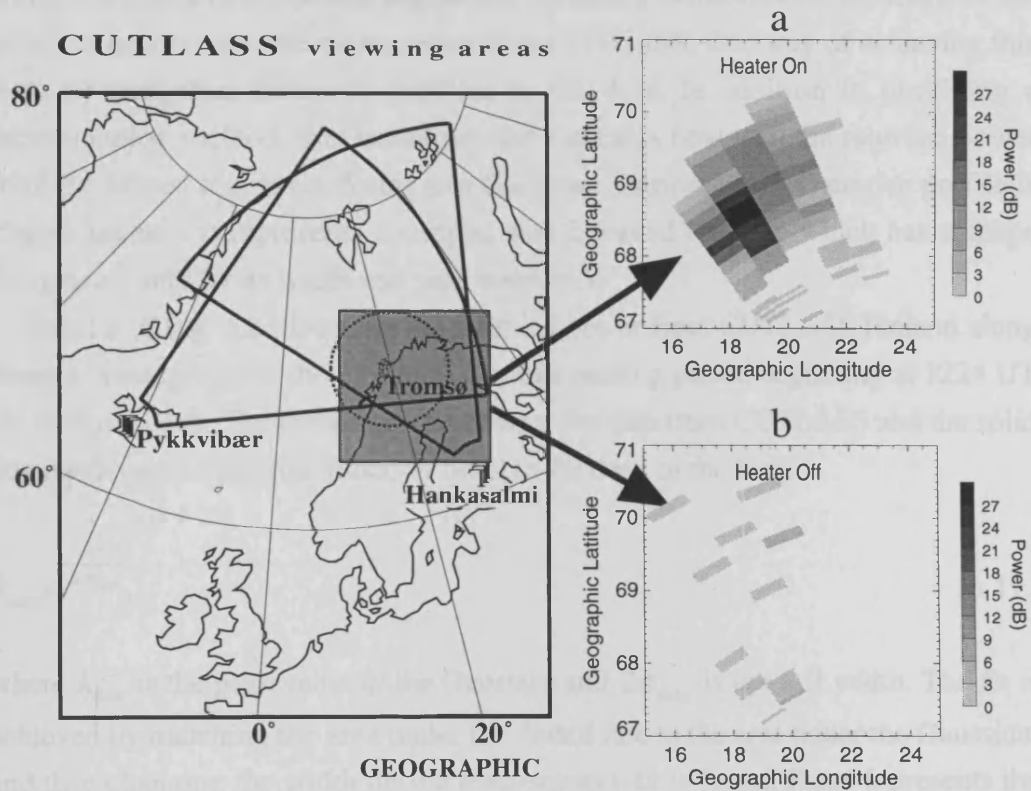


**Figure 6.2.** The map on the left depicts the locations and fields of view of the CUTLASS and EISCAT radars. The shaded region indicates the area covered by the spatial plots presented in a) and b). a) Returned power from the CUTLASS Finland radar on 26 April 1996, during a heater-on period. b) Data taken 4 minutes later during a heater off period.

off period. The data in Fig. 6.2 demonstrate that the region where FAIs were excited had a horizontal extent of around 200 km. This representation is slightly inaccurate, as the width of the radar beam and the length of the pulse are convolved with the true distribution of FAI in the heated region. In order to find the true horizontal extent of the heated region it is necessary to deconvolve the shape of the pulse (or beam) from the data produced by CUTLASS. One way of achieving this is to fit analytical Gaussian profiles to the data. In addition to providing a deconvolution method, this technique also indicates how well the returned power from the heated region conforms to a Gaussian distribution. A Gaussian profile is chosen because it represents a simple, well-behaved function which has a shape determined only by its width and peak amplitude.

Panel *a* of Fig. 6.3 illustrates the returned power from CUTLASS Finland along beam 5, averaged over the 3 minute O-mode heating period beginning at 1224 UT on 26 April 1996. The dotted line represents the data from CUTLASS and the solid line represents a Gaussian function fitted to the data, of the form

$$k_{data} e^{-\frac{x^2}{2\sigma_{data}^2}}, \quad (6.1)$$

where  $k_{data}$  is the peak value of the Gaussian and  $2\sigma_{data}$  is the full width. The fit is achieved by matching the area under the dotted line to the area under the Gaussian, and then changing the width until a least-squares-fit is found. Panel *b* presents the power output produced when a square-wave test input is fed into a CUTLASS receiver. The pulse length is converted from the temporal to the spatial domain by multiplying the width in seconds by half the free-space speed of light. The dotted line represents the data from the receiver and the solid line represents the best-fit Gaussian to the data, which has the form

$$k_{pulse} e^{-\frac{x^2}{2\sigma_{pulse}^2}}, \quad (6.2)$$

where  $k_{pulse}$  is the height of the profile and  $2\sigma_{pulse}$  is the full width. A Gaussian representing the distribution of FAI within the heated volume can be found by deconvolving the Gaussian representing the pulse from the Gaussian representing the data. This deconvolution is achieved by first finding the Fourier ( $\omega$ ) transforms of the curves in expressions 6.1 and 6.2. These transforms have the form

$$\sqrt{2\pi} k_{data} \sigma_{data} e^{-\frac{2\sigma_{data}^2 \omega^2}{4}} \quad (6.3a)$$

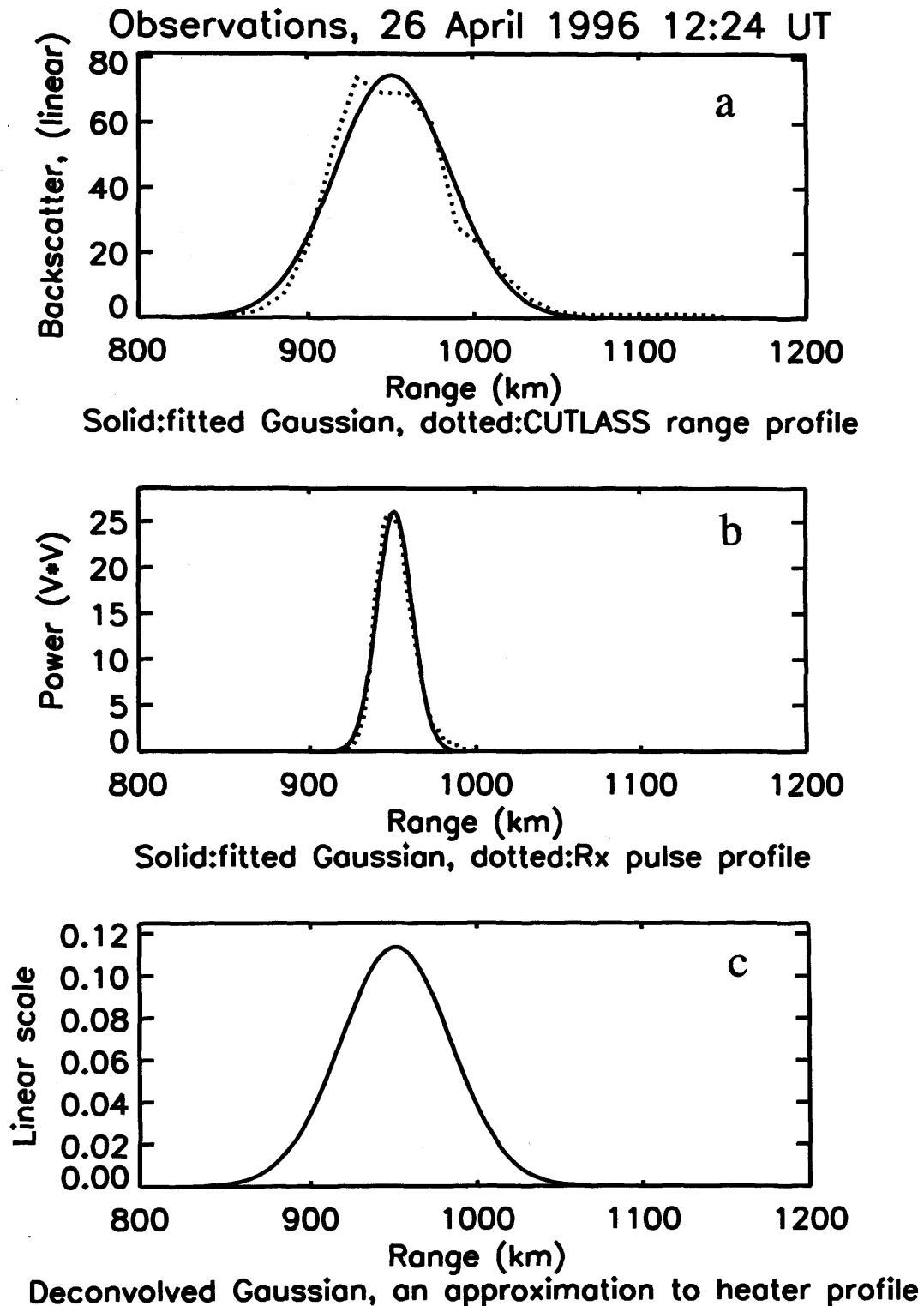


**Figure 6.3.** Observations for 1224 UT on 26 April 1996. a) The dotted line represents backscatter power from CUTLASS Finland along beam 5. The solid line is a Gaussian function fitted to the data. b) The dotted line represents the power produced by a pulse fed into a CUTLASS receiver. The solid line is a Gaussian fitted to the profile. c) An analytical profile produced by deconvolving the Gaussian fitted to the pulse profile from the curve fitted to the backscatter data.

$$\sqrt{2\pi}k_{pulse}\sigma_{pulse}e^{-\frac{2\sigma_{pulse}^2\omega^2}{4}}. \quad (6.3b)$$

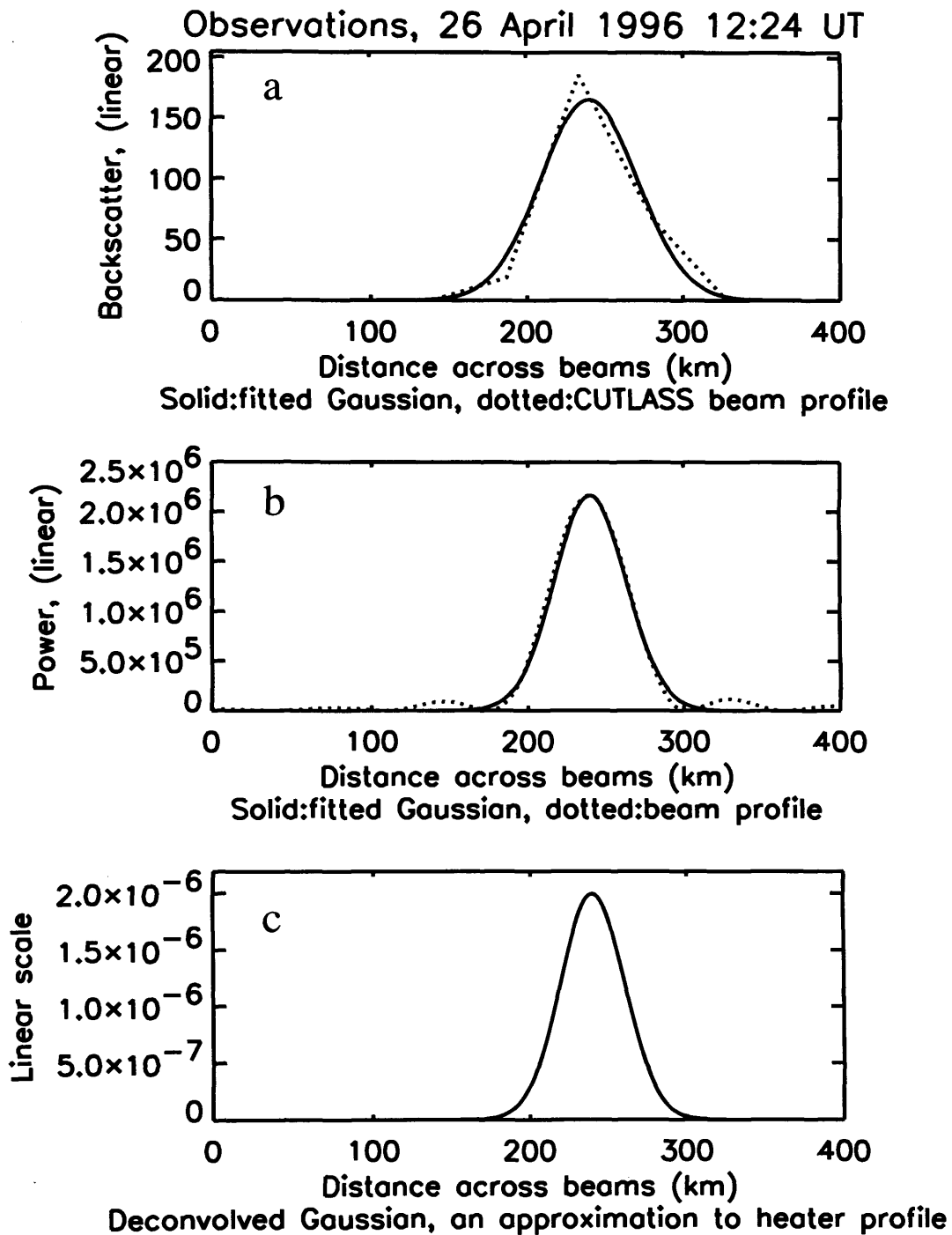
Dividing 6.3a by 6.3b gives the Fourier transform of the deconvolved Gaussian which represents the distribution of FAI. After inverse transforming the resulting deconvolved profile has the form.

$$e^{-\frac{x^2}{2(\sigma_{data}^2 - \sigma_{pulse}^2)}}. \quad (6.4)$$

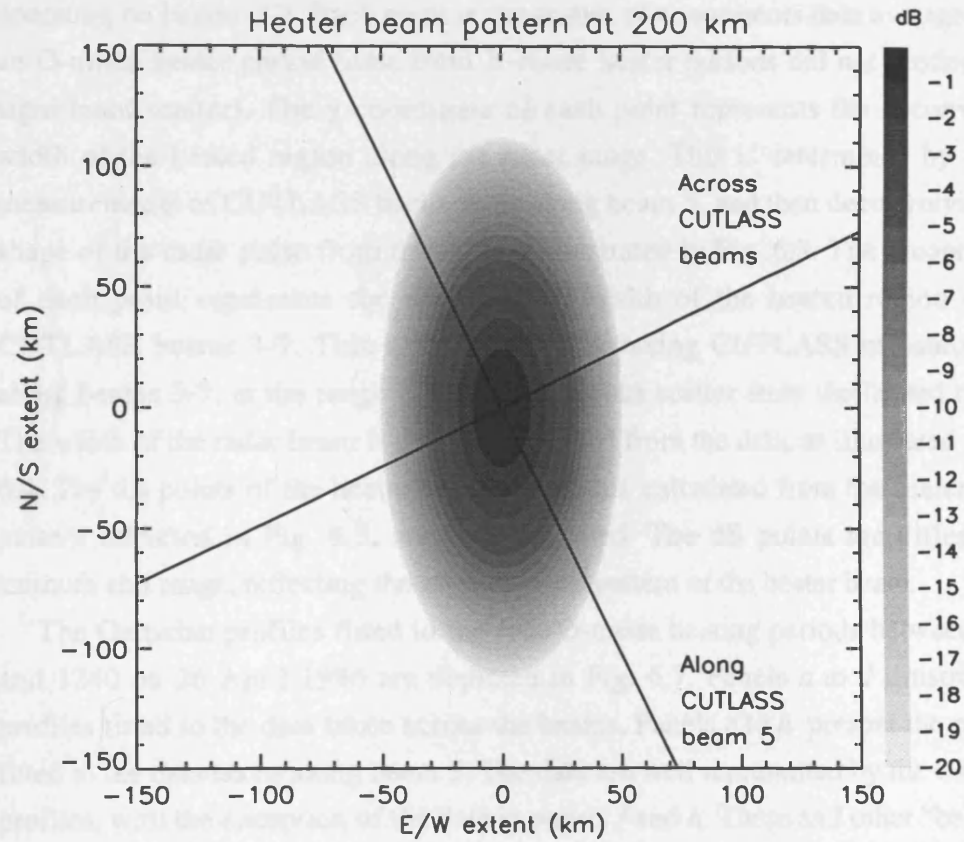
This profile is plotted in panel *c*, and the full width is  $2\sqrt{\sigma_{data}^2 - \sigma_{pulse}^2}$ .

Fig. 6.4 presents data from the same time as depicted in Fig. 6.3. The dotted line in the top panel represents the returned power from CUTLASS Finland across five beam directions, at a range corresponding to the position of the heater. The solid line is a best-fit Gaussian to the data, of the form illustrated in expression 6.1. The dotted line in panel *b* depicts a modelled profile for beam 5 of the CUTLASS radar (the profiles for the other beams utilised in this experiment are very similar). The solid line represents a best-fit Gaussian to the data, with the same form as expression 2. The bottom panel of Fig. 6.4 illustrates the result of analytically deconvolving the Gaussian fitted to the beam shape from the Gaussian fitted to the CUTLASS data. The profile is a representation of the extent of the heated region across the beams; and has the same form as expression 6.4.

In order to interpret spatial observations of the heated volume it is necessary to model the beam pattern of the heater. During the April 1996 campaign, only 6 of the 12 transmitters were available at the heater site, along with half the dipole antennas of array 2. Whilst the full number of antennas were available in the east-west direction, only half the usual number in the north-south direction were present. Therefore, the beam pattern was modelled to take account of the north-south, east-west asymmetry. The heater beam pattern was calculated from the theoretical beam pattern of the heater antenna array. In addition, ray tracing calculations were carried out utilising a realistic electron density profile which indicated that spreading of the heater rays near the reflection point was less than 5 km. Fig. 6.5 presents the contours at a height of 200 km for O-mode propagation at 4.04 MHz. The contours are expressed in dB below the power at the centre of the beam. Each contour is an ellipse, with the major axis determined by the beam pattern in the north-south direction, and the minor axis by the beam pattern in the east-west direction. The direction of CUTLASS beam 5 is marked in Fig. 6.5, along with the direction across the CUTLASS beams. By calculating where these two lines cross the



**Figure 6.4.** Observations for 1224 UT on 26 April 1996. a) The dotted line represents backscatter power from CUTLASS Finland across beams 3-7 at a range gate over Tromsø. The solid line is a Gaussian function fitted to the data. b) The dotted line represents a modelled beam profile for the CUTLASS antenna system. The solid line is a Gaussian fitted to the beam profile. c) An analytical profile produced by deconvolving the Gaussian fitted to the beam profile from the curve fitted to the backscatter data.



**Figure 6.5.** A contour plot illustrating the power distribution of the heater beam at an altitude of 200 km. The shading presents the power in dB below the power at the centre of the beam. The straight lines indicate the directions along and normal to CUTLASS Finland beam 5.

contours it is possible to build up a picture of the amount of heater power radiated into different positions in the CUTLASS field of view.

Observations covering the whole campaign are depicted in Fig. 6.6. The data is from CUTLASS Finland, for times when the radar was operating in a scan mode operating on beams 3-7. Each point in the scatter plot represents data averaged over an O-mode heater period (data from X-mode heater periods did not produce any significant scatter). The y-coordinate of each point represents the deconvolved width of the heated region along the radar range. This is determined by taking measurements of CUTLASS backscatter along beam 5, and then deconvolving the shape of the radar pulse from the data, as illustrated in Fig. 6.3. The x-coordinate of each point represents the deconvolved width of the heated region across CUTLASS beams 3-7. This is determined by taking CUTLASS measurements along beams 3-7, at the range of the most intense scatter from the heated region. The width of the radar beam is then deconvolved from the data, as illustrated in Fig. 6.4. The dB points of the heater beam at 200 km, calculated from the heater beam pattern depicted in Fig. 6.5, are also indicated. The dB points are different in azimuth and range, reflecting the asymmetrical pattern of the heater beam.

The Gaussian profiles fitted to the four O-mode heating periods between 1200 and 1240 on 26 April 1996 are depicted in Fig. 6.7. Panels *a* to *d* illustrate the profiles fitted to the data taken across the beams, Panels *e* to *h* present the profiles fitted to the data taken along beam 5. The data are well represented by the Gaussian profiles, with the exception of the data in panels *f* and *h*. These and other “bad fits”, defined by a chi-squared fit less than 1, are excluded from the data plotted in Fig. 6.6.

An ionogram taken at the heater site at 1210 UT on 26 April 1996 is presented in Fig. 6.8. The dots represent the ionogram and the solid line indicates a calculated true-height electron density profile (Titheridge, 1985). Fig. 6.8 is typical of ionograms taken during the campaign.

### 6.3.2 Estimating the size of the heated region

The width of the deconvolved Gaussian provides a useful first estimate of the size of the heated region. This width represents approximately the -2 dB contour of FAI amplitudes. However, it is also of interest to determine the limiting size of the region in which backscatter is generated above the background noise. This allows us to estimate the required heater threshold electric field for the excitation process. This may be achieved by exploiting the fitted Gaussian, as follows.

The returned backscatter power to the CUTLASS radar can be represented by

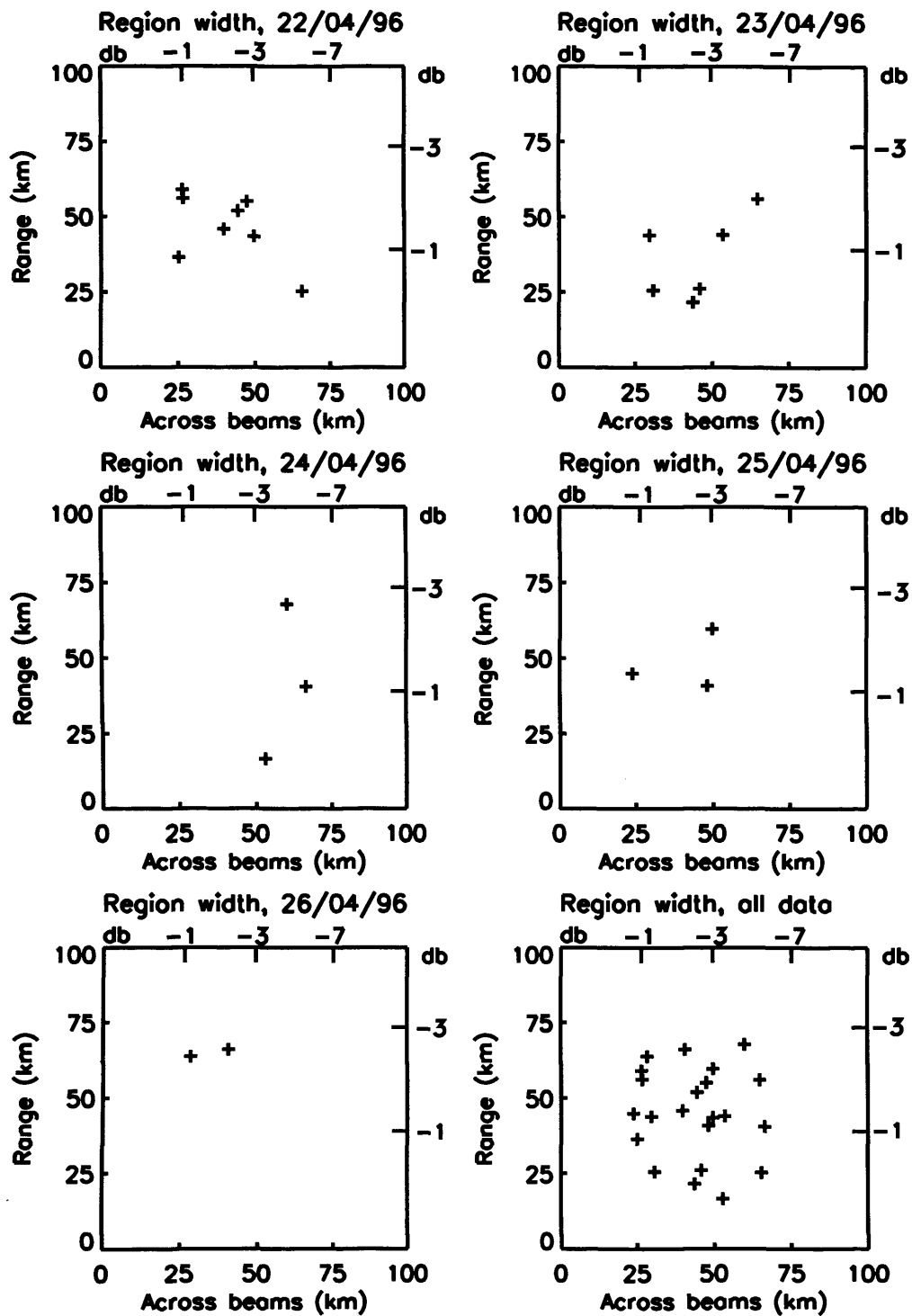


**Figure 6.6.** Observations for 22-26 April 1996. Each scatter plot represents the width of the heated region along CUTLASS beam 5 against the width across CUTLASS beams 3-7. The dB scale indicates the level of power in dB down from the centre of the heater beam.

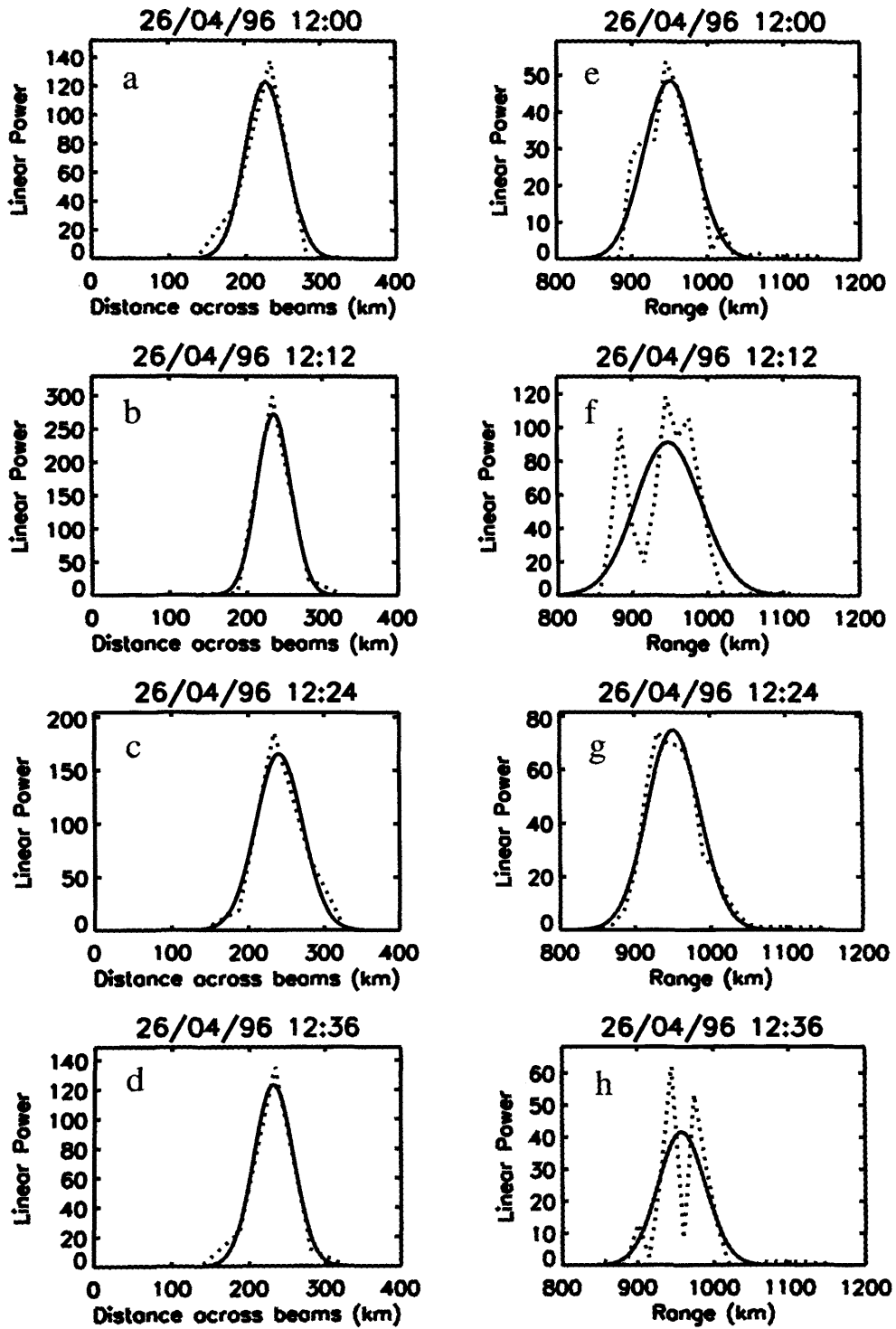
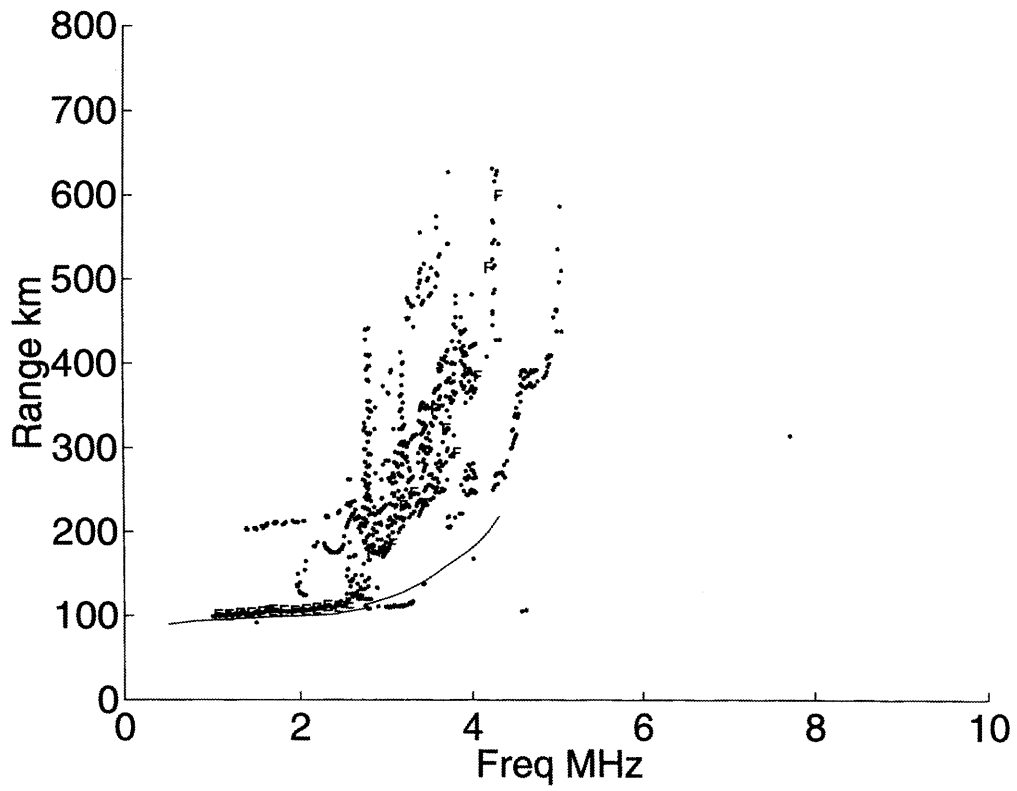


Figure 6.7. Data from CUTLASS Finland for 26 April 1996, between 12:00 and 12:40 UT. Panels a) to d) illustrate Gaussian profiles fitted to azimuthal data. Panels e) to h) present Gaussian profiles fitted to range data.



**Figure 6.8.** An ionogram taken at 1210 UT on 26 April 1996. The critical frequency was 4.3 MHz. The solid line represents a fitted true-height electron density profile.

$$P_{dB} = 10 \log \left( \frac{S}{N} \right) \quad (6.5)$$

Where  $P_{dB}$  is the returned backscatter power in dB, and  $S$  and  $N$  are the signal and noise power respectively, measured in linear units. From expression 4, the signal-to-noise ratio after deconvolution can be represented by a Gaussian of the form

$$\frac{S}{N} = k_{decon} e^{\frac{-x^2}{2\sigma_{decon}^2}} \quad (6.6)$$

where  $\sigma_{decon}$  is the width of the Gaussian (equal to  $\sqrt{\sigma_{data}^2 - \sigma_{pulse}^2}$  as given in expression 4) and  $k_{decon}$  is the peak height of the Gaussian. A value for  $k_{decon}$  can be determined from the peak backscatter power from the centre of the heated region,  $P_{peak}$ . Substituting for  $P_{peak}$ , equation 6.6 becomes

$$\frac{S}{N} = 10^{\frac{P_{peak}}{10}} e^{\frac{-x^2}{2\sigma_{decon}^2}} \quad (6.7)$$

When the signal-to-noise ratio becomes unity, equation 6.7 can be re-written thus

$$\frac{-P_{peak}}{10} \ln 10 = \frac{-x^2}{2\sigma_{decon}^2} \quad (6.8)$$

And the distance from the centre of the Gaussian where the signal reaches the noise level is

$$x = \sqrt{\frac{\ln 10}{5} \sigma_{decon}^2 P_{peak}} \quad (6.9)$$

From equation 6.9 we define the noise threshold range as the full range across the heated region where the deconvolved signal is above the noise level. This is equal to twice the value in equation 6.9.

$$\text{noise threshold range} = 1.36 \sigma_{decon} \sqrt{P_{peak}} \quad (6.10)$$

where the noise threshold range and  $\sigma_{decon}$  are in km and  $P_{peak}$  is in dB.

Fig. 6.9 presents observations of the noise threshold range as a function of UT for 22-26 April 1996. Each point represents backscatter measurements along CUTLASS beam 5, averaged over a 3 minute O-mode heating period (X-mode

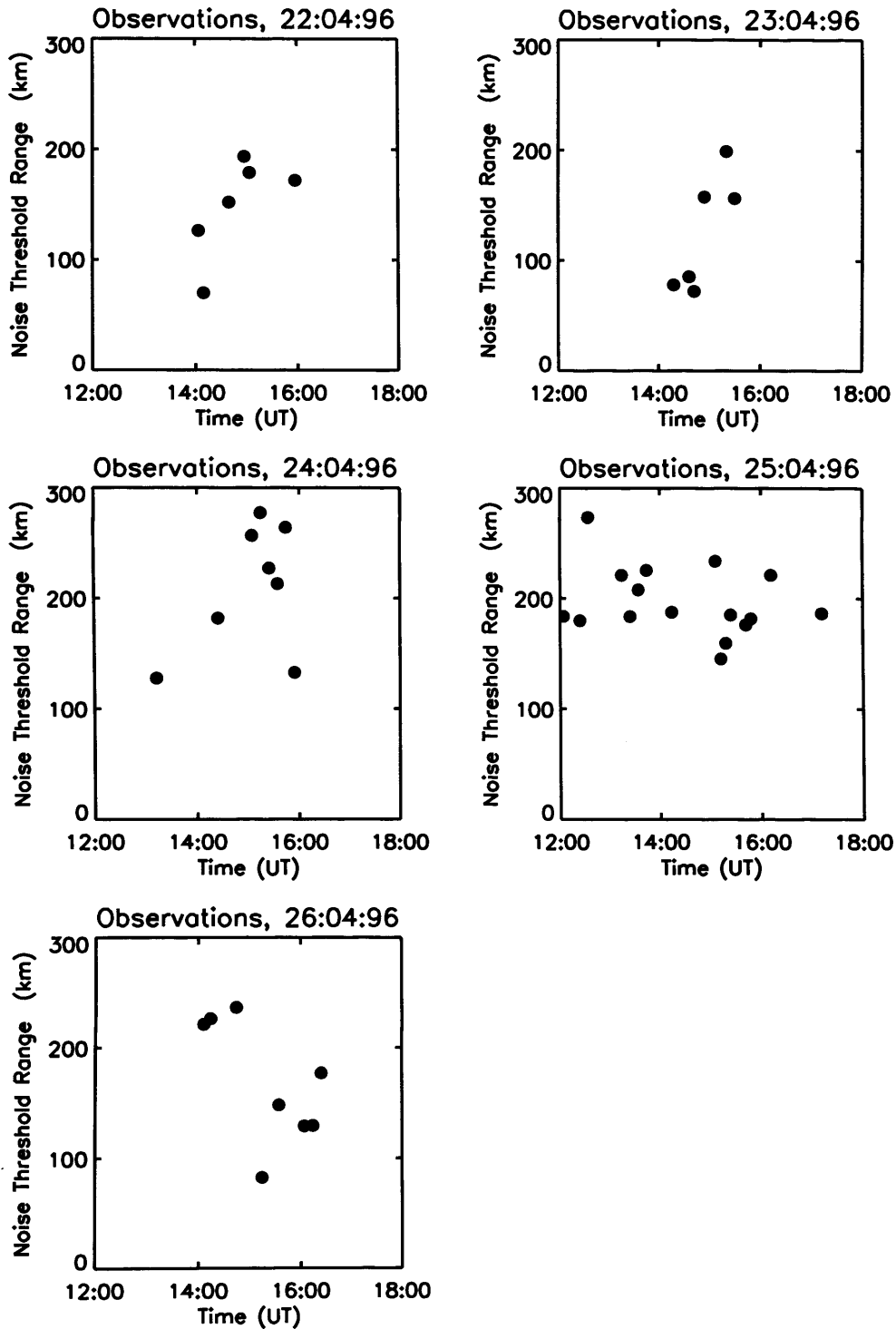


**Figure 6.9.** Observations for 22-26 April 1996. The noise threshold range, a measure of where artificial scatter is observed above the noise level, plotted as a function of UT.

periods did not produce significant scatter). Points are only plotted for an average peak returned power of greater than 20 dB, and for a Gaussian profile fitting the data with a chi-squared fit less than 0.5. For the data in Fig. 6.9, the mean noise threshold range across the full width of the heated region is  $170 \text{ km} \pm 50 \text{ km}$ .

### 6.3.3 CUTLASS observations during vertical and field aligned heater beam propagation

By phasing the antennas in the heater array, it is possible to steer the heater beam to different positions. Fig. 6.10 depicts three CUTLASS spatial plots of the heated region at 1447<sup>02</sup>, 1504<sup>38</sup> and 1533<sup>40</sup> UT on 22 April 1996. During these 3 periods the heater was transmitting at 4.10 MHz in O-mode polarisation. CUTLASS was in a 5 beam scan mode, dwelling on each beam for five seconds and transmitting at 12.4 MHz. Panels *a* and *c* of Fig. 6.10 represent data from when the heater beam pointed south, at  $13^\circ$  to the vertical, panel *b* represents data taken during vertical propagation. Horizontal lines are drawn at  $67.9^\circ$  and  $70.3^\circ$  latitude, to clearly indicate the movement of the heated region. The scatter corresponding to vertical propagation is  $0.3^\circ$  north of the regions of scatter corresponding to propagation at  $13^\circ$  to the vertical. No significant change is observed in the east-west position of the heated region.

### 6.3.4 Results from the Iceland radar

Panel *a* in Fig. 6.11 depicts a spatial plot from the Iceland radar for 1324<sup>45</sup> UT on the 24 April 1996. The Iceland radar was operating at a frequency of 15 MHz and was in a 45 km range mode. Panel *b* in Fig. 6.11 presents the spatial plot from the Finland radar for 1324<sup>48</sup> UT. The Finland radar was operating at 12.4 MHz in a 15 km range mode. The heater was transmitting at 4.20 MHz in O-mode polarisation.

## 6.4 Discussion and conclusions

### 6.4.1 CUTLASS spatial measurements

The CUTLASS beam is approximately horizontal when it intersects the heated region, and so the data from CUTLASS represents a horizontal slice through the heated volume. The height at which CUTLASS intersects the heated volume encompasses the region of most intense scatter near the reflection point of the heater. The width of Gaussian functions fitted to the data indicate the variation in irregularity intensity with distance from the centre of the heated region, and allow

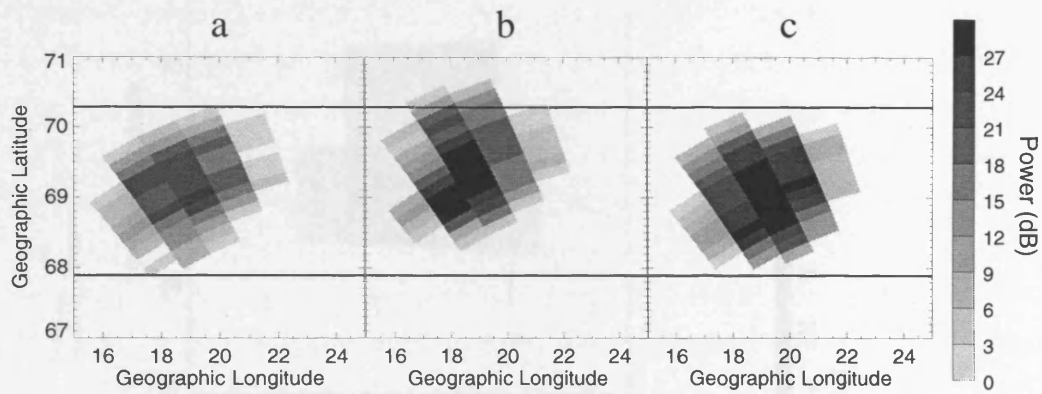


**Figure 6.10.** CUTLASS Finland spatial plots for 22 April 1996. a) 1447 UT, heater beam at  $-13^\circ$  to the vertical. b) 1504 UT, heater beam pointing vertically. c) 1534 UT, heater beam at  $-13^\circ$  to the vertical. Horizontal lines are drawn at  $67.9^\circ$  and  $70.3^\circ$  latitude.

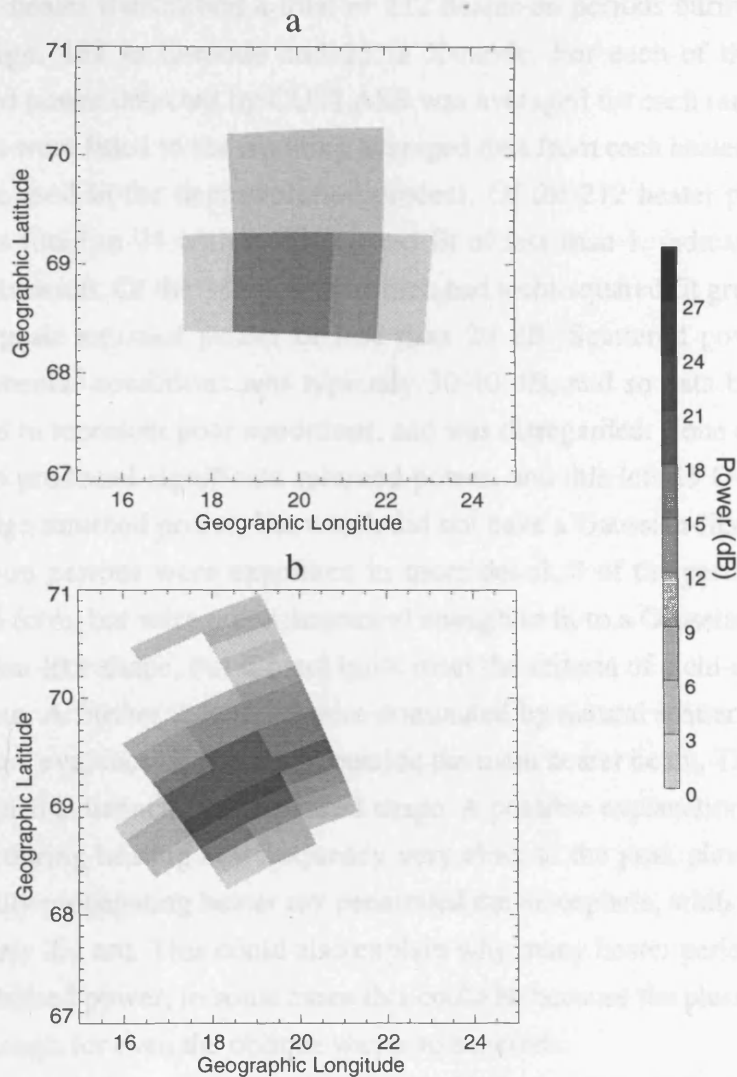


**Figure 6.11.** CUTLASS spatial plots of returned power taken at 1324 UT on 24 April 1996, during a heater-on period. a) Iceland radar operating at 15 MHz in 45 km range mode. b) Finland radar operating at 12.4 MHz in 15 km range mode.

comparison between measurements taken in range and azimuth. By determining where the Gaussian functions are above the noise level it is possible to make an estimate of the threshold electric fields required for the production of FAIs.

The heater transmitted a total of 212 heater-on periods during the April 1996 campaign, 187 in O-mode and 25 in X-mode. For each of these periods, the returned power detected by CUTLASS was averaged for each range bin. Gaussian profiles were fitted to the resulting averaged data from each heater-on, which could then be used in the deconvolution process. Of the 212 heater periods, Gaussian profiles fitted to 94 with a chi-squared fit of less than 1, indicating a reasonable approximation. Of the 118 periods which had a chi-squared fit greater than one, 93 had a peak returned power of less than 20 dB. Scattered power during good experimental conditions was typically 30-40 dB, and so data below 20 dB was deemed to represent poor conditions, and was disregarded. None of the 25 X-mode periods produced significant returned power, and this left 25 O-mode heater-ons with high returned power, but which did not have a Gaussian-like shape. These 25 heater-on periods were examined in more detail. 8 of the periods had a single-peaked form, but were not symmetrical enough to fit to a Gaussian. 3 periods had a Gaussian-like shape, but did not quite meet the criteria of a chi-squared fit of less than one. A further 2 profiles were dominated by natural scatter, and two periods indicated evidence of excitation outside the main heater beam. This left 10 periods which had a distinct double peaked shape. A possible explanation for this structure is that during heating at a frequency very close to the peak plasma frequency the vertically propagating heater ray penetrated the ionosphere, whilst rays propagating obliquely did not. This could also explain why many heater periods produced very low returned power, in some cases this could be because the plasma frequency was low enough for even the oblique waves to penetrate.

Fig. 6.6 depicts data from the April 1996 campaign, during heater-on periods when CUTLASS was operating in a scan mode. The summary scatter plot for the whole campaign indicates that the deconvolved width of the heater beam corresponds approximately to the 2 dB point determined from the model. The width of the heater beam is usually described in terms of its half power point, or 3 dB down point, and so the Gaussian width of the heated region lies within the width of the heater beam.

The data in Fig. 6.7 represent range and azimuth profiles for 4 O-mode periods transmitted on 26 April 1996. The azimuthal data appears to be better represented by Gaussian profiles than the range data, as in nearly all cases the azimuthal data exhibited a single peaked, symmetrical shape. However, as only five beams were used in each scan, the number of degrees of freedom in azimuth is low, and the resulting chi-squared fit is poor. The limitations of the azimuthal data are borne out

in Fig. 6.7. The azimuthal data is pictured in panels *a-d* and the range data is in panels *e-h*. The range data depicts far more structure in the heated region. The data in panel *g* is well represented by a Gaussian, and the data in panel *e* is also a reasonable fit. Panels *f* and *h* provide evidence of a double peaked structure. In contrast, the azimuthal data is all single peaked, with no additional structure. This indicates that the finer resolution associated with the range data is crucial in revealing the true structure of the heated region. Although deconvolution of the azimuthal data gives an estimate of the spreading effect of the radar beam width, it cannot reveal any further detail when so few data points are available.

The threshold electric field required to produce irregularities can be estimated by utilising the mean noise threshold range determined from the data in Fig. 6.9, which has a value of  $170 \pm 50$  km. The height where irregularities were excited was found to be around 200 km by observing the height of the ion-overshoot. The ion-overshoot is a spike in the power profile of the EISCAT data caused by the excitation of ion acoustic waves during the first few seconds of heating (*e.g.* Robinson, 1989). By using the beam pattern model presented in Fig. 6.5, the extent of 170 km was found to correspond to a heater power of  $20 \pm 12$  dB below the power at the centre of the beam. The large error estimate is due to the fast fall-off in heater power at this distance from the centre of the beam. During the experiments, 6 heater transmitters at a power of 90 kW each were utilised and the gain produced by the available antennas was 21 dB, producing an ERP of 68 MW. Assuming free space propagation, the electric field,  $E$  (V/m), produced by a heater beam with  $ERP$  in kW, at an altitude,  $R$  (km), is (Robinson, 1989)

$$E = \frac{0.25\sqrt{ERP}}{R}. \quad (6.11)$$

This gives an electric field of 0.3 V/m at the centre of the heater beam at 200 km altitude. Allowing for the 20 dB reduction in power, the electric field at the edge of the region of artificial backscatter was between 0.01 and 0.1 V/m. These two values correspond to the upper and lower limits of the error estimate in the mean noise threshold range.

Hysteresis effects can significantly affect the threshold level of the irregularities. The heater operated in a typical cycle of 3 minutes O-mode on, followed by 3-minutes off. The irregularities were sometimes observed to remain in the ionosphere for as long as 3 minutes after heater off, but only at the centre of the heater beam and not at the edges where threshold effect were calculated. However, to be certain that hysteresis effect are not plying a role it is useful to examine the noise threshold range calculated for April 25 1996 (Fig. 6.9). Between 1200 and

1500 UT the heater operated in a cycle of 2 minute tune (low power on) 2 minute off, 3 minute O-mode, 3 minute off. Between 1500 and 1700 UT the heater operated with a cycle of 3 minutes O-mode, 3 minutes off, 3 minutes X-mode, 3 minutes off. As X-mode heating does not produce irregularities, this means that between 1500 and 1700 UT the ionosphere was left for 9 minutes before new irregularities were generated, compared to 2 minutes between 1200 and 1500 UT. The plot in Fig. 9. indicates that the noise threshold range remained at around 200 km for both heater regimes, indicating that hysteresis effects were not influencing the measurements.

The thermal parametric instability (TPI) is thought to be involved in the production of FAIs, and this has a threshold electric field,  $E_t$ , given by (Das and Fejer, 1979)

$$pE_t^2 = \frac{15.38(T_{eo}k_B)^2 \omega_0^2 \sin I}{\nu \Omega_e e^2 H \lambda} e^{\frac{\nu H}{50 \omega_0}}. \quad (6.12)$$

$p \leq 1$  depends on the standing wave ratio of the heater wave and is 1 for the case when the pump electric field is maximised,  $k_B$  is Boltzmann's constant,  $I$  is the angle of inclination of the geomagnetic field,  $H$  is the scale height,  $\omega_0$  is the angular frequency of the heater wave,  $T_{eo}$  is the undisturbed electron temperature,  $\nu$  is the electron-neutral collision frequency,  $e$  is the electronic charge,  $\lambda$  is the wavelength of the FAIs and  $\Omega_e$  is the electron gyro frequency. For typical ionospheric parameters Das and Fejer (1979) determine the following expression for  $E_t$ ,

$$E_t = \sqrt{\frac{0.264}{\lambda p}} \quad (6.13)$$

For irregularities of scale length 10m, which is the case for a radar frequency of 15 MHz, and taking the most favourable case of  $p = 1$ , the threshold electric field is 0.16 V/m. This threshold is high compared to the threshold value derived from the data of between 0.01 and 0.1 V/m, although other investigations have found a lower threshold value. Lee and Kuo (1983) consider a TPI characterised by a four-wave interaction. These authors found a threshold electric field of 0.0015 V/m for irregularities scale lengths of greater than 10m, which is below the threshold electric field measured for the current study.

These results indicate that it is possible to excite instabilities in a region significantly wider than the nominal width of the heater beam. Djuth *et al.* (1985) utilised a 49 MHz coherent scatter radar to measure the response of the ionosphere

to a heater wave reflecting in the E-region. These authors also observed scatter from FAIs outside the 3 dB point. Stubbe *et al.* (1982) found that under quiet ionospheric conditions, the level of anomalous absorption produced was independent of heater power. These authors observed 15 dB of anomalous absorption for a heater ERP of 160 MW. This did not change when the ERP was reduced by 10 dB, which further illustrates that irregularities can be excited at relatively low heater powers.

Ray-tracing calculations (Jones and Stephenson, 1975) utilising the appropriate heater frequency and the ionogram in Fig. 6.8 suggest that rays spread out to a diameter 5 km greater than the nominal half-power point at the upper hybrid height. Other factors which could produce irregularities outside the 3 dB point are refraction due natural horizontal gradients in the ionosphere and FAIs spreading outside the heated region along the field lines .

#### **6.4.2 Comparisons of vertical and field-aligned heater beam positions**

The heater antennas can be phased to provide electronic steering of the heater beam. In Fig. 6.10 the scatter in panel *c*, taken when the heater was pointing vertically, is approximately  $0.3^\circ$  latitude further north than the scatter in panels *b* and *c*, where the heater was pointing south, at  $13^\circ$  to the vertical. This corresponds to a horizontal distance of  $40 \pm 10$  km. This is consistent with the theoretical value of 45 km, obtained from the geometric movement produced at 200 km altitude when the beam is moved by  $13^\circ$ .

#### **6.4.3 Iceland observations of the heated region**

The first observations of the heated region by the CUTLASS Iceland radar were made during the April 1996 campaign. Fig. 6.11 presents 2 spatial plots of the heated patch, panel *a* is produced from Iceland data, and panel *b* presents data from the Finland radar. The different views of the heated region presented by the two plots are due to the position of the two radars in relation to the heater. The heater site at Tromsø is 1000 km away from the Finland radar and lies near the centre of the radar field of view. The Iceland radar is around 2000 km away from the Tromsø site and the heated region is only detected in the last two or three beams of the radar's scan (see Fig. 6.2). Also, in this case, the Finland radar was operating in a 15 km range mode, compared to the 45 km mode employed in Iceland. The low signal-to noise ratio observed at Iceland could be due to the greater range involved, and may also be due to greater refraction causing the radar beam to look into the E-

region rather than the F-region over Tromsø. The Finland radar received backscatter from artificial irregularities consistently throughout the campaign. The results from Iceland were more sporadic, scatter was not detected during long periods of heating, but was sometimes observed consistently for periods of up to two hours.

The two spatial plots in Fig. 6.11 provide a consistent picture of the position of the heated region over the Tromsø site, at around 69 latitude and 19 longitude.

## 6.5 Summary

Measurements of the spatial extent of the heated region over Tromsø have been presented. The CUTLASS radar was employed to produce spatial maps of backscatter intensity across a horizontal cross-section of the heated region. A deconvolution method, using fitted Gaussians, was utilised to remove the effects of the radar beam width and the pulse length from the measurements. The full Gaussian width of scatter from the heated patch was found to lie within the half-power-width of the heater beam. The profile of returned power along the radar beam was found to have a Gaussian-like shape in the majority of cases. In the examples where this was not the case, a double peak structure was sometimes seen. This structure could be due to vertically propagating heater rays penetrating the ionosphere, leaving only oblique rays to produce FAI. Measurements in azimuth produced Gaussian-like profiles in most cases, with no evidence of double peaked structure. This is probably due to the azimuthal data having poorer resolution than the range data, making this data suitable for estimating the overall width of the heated region, but not for identifying finer structure.

The horizontal range over which artificial instabilities were excited was measured to be around 170 km. This demonstrates that it is possible to produce FAIs far beyond the half-power-point of the heater beam. By comparing the observations to a model of the heater radiated power, it was found that FAIs were generated at 20 dB down from the power at the centre of the heater beam. This corresponds to an electric field of between 0.01 and 0.1 V/m at an altitude of 200 km, which is an indication of the threshold electric field required to excite FAIs. The measured threshold value is in approximate agreement with the theoretical value required to excite the thermal parametric instability.

The effect of moving the heater beam has been investigated. It was found that when the heater beam was moved by  $13^\circ$  from the vertical, the region of artificial backscatter observed by CUTLASS moved  $0.3^\circ$  latitude south. By assuming that the scatter was from near the reflection point of the heater, it was calculated that the heated region had moved around 50 km, which was consistent with a beam movement of  $13^\circ$ .

Spatial plots from the Finland and Iceland CUTLASS radars have been compared. The Finland radar produces more intense and more consistent scatter than Iceland, which is further away from the heater site and may not always look in the F-region. The two radars provide a consistent picture of the position of the heated region over Tromsø.

## Chapter 7

# *Decay Characteristics of Heater Induced Irregularities*

### 7.1 Introduction

Artificial FAI with scale sizes of a few metres to tens of metres across the geomagnetic field coherently backscatter radar signals when the radar beams are directly orthogonal to the geomagnetic field. These irregularities remain in the ionosphere for some time after the high power radio beam has been turned off, and gradually decay over periods as long as a few minutes. The nature of the decay is indicative of the properties of both the irregularities themselves and the background ionospheric conditions.

In this chapter, results are presented from an experimental campaign in April 1996, in which the CUTLASS coherent scatter radar was employed to observe artificial field aligned irregularities (FAI) generated by the EISCAT heating facility at Tromsø, Norway. The EISCAT UHF radar was utilised as a complementary diagnostic to measure background ionospheric parameters.

Many characteristics of FAI are revealed by the way the structures decay after the heater has been turned off. A diffusion mechanism is believed to be involved, where the decay rate is proportional to the scale length of the structures perpendicular to the field line (Belenov *et al.*, 1977; Coster *et al.*, 1985; Hysell *et al.*, 1996). This scale-dependent diffusion is widely recognised as a key process in the plasma. Coherent scatter isolates structures with k-vectors which are double that of the radar wavelength, and so structures with different scale sizes can be observed by transmitting different radar frequencies.

The decay time of the irregularities has been investigated, and a two stage exponential decay process has been identified. The first decay constant has a value of order 10 s and is dependent on the scale size of the irregularities isolated by the coherent scatter. The second decay constant is of order 100 s and is thought to depend on artificial large-scale structure. The backscatter from the irregularities falls below the 3 dB level approximately 100 s after heater switch off, and this decay varies with time of day.

### 7.2 Experimental arrangement

The arrangement of diagnostics and the heater for modification experiments carried out in April 1996 is depicted schematically in Fig. 7.1. Due to technical problems,

only 6 of the 12 heater transmitters were available, along with half the dipole antennas. The six transmitters operated at 90 kW each, and the gain of the array was 21 dB, compared to 24 dB when the full array is in use. This gave a heater ERP of just under 70 MW, neglecting losses, and the frequencies utilised were between 3.9000 and 4.9128 MHz. The Finland CUTLASS radar operated in 2 main frequency modes, 12.4 and 15 MHz. A high resolution mode was employed, which produced a temporal resolution as fine as 1 second per beam compared to the usual 7 seconds, and a range resolution of 15 km compared to the standard 45 km resolution. The EISCAT UHF radar (Rishbeth and Williams, 1985) utilised a CP1 pulse scheme, modified during some of the experiments to point vertically rather than along the geomagnetic field line. This scheme points the 3 UHF radars in Norway, Finland and Sweden in fixed directions and produces both alternating code and long-pulse data. The tristatic arrangement facilitates the calculation of the flow velocity of the ionospheric plasma.

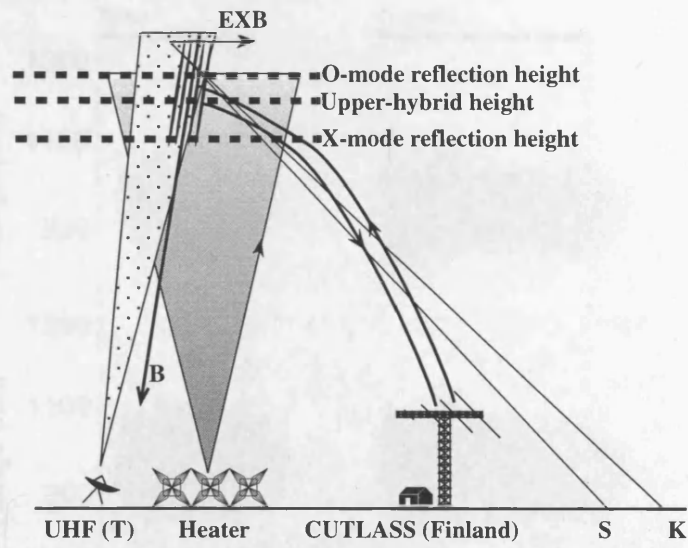
The backscatter power observed by CUTLASS is proportional to the square of the density perturbation induced by the heater, and so CUTLASS was utilised to measure the decay of the irregularity amplitude after heater-off. The EISCAT UHF radar was employed simultaneously to provide measurements of background ionospheric parameters, as the nature of the decay is dependent flow speed, electron density and ion and electron temperatures.

### **7.3 Observations**

#### **7.3.1 CUTLASS observations**

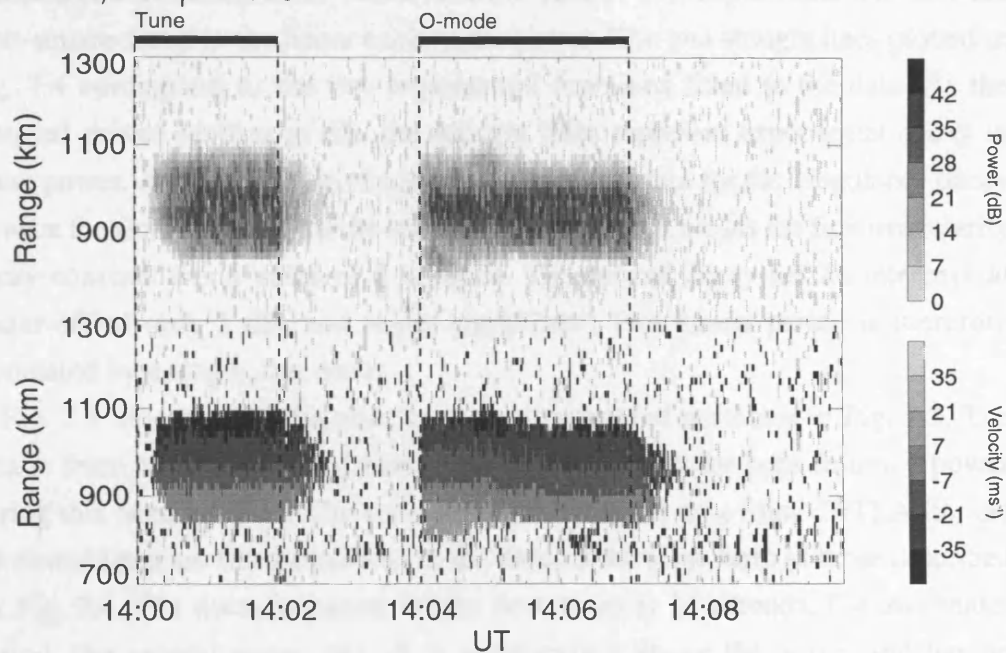
Fig. 7.2 presents data from 25 April 1996. The top panel illustrates returned power from the CUTLASS Finland radar, and the bottom panel indicates line of sight velocity, with negative velocity being away from the radar. CUTLASS operated in a 1 second temporal resolution mode, along a single beam (beam 5) positioned over the heater site at Tromsø, Northern Norway. The backscatter between 1400 and 1403 UT is due to a heater tuning period, and will not be considered in detail. At 1404 UT the heater was switched on at full power, and backscatter was excited to a signal-to-noise ratio of around 30 dB within a few seconds. The heater was turned off at 1407 and the irregularities decayed to a level below the noise in under one minute.

Fig. 7.3 depicts backscatter detected during a heater period later in the day on 25 April 1996. The heater was turned on at full power at 1712 UT and irregularities were excited to greater than 30 dB within a few seconds. The heater was turned off



**Figure 7.1.** Schematic illustrating the beam geometry for the experiment.

Finland, 25 April 1996



**Figure 7.2.** The top panel presents backscatter power measured by CUTLASS Finland along beam 5 from 1400 to 1410 on 25 April 1996. The bottom panel depicts the line of sight velocity measured by CUTLASS.

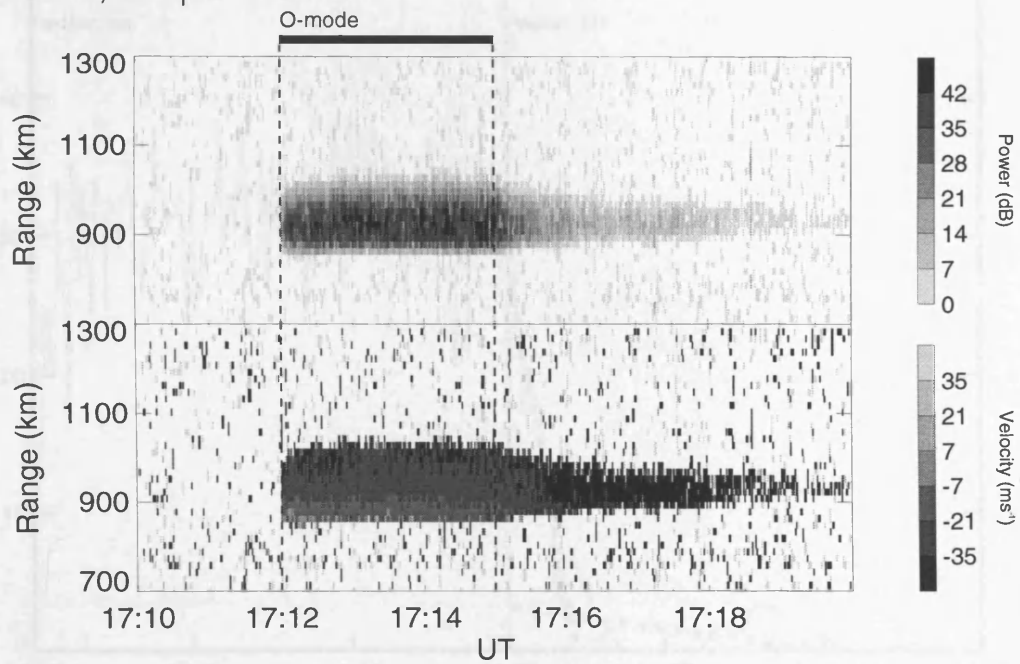
at 1715 and some evidence of artificial scatter was still present at 1719, 4 minutes after the heater was turned off.

Fig. 7.4 illustrates a line plot of backscatter from the time period presented in Fig. 7.2. The backscatter is from beam 5, range gate 32, which represented the region of most intense artificial scatter for this particular period. The solid line represents the data from CUTLASS and the dotted lines are fitted functions to the data. After heater-on, the artificial scatter was excited to a level of around 32 dB within a few seconds. After heater-off, the sum of two exponential curves were least-square-fitted to the linear backscatter power. The two straight lines plotted in Fig. 7.4 correspond to the two exponential functions fitted to the data. As the returned power scale is in dB, the straight lines represent exponential decay in linear power. As described in chapter 3, the time constant for the irregularity decay is twice the time constant for the returned power, which means the first irregularity decay constant has a value of 8 seconds. The second decay has an intercept at heater-off of only 3 dB, and is not significant. This heater period is therefore dominated by a single, fast decay.

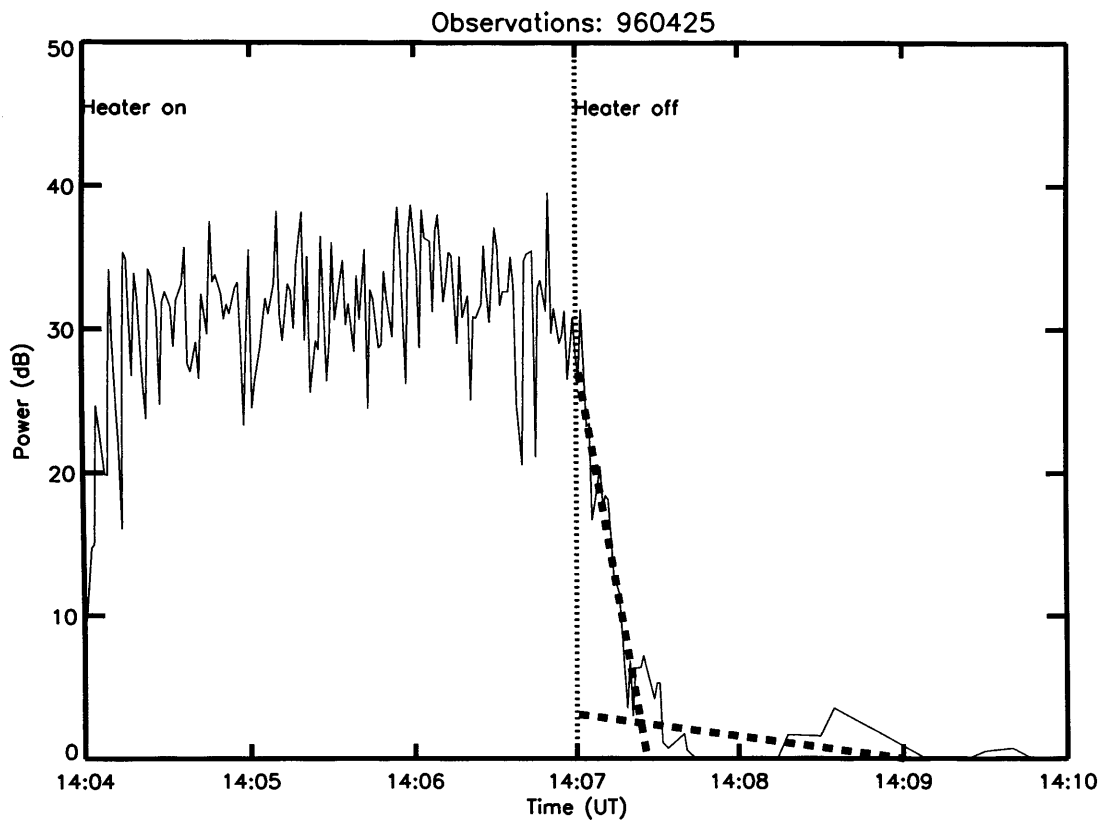
Fig. 7.5 illustrates backscatter from the time period presented in Fig. 7.3. The data is from range gate 30 of beam 5, which contained the peak returned power during this heater period. The solid line represents the data from CUTLASS, and the dotted lines are fitted functions to the data, of the same form as those described for Fig. 7.4. The decay constant for the first decay is 14 seconds. For this heater period, the second decay period is significantly above the noise, and has an intercept of 24 dB. The time constant for the second decay period is 90 seconds.

Fig. 7.6 presents calculated values of the first time constant after switch-off against UT for 22-26 April 1996. Fitting the sum of 2 exponentials to the data and then treating the 2 decays as separate is only useful when the two decay rates are very different. This represents a physical model where 2 separate decay rates are visible in the data due to their distinctly different values. Only first decays which are at least a factor of 5 less than the corresponding second decay are plotted. The circles represent data collected when CUTLASS was transmitting at 15 MHz, and the crosses indicate when CUTLASS was operating at 12.4 MHz. The plotted points each represent the decay after a 3-minute O-mode heater-on period, and no significant scatter was observed during X-mode heating. In order to avoid measurements taken during poor propagation conditions, CUTLASS data are only plotted if during heater-on a mean returned power of 25 dB was observed from the range gate containing the most intense scatter. The decay constant is calculated by fitting lines to the data after each heater period, as illustrated in Figs. 7.4 and 7.5. The plotted value is the e-fold irregularity decay time for the first of the two fitted

Finland, 25 April 1996



**Figure 7.3.** The top panel presents backscatter power measured by CUTLASS Finland along beam 5 from 1710 to 1720 on 25 April 1996. The bottom panel depicts the line of sight velocity measured by CUTLASS.



**Figure 7.4.** Backscatter power measured by CUTLASS Finland from 1404 to 1410 on 25 April 1996. The solid line represents the data from CUTLASS and the dotted lines are 2 exponential functions fitted to the data after heater-off.

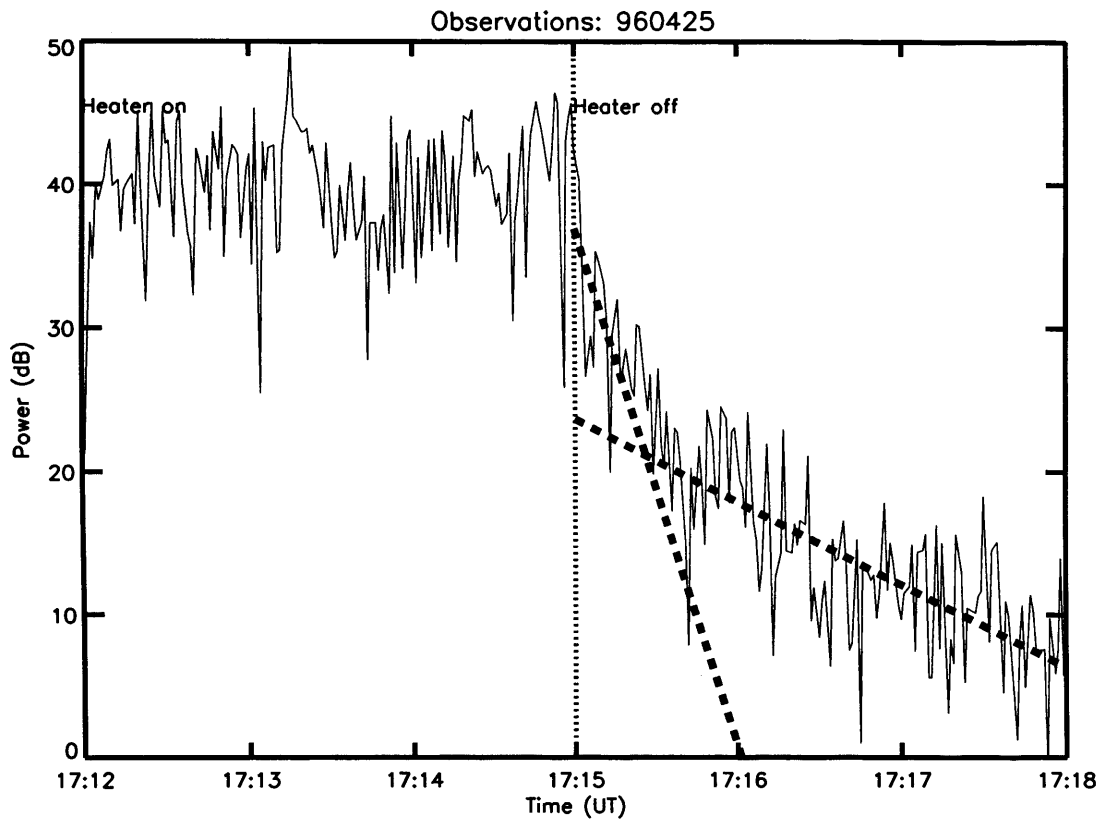


**Figure 7.5.** Backscatter power measured by CUTLASS Finland from 1712 to 1718 on 25 April 1996. The solid line represents the data from CUTLASS and the dotted lines are 2 exponential functions fitted to the data after heater-off.

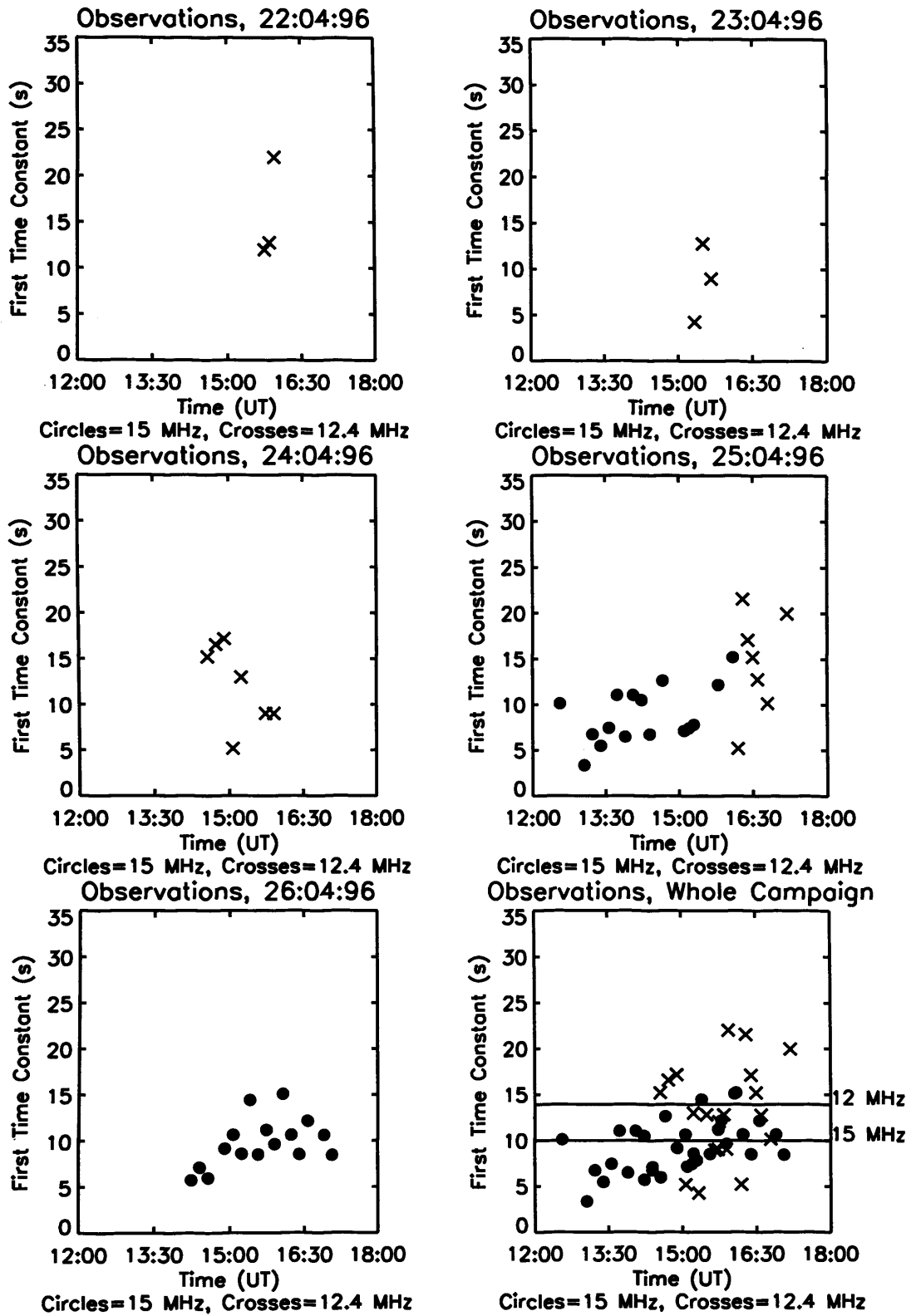


**Figure 7.6.** Time constant plotted against UT for 22-26 April 1996. The time constant plotted is the first of two constants fitted to the decay curve of heater-induced irregularities.

decays. The mean time constant for the 12.4 MHz observations is  $14 \pm 6$  s, and for the 15 MHz observations it is  $10 \pm 5$  s.

Fig. 7.7 presents values calculated for the second time constant against UT for heater periods between 22-26 April 1996. The plotted value is the e-fold irregularity decay time of the second exponential fitted to the data after heater-off. The plotted values of decay time have a minimum intercept at heater-off of 10 dB to reduce the effect of noise. The data correspond to heater periods where significant scatter was observed during heater on ( $> 25$  dB) and the values are all at least 5 times longer than the corresponding first decay.

Fig. 7.8 depicts measurements of the overall decay time of the irregularities plotted against UT. This is measured by smoothing the CUTLASS data with a running mean over 7 data points, and then determining where the smoothed data falls below 3 dB. The crosses indicate where a two stage decay was observed, defined as where the first and second decay constants differ by a factor of 5. The circles indicate single stage decay, where the two time constants differed by less than a factor of 5.

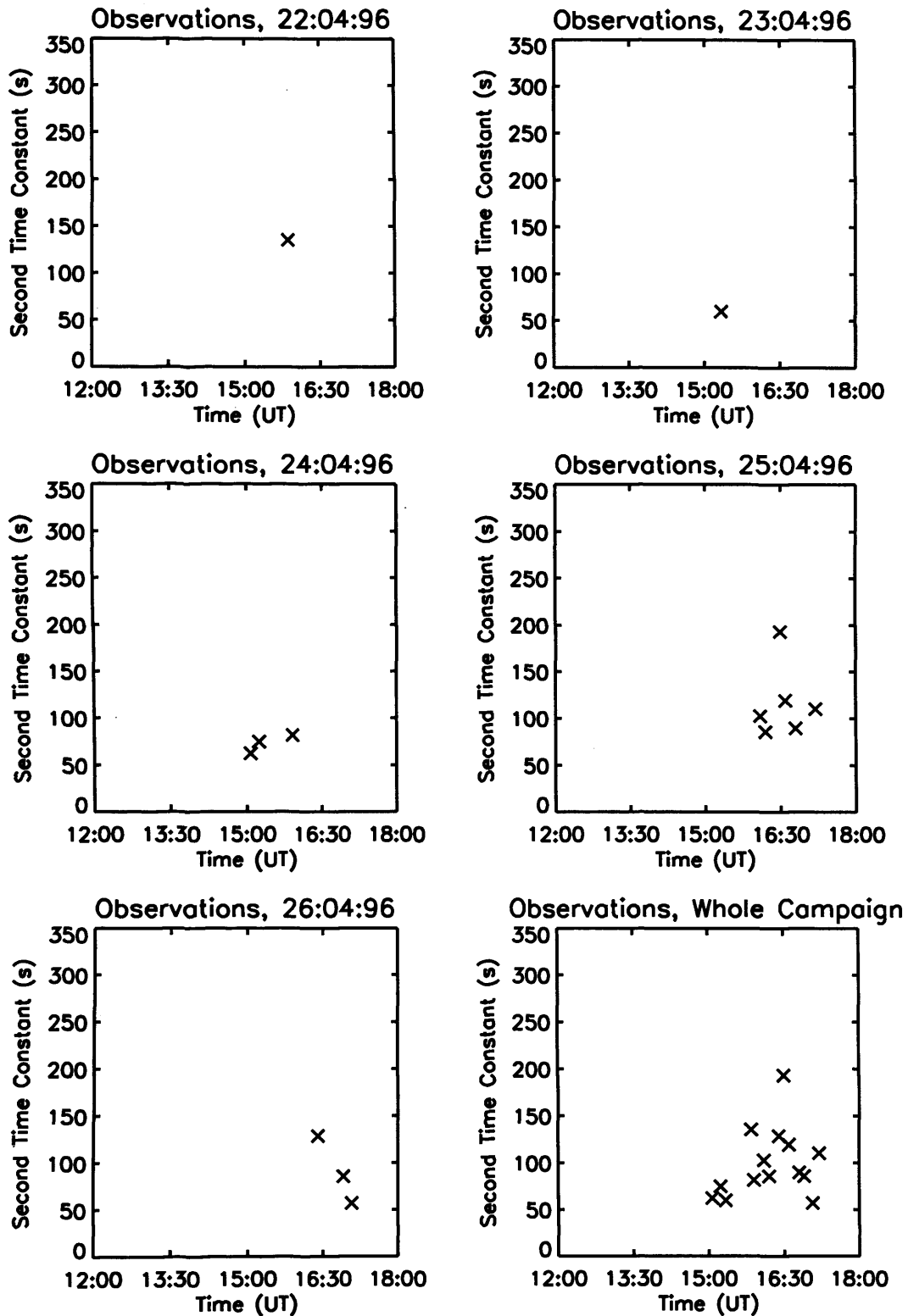
Fig. 7.9 presents values for the intercept at heater-off of the second decay curve, plotted as a function of UT for heater periods between 22-26 April 1996. The data correspond to heater periods where significant scatter was observed during heater on ( $> 25$  dB) and the values are all at least 5 times longer than the corresponding first decay.

### **7.3.2 EISCAT observations**

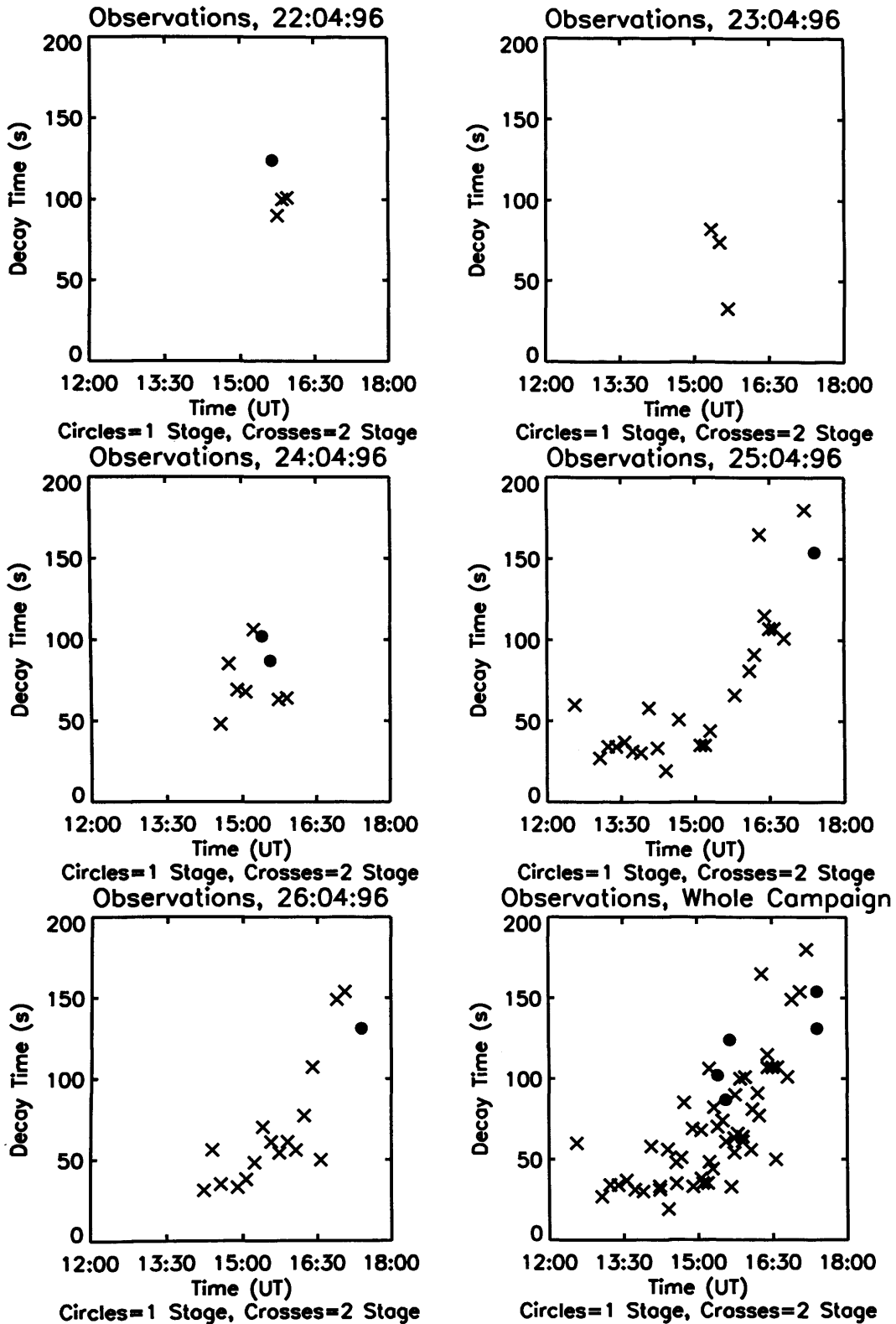
Electron and ion temperature, plotted as a function of UT for 22-26 April 1996, are presented in Fig. 7.10. The data is from the long-pulse height gate closest to 220 km, and has a high resolution of 23 km. Each point represents data averaged over heater-off periods before and after a heater-on, and so the plotted data represents undisturbed background conditions.

Fig. 7.11 illustrates the plasma flow speed plotted as a function of UT for 22-26 April 1996. The speed is calculated from tristatic velocity measurements recorded by the 3 UHF EISCAT radars. The intersection point of the radar beams, and hence the height at which the velocity was sampled, was varied during the campaign, but was typically at around 250 km.

Electron density is plotted as a function of UT in Fig 7.12. The data is from the long-pulse height gate closest to 220 km, and each point represents data averaged over heater-off periods before and after a heater-on. The bottom-right panel presents density observations over the whole campaign plotted against UT, which illustrates the dependence on time of day



**Figure 7.7.** Time constant plotted against UT for 22-26 April 1996. The time constant plotted is the second of two constants fitted to the decay curve of heater-induced irregularities.



**Figure 7.8.** Decay time plotted against UT for 22-26 April 1996. The decay time is defined as the number of seconds taken for the backscatter from the decaying irregularities to fall below 3 dB.

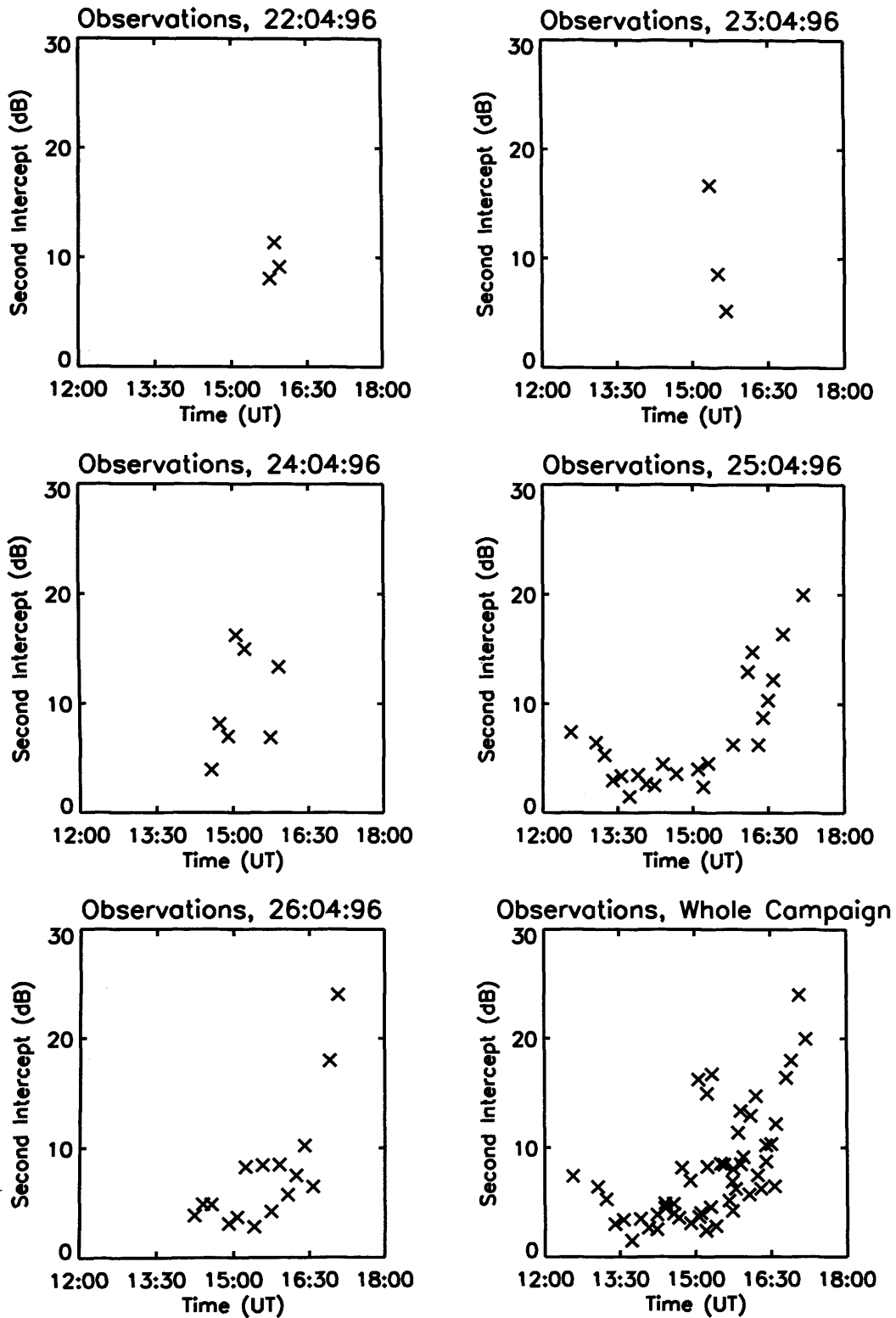


**Figure 7.9.** Intercept plotted against UT for 22-26 April 1996. The intercept plotted is for the second of two functions fitted to the decay curve of heater-induced irregularities.

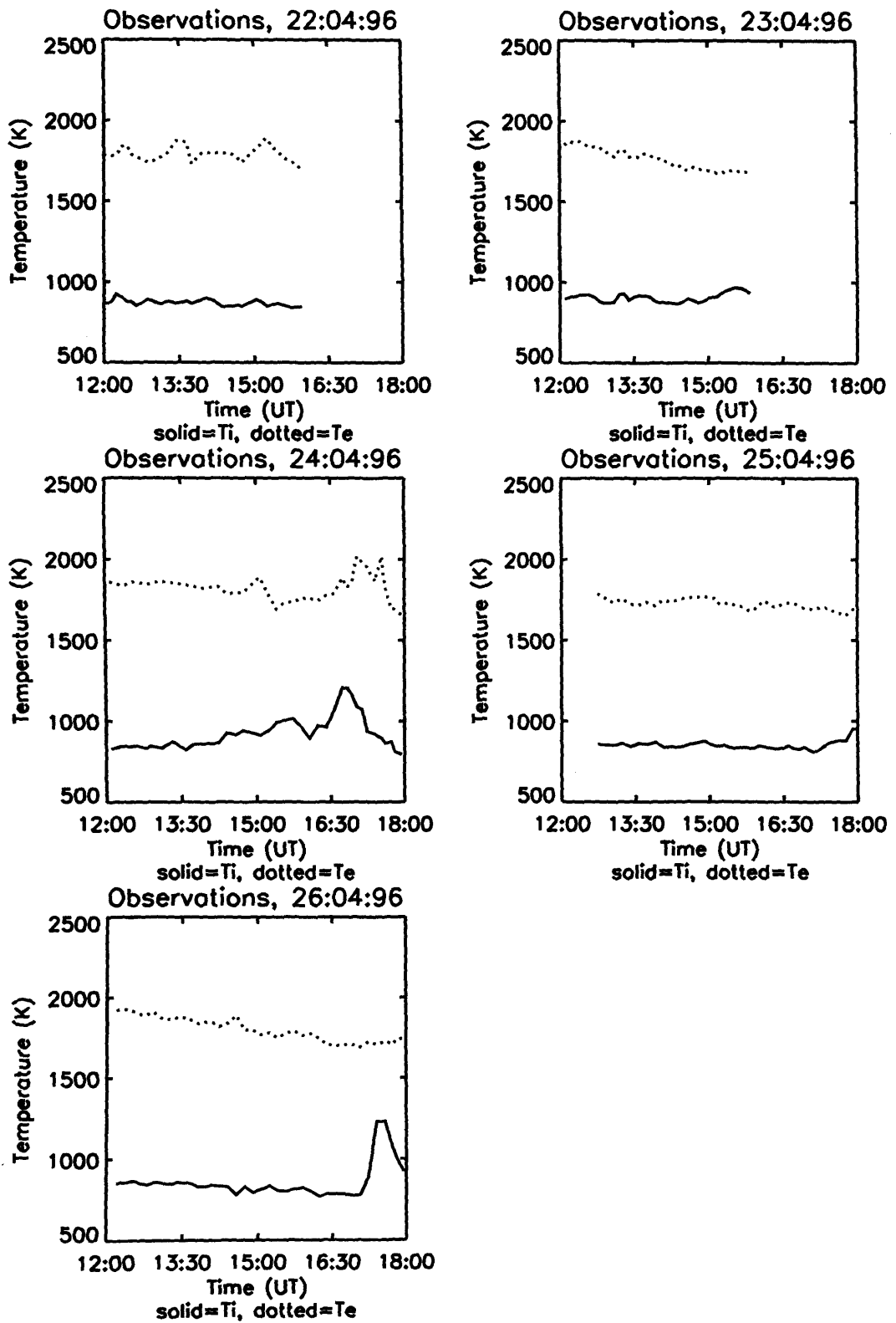


**Figure 7.10.** Electron and ion temperature plotted against UT for 22-26 April 1996. The measurements are from EISCAT long-pulse data at 220 km.

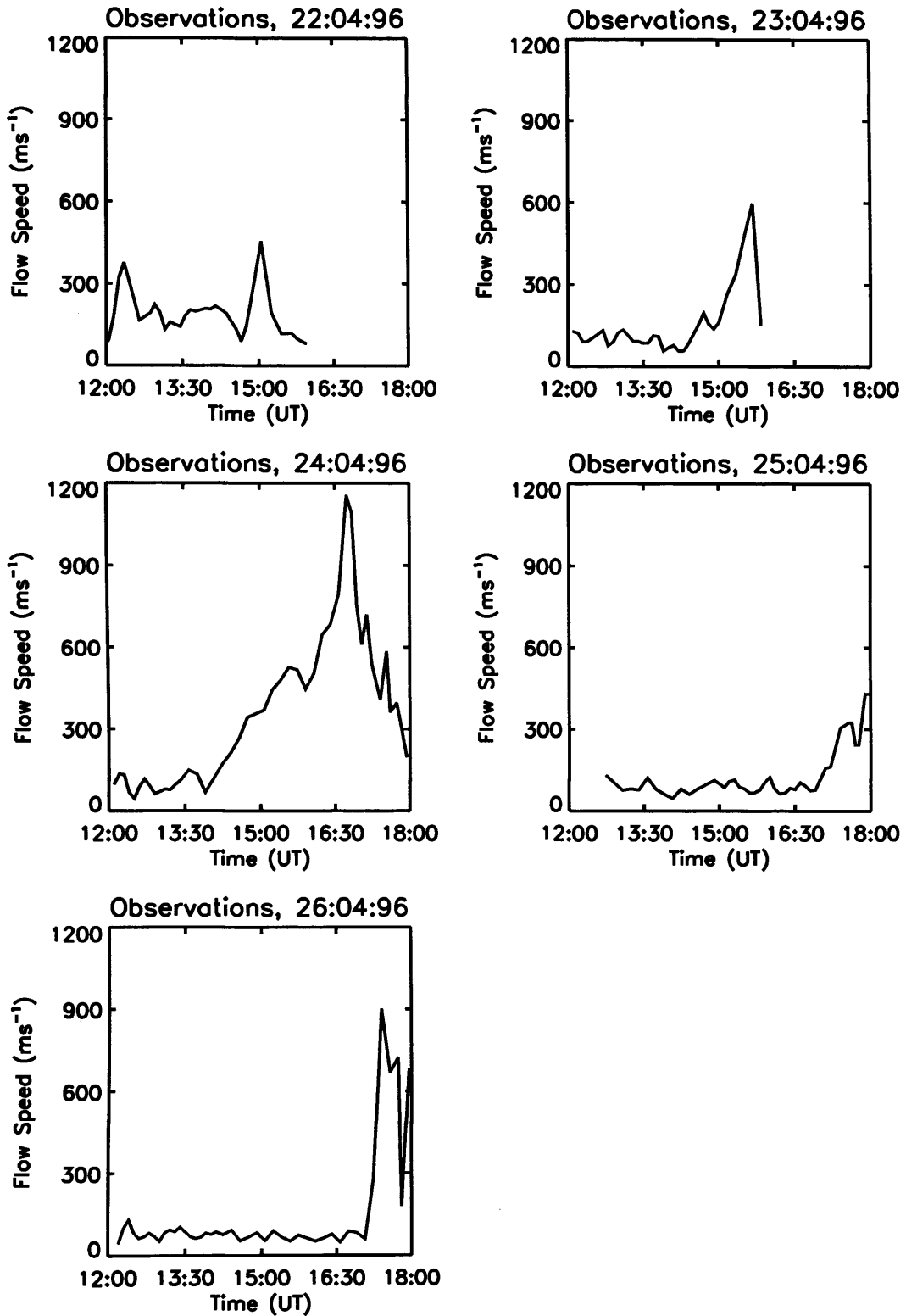


**Figure 7.11.** Flow speed plotted against UT for 22-26 April 1996. The flow speed is measured tristatically by the EISCAT UHF radar.

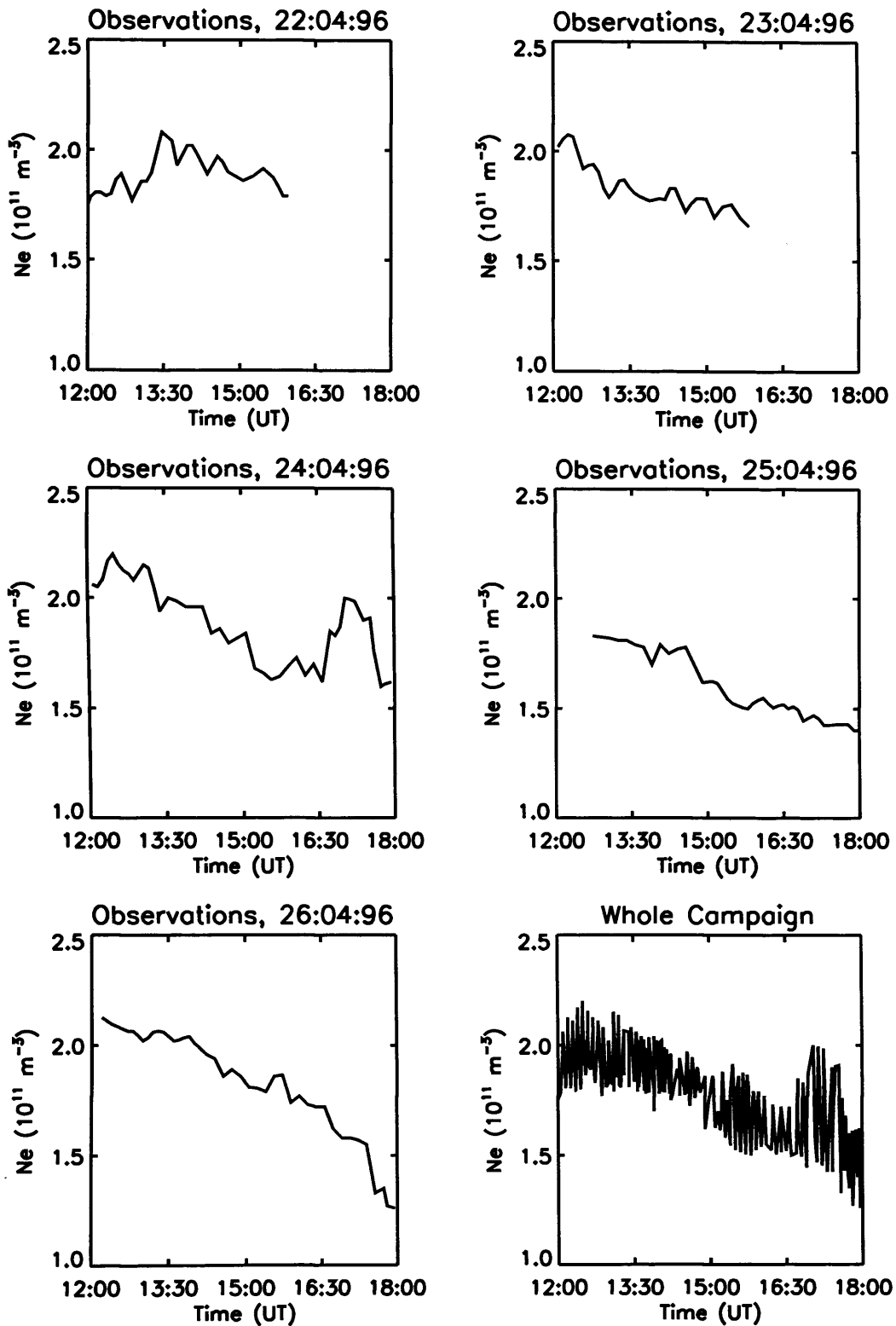


**Figure 7.12.** Electron density plotted against UT for 22-26 April 1996. The density plotted is from EISCAT long-pulse data at 220 km.

Fig. 7.13 depicts the height at which the heater wave produces irregularities. This is determined from EISCAT data by measuring the height of the ion-overshoot. The ion-overshoot is a spike in the power profile of the EISCAT data caused by the excitation of ion acoustic waves during the first few seconds of heating (e.g. Robinson, 1989). The mean interaction height for the campaign was around 220 km, and so the temperature and density data plotted in Figs 7.10 and 7.12 represent conditions close to the interaction height of the heater wave.

#### 7.4 Discussion

Previous authors (Belenov *et al.*, 1977; Coster *et al.*, 1985; Hysell *et al.*, 1996), have assumed that the first decay is controlled by ambipolar diffusion, and this mechanism is described in detail in chapter 3. Coster *et al.* (1985) utilise an expression which describes electron diffusion across the geomagnetic field. The expression depends on the cross-field irregularity scale length and has the form

$$\tau = \frac{\lambda^2}{1.2 \times 10^{-11} \Omega_e \nu_e T_e}, \quad (7.1)$$

where  $\Omega_e$  is the electron gyrofrequency,  $\nu_e$  is the electron neutral collision frequency,  $\lambda$  is the wavelength of the irregularities, and  $T_e$  is the electron temperature. Radar beams scatter from irregularities with wavelengths half that of the radar wavelength, therefore radar measurements at 15 MHz scatter from 10 m scale irregularities, and 12.4 MHz radar beams scatter from 12 m irregularities. From the EISCAT data in Fig. 7.10, the electron temperature remained around 1700 K during the campaign. Taking typical F-region values for  $\nu_e$  and  $\Omega_e$  of 200 s<sup>-1</sup> and 8.4 × 10<sup>6</sup> s<sup>-1</sup> respectively, the time constants for 15 MHz and 12.4 MHz scatter are 3 and 4 s respectively. These values are a little low compared to the experimental values plotted in Fig. 7.6, which give a time constant of 14 ± 6 s for 12.4 MHz scatter and 10 ± 5 s for 15 MHz scatter. Hysell *et al.* (1996) derive an expression for the diffusion of the irregularities parallel and perpendicular to the geomagnetic field. This produces a time constant (derived in chapter 3)

$$\frac{1}{\tau} = \frac{k_B(T_e + T_i)}{M_e \nu_e} k_{\parallel}^2 + \frac{k_B \nu_e (T_e + T_i)}{M_e \Omega_e^2} k_{\perp}^2, \quad (7.2)$$

where  $T_i$  is the ion temperature,  $k_B$  is Boltzmann's constant,  $M_e$  is the electron mass,  $\tau$  is the time constant and  $k_{\parallel}$  and  $k_{\perp}$  are the k-vectors of the irregularities parallel and perpendicular to the geomagnetic field. From Fig. 7.10, the ion

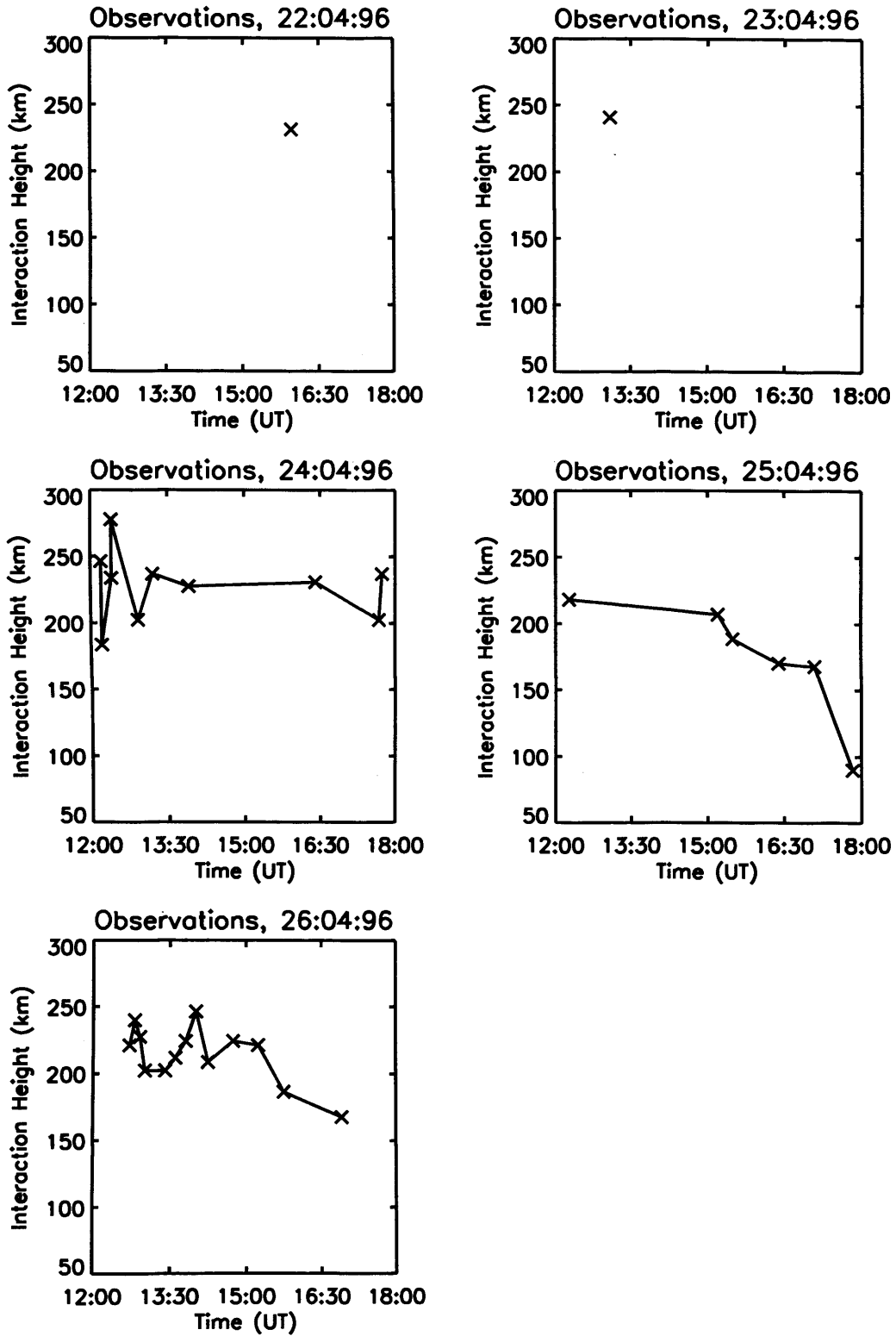


**Figure 7.13.** Interaction height plotted against UT for 22-26 April 1996. The interaction height is determined from the ion-overshoot in the EISCAT data during the first few seconds of each heater-on.

temperature during the campaign was typically around 800 K. The k-vector parallel to the geomagnetic field is probably limited to the inverse of the ionospheric scale height. From ionograms this was typically 50 km, which gives a lower limit to the parallel k-vector. The k-vector perpendicular to the geomagnetic field is simply proportional to the inverse of the irregularity scale size. Utilising these values, and the values described above for equation 7.1 yields time constants of 11.6 s for 15 MHz scatter and 12 s for 12.4 MHz scatter. These values are of the same order as those obtained from equation 7.1, and they agree with the experimental data. The parallel diffusion term is significant for the parameters appropriate to the experimental data, and as the value utilised for k-parallel represents a lower limit, a larger k-parallel could legitimately be substituted to give faster decay times.

The second decay constant is illustrated in Fig. 7.7 and has a mean value of around  $100 \pm 40$  s. The error estimate is large because the second decay time is typically measured at low levels of returned power (of order 15 dB), and the measurements are susceptible to noise. There is no obvious dependence on radar frequency or time of day. However, it is noticeable that values for the second time constant are only well determined later in the day. For times earlier than 1500 UT there are good data and significant radar backscatter observed by CUTLASS, but the second decay has an intercept of 10 dB or less and is therefore not sufficiently above the noise level to be accurately determined. The second time constant is too slow to be associated with the diffusion mechanism proposed for the first decay. Rather it may be associated with the decay of large-scale turbulence (Belenov *et al.*, 1977; Hysell *et al.*, 1996).

After heater-off, the irregularities visible to the radar decay by the mechanism illustrated in equation 7.2. The decay lasts a few seconds and is due to diffusion parallel and perpendicular to the field lines. After this initial decay, the irregularities can be sustained in the ionosphere by what is believed to be a nonlinear interaction between the FAI visible to the radar and large-scale artificial turbulence. A similar mechanism operates to produce natural small-scale irregularities. In the natural case, the small-scale irregularities grow because they are pumped by gradient drift waves. In the artificial case, artificial induced large-scale turbulent waves pump the radar-visible FAI.

Hysell *et al.* (1996) consider a 3 wave interaction where a large or intermediate scale wave decays into a radar visible FAI and an accessory wave. These authors derive the following expression for the growth of the linearly stable parasitic FAI

$$\gamma \approx \frac{E_{zonal} k_{\perp} |n_{is}|}{2Bn_0} - D_{\perp} k_{\perp}^2, \quad (7.3)$$

where  $E_{\text{conal}}$  is the naturally occurring electric field,  $n_0$  is the background electron density,  $n_{1s}$  is the amplitude of the large-scale perturbation,  $B$  is the geomagnetic field,  $D_{\perp}$  is the diffusion coefficient and  $k_{\perp}$  is the wavenumber for the small-scale FAI. Hysell *et al.* (1996) do not consider the effect of a spectrum of large-scale waves on parasitic FAI growth, but equation 7.3 does illustrate the mechanism by which the parasitic FAI are generated. The first term is the growth due to large scale turbulence and the second term is due to diffusion. The growth of the parasitic FAI depends on the amplitude of the large-scale turbulence. When the large-scale turbulence decays, so does the parasitic FAI amplitude, and it is this decay which characterises the second time constant determined from the data. The FAI growth also depends on the level of natural electric field present in the ionosphere. The EISCAT tristatic plasma velocity plotted in Fig. 7.11 is an indicator of the natural electric field, as the electric field term in equation 7.3 can be generalised to include the background electric field, gravity, neutral winds and heater-induced convection. A background plasma speed of around 100 m/s is always present, and it seems likely that this is sufficient to allow coupling between the FAI and the large-scale turbulence. Once this threshold is achieved, the natural electric field does not play an important role in determining the amplitude of the parasitic FAI. This is demonstrated by comparing Figs. 7.9 and 7.11. Fig. 7.9 depicts the intercept of the second decay curve during the campaign, and therefore provides an indication of the parasitic FAI amplitude. The intercept exhibits a general dependence on time of day which is particularly evident in the data from 25 and 26 April. On 25 April, the intercept illustrates a marked increase at around 1600 UT, and there is also an increase in the flow speed, but this does not occur until significantly later, at around 1700 UT. Similarly, there is an increase in the intercept after 1630 UT on 26 April, but this occurs before an increase is observed in the EISCAT velocity data. The electron density measured during the experiments (Fig. 7.12) decreased during the day, as would be expected. This decrease could influence the parasitic FAI amplitude, as equation 7.3 indicates that the FAI growth has an inverse dependence on electron density. The heater frequency remained at around 4 MHz during most of the experiments, and so the interaction point remained at the same electron density. However, the overall ionospheric electron density decreased during the day, and this could have influenced the parasitic FAI amplitude. It is also possible that the amplitude of the large-scale turbulence increases with time of day, which would produce a corresponding increase in the parasitic FAI amplitude.

The decay time depicted in Fig. 7.8 is a measure of the overall time taken for the irregularities to decay, and is defined by the time taken for the backscatter power to fall below 3 dB. The decay time has a dependence on time of day, being longer for later UT. One explanation for this could be preconditioning of the ionosphere by

the heater. For each day of the campaign heating began at around 1200 UT, and continued in a series of 2-3 minute heater on periods separated by heater off periods of 2-3 minutes. This heating could have a cumulative effect on the decay time of the irregularities. However, the decay time increases over a period of 6 hours, and it is likely that a preconditioning effect would saturate in minutes rather than hours.

Kagan and Frolov (1996) have also observed a diurnal variation in the decay time of heater-induced irregularities. These authors utilised diagnostic stimulated electromagnetic emission (DSEE) to establish the decay characteristics of irregularities generated by the SURA heating facility in Russia. They observed steady daytime values for the decay, which then increased abruptly at local sunset, before reaching new stable values.

The time constants for the first and second decays, depicted in Figs. 7.6 and 7.7, do not exhibit a significant dependence with time of day. However, the second decay intercept and the time taken for the backscatter to fall below 3 dB both exhibit a time of day dependence. This suggests that the length of time for which irregularities remain visible in the ionosphere is not characterised by the decay constants themselves, but rather by the point at which the second decay regime takes over. It is the parasitic FAI produced by the artificial large-scale turbulence which determine the length of time for which visible irregularities persist in the ionosphere.

## 7.5 Summary

The decay characteristics of artificial field aligned irregularities after heater-off have been diagnosed by CUTLASS. Irregularities have been observed to remain in the ionosphere for a number of minutes after heater-off. By fitting the sum of two exponential functions to the backscatter power received by CUTLASS after each heater period, a distinct two stage decay process has been identified. Following the work of previous authors (Belenov *et al.*, 1977; Coster *et al.*, 1985; Hysell *et al.*, 1996) the first decay constant is attributed to diffusion of small-scale irregularities and the second decay constant is characteristic of large-scale decay. The first time constant has a value of around 10 s and represents the diffusion along and across the field lines of artificial irregularities isolated by the frequency of the radar beam. The second time constant has a value of around 100 s and represents the decay of large-scale irregularities, which undergo mode conversion and are therefore visible to an HF radar. A link has been established between the time of day of the observations and the time taken for the irregularities to decay into the noise. The time constants themselves do not illustrate a dependence on time of day, and neither does the initial irregularity level at heater off. However, the level at which the

second time constant becomes significant does illustrate a dependence on time of day. This indicates that the parasitic FAI produced by artificial large-scale turbulence are an important factor in determining the length of time for which decaying irregularities remain visible to the radar. Furthermore, the amplitude of the parasitic FAI increases during the day.

## **Chapter 8**

# ***Summary and Conclusions***

### **8.1 Introduction**

In this thesis the results of experimental and modelling studies of artificial modification of the ionosphere have been presented. The EISCAT ionospheric modification facility at Tromsø, Northern Norway has been utilised in two experimental campaigns in February 1995 and April 1996. The February 1995 campaign was principally concerned with modification of the auroral electrojet region during both disturbed and quiet conditions. For this experiment the most significant diagnostic tool was the EISCAT UHF incoherent scatter radar. This provided measurements of electron and ion temperature, electron density and plasma flow speed. In addition, the dynasonde at Tromsø was utilised to measure the peak plasma frequency in the ionosphere, which facilitated normalisation of the electron density values provided by EISCAT. For the April 1996 experimental campaign the most important diagnostic was the CUTLASS coherent radar system. CUTLASS measures power backscattered from field aligned irregularities produced during heating, and can be utilised to map the spatial extent and the temporal development of the irregularities. During the April 1996 campaign, the EISCAT incoherent scatter radar was available to record complimentary measurements of bulk ionospheric parameters.

In addition to these experimental studies, a computer model has been developed to investigate the electron temperature and density changes which are induced in the ionospheric D- and E-regions during periods of electrojet activity.

### **8.2 Summary of principal observations**

The results of the experimental and modelling investigations in this thesis may be summarised as follows:

a) The artificially induced perturbation in bulk electron temperature in the auroral E-region has been measured under both disturbed and quiet periods of plasma flow. During quiet conditions the underdense artificial increase in electron temperature was found to be of order 100 K. When the plasma flow speed increased to a level above the threshold for the Farley-Buneman instability, a natural increase in electron temperature was recorded of a few 100 K. When the heater was switched on during high plasma flow conditions a net decrease was observed in the electron temperature. This represents the first experimental confirmation of the theory of

Robinson (1994), which predicts a direct interaction between the heater wave and the instability which can cause quenching of the instability mechanism. Robinson (1994) found that during artificial heating the natural heating contribution can be reduced or eliminated, and the energy input from the heater wave is not enough to compensate, leading to an overall electron temperature decrease.

The cooling was observed when the RF wave interacted strongly with a wide range of heights in the electrojet, and when there is little or no D-region absorption. When the RF wave interacted with the instability at a narrow height range, the data suggests that although there was no cooling, there was a reduction in the heating efficiency of the RF wave.

b) A self-consistent computer code has been developed which calculates the electron temperature and density perturbations produced by a high power radio wave propagating through the auroral D- and E-regions. The model results are in agreement with previous studies (Tomko *et al.*, 1980; Meltz *et al.*, 1982; Milikh *et al.*, 1995) which indicate that significant electron temperature enhancement occurs in the D-region, where the power of the HF wave is high, but the electron density is low. For the first time, the model also includes the energy contribution due to Farley-Buneman heating in the electrojet, and frictional heating due to plasma flow. During quiet conditions, *i.e.* with the natural electric field switched off, the heater wave produces an electron temperature enhancement of order 100 K at electrojet heights, which is consistent with the experimental observations reported in chapter 5. When the natural electric field is introduced, the Farley-Buneman heating term becomes the most significant contribution to the overall heating effect between 105 and 120 km. When the heater is turned on during model disturbed conditions, the artificial fractional temperature and density increase is less than the corresponding artificial increase under quiet conditions. This indicates that the efficiency of the RF heating is reduced under disturbed conditions.

Using experimental values for flow speed, the model gives quantitative agreement with the EISCAT values for naturally enhanced electron temperatures.

c) The CUTLASS coherent scatter radar has been utilised to diagnose the horizontal spatial extent of the heated region over Tromsø. Coherent scatter radars measure backscatter from the field aligned irregularities generated near the reflection point of the heater wave. During the experiments, the resolution of CUTLASS over Tromsø was around 15 km in range and 45 km in azimuth. In order to establish the true size of the heated patch the pulse shape and the beam pattern of the radar were deconvolved from the backscatter power as measured by the radar. Gaussian functions were employed to represent the data, pulse shape and beam shape.

Gaussians were chosen as they are simple functions which are defined only in terms of their height and width, and width was the only parameter of concern. The deconvolved data indicate that irregularities were excited significantly outside the 3 dB point of the heater beam, which is often used to describe the width of the heated region. In fact, irregularities were observed as far out as the 18 dB point of the heater beam. Also during this campaign, the first observations were made of artificial irregularities with the Iceland component of the CUTLASS radar. The Iceland data were generally poorer than those from Finland, and Finland data were utilised for the bulk of the analysis. Both radars located the heated patch directly over the Tromsø heater site, which is useful confirmation of the mapping ability of CUTLASS.

d) The decay characteristics of artificial field aligned irregularities after heater-off have been diagnosed by CUTLASS. Irregularities have been observed to remain in the ionosphere for a number of minutes after heater-off. By fitting the sum of two exponential functions to the backscatter power received by CUTLASS after each heater period, a distinct two stage decay process has been identified. Following the work of previous authors (Belenov *et al.*, 1977; Coster *et al.*, 1985; Hysell *et al.*, 1996) the first decay constant is attributed to diffusion of small-scale irregularities and the second decay constant is characteristic of large-scale decay. The first time constant has a value of around 10 s and represents the diffusion along and across the field lines of artificial irregularities isolated by the frequency of the radar beam. The second time constant has a value of around 100 s and represents the decay of large-scale irregularities, which undergo mode conversion and are therefore visible to an HF radar. For the first time a link has been established between the time of day of the observations and the time taken for the irregularities to decay into the noise. The time constants themselves do not illustrate a dependence on time of day, and neither does the initial irregularity level at heater off. However, the level at which the second time constant becomes significant does illustrate a dependence on time of day. This indicates that the amplitude of artificial large-scale irregularities is an important factor in finding the length of time for which artificial irregularities remain visible to the radar after heater-off. Furthermore, the amplitude of large-scale irregularities increases during the day.

### 8.3 Further work

In this thesis results from one of the first artificial modification campaigns to employ the CUTLASS radar system have been presented. The results from this early campaign have been very encouraging, and further campaigns involving

CUTLASS promise to reveal more about the mechanisms involved in the formation of artificial irregularities. Planned experiments include stepping the ERP of the Tromsø heater and observing the resulting irregularities with CUTLASS. The results from chapter 6 demonstrate that CUTLASS is capable of observing artificial irregularities excited at very low power levels, stepping the power of the heater will facilitate further investigation of the threshold effects involved in irregularity production. In addition, the effects of preconditioning can be investigated by varying the length of time between heater on periods. Another area for further study is the frequency dependence of irregularity decay. A coherent scatter radar isolates irregularities in the ionosphere with scale lengths determined by the frequency of the radar beam. The results from chapter 7 indicate that the decay of artificial irregularities in the ionosphere is dependent on the irregularity scale size. So far, only 2 CUTLASS frequencies have been utilised over long periods to observe the decay of the irregularities. In future, a greater range of CUTLASS frequencies can be employed to diagnose the heated volume, and hence provide a more systematic picture of the relationship between decay time and radar frequency.

The results of chapter 7 illustrate that irregularities remain in the ionosphere for longer later in the day. Experiments thus far have run between around 1200 and 1800 UT. To investigate the true diurnal dependence of irregularity decay time it will be necessary to perform experiments for longer periods, which may prove difficult. The level of ionisation decreases during the night, and the radar beam is refracted less, making the orthogonality condition difficult to achieve over the heater site. Nevertheless, it will be useful to determine how much further the observing envelope can be extended.

In a typical CUTLASS scan, many of the range cells do not return a significant level of scatter. This is because coherent scatter requires irregularities to be present to facilitate Bragg-like scattering of the radar beam. Under quiet geophysical conditions, when no natural irregularities are excited, very little data is recorded by CUTLASS. Spatial observations of the heated volume with CUTLASS have demonstrated how the artificial irregularities provide a very effective target for CUTLASS backscatter. This artificial target can be exploited for geophysical applications. Utilising a very wide heater beam, achievable by transmitting on fewer antennas, can enable the heater to illuminate the ionosphere over a wide area. This will facilitate CUTLASS observations of flow patterns at very low velocities, which would normally be invisible to coherent radars.

The model of a heater wave propagating through the auroral D- and E-regions could be expanded to include more complicated effects. The model presently only considers underdense heating, a more advanced version could model the effects of a heater wave reflecting within the auroral region. A heater wave produces a stronger

effect at its reflection point, and it would be interesting to see if this could be reproduced in a model. The theory of Robinson (1994), which predicts a cooling effect when the heater is turned on during periods of high natural electrojet current, could also be included in the model. This would allow direct comparison between modelled electrojet heating and the data collected on February 6 1995, where the artificial cooling effect was first demonstrated, and would provide a very useful confirmation of the preliminary result.

The data presented in this thesis represents the first experimental evidence for artificial cooling in the electrojet. However, the effect was only observed on one day of the campaign and the data are somewhat preliminary in nature. A future campaign to confirm the effect is therefore desirable. A useful additional diagnostic to confirm the effect would be a coherent scatter radar to look into the E-region over Tromsø. This role could be fulfilled by the Leicester University RAPIER (Relocatable Auroral Polar Experimental Radar) system (Popple *et al.*, 1997). RAPIER is a VHF system, and so its radar beam propagates in an approximately straight line direction, in contrast to the refracted propagation associated with CUTLASS. RAPIER could be co-located with CUTLASS in Finland, and the complimentary propagation characteristics of the two radars would mean that CUTLASS could observe the F-region whilst RAPIER observed the E-region. The Farley-Buneman instability produces wave turbulence which can be detected directly by a coherent scatter radar such as RAPIER. This direct measurement method provides a more satisfactory way to observe the turbulence, instead of having to rely on the temperature increase produced by the turbulence. If quenching of the instability occurs during heating, RAPIER should be able to observe the effect in radar backscatter measurements.

It has recently been suggested that artificial modification research could be applied to geological prospecting. ULF (Ultra Low Frequency) electromagnetic waves are a useful tool in mapping the subsurface of the Earth. When an EM wave is incident on a conducting surface such as the Earth, the depth to which it penetrates, the skin depth, is determined by the wavelength of the wave. For instance, to penetrate to depths useful for oil prospecting a wavelength of a few thousand km is required, this corresponds to the ULF frequency band. To produce EM waves with a conventional antenna, it is usually necessary for the antenna to have dimensions of the same order as the wavelength of the waves. This is clearly impossible for ULF waves, and so geologists utilise natural ULF sources such as thunderstorms or magnetospheric pulsations, and this is already an established technique in the petroleum industry. Electromagnetic sensors are placed on the ground to measure the currents induced in the subsurface by the ULF waves. Computer inversion routines are then utilised to provide a picture of the subsurface.

Natural ULF sources have limitations, both in the range of frequencies they provide and the regularity with which they are generated. An alternative is to generate artificial ULF waves, employing the auroral electrojet as an antenna. The model calculations in chapter 5 demonstrate that the temperature and density in the electrojet can be modulated by the heater. The conductivity in the electrojet is dependent on the density and temperature, and so by pulsing the heater on and off, ULF waves can be produced at the modulation frequency. This technique has the added advantage that the ground sensing equipment and computer software developed for use with natural ULF waves is equally useful for artificial waves. Recent experiments with the HIPAS facility in Alaska have demonstrated that the concept is worth pursuing, and it is hoped that field trials with the EISCAT heater will demonstrate that the technique is viable.

## References

- Allen, E. M., G. D. Thome and P. B. Rao, HF phased array observations of heater-induced spread-F, *Radio Science*, **9**, 905-916, 1974.
- Bailey V. A., On some effects caused in the ionosphere by electric waves, *Phil. Mag.*, **26**, 425-453, 1938.
- Bailey V. A., Some possible effects caused by strong gyrowaves in the ionosphere, 1, *J. Atmos. Terr. Phys.*, **14**, 299-324, 1959
- Bailey G. J. and R. Sellek, A mathematical model of the Earth's plasmasphere and its application in a study of He<sup>+</sup> at L=3, *Ann. Geophys.*, **8**, 171-190, 1990.
- Belenov, A. F., V. A. Bubnov, L. M. Erukhimov, Yu. V. Kiselev, G. P. Komrakov, E. E. Mityakova, L. N. Rubstov, V. P. Uryadov, V. L. Frolov, Yu. V. Chagnuov, and B. V. Ykhmatov, Parameters of artificial small-scale ionospheric irregularities, *Radiophys. Quantum Electron. Engl. Transl.*, **20**, 1240-1250, 1977.
- Bowles, K. L., Observations of vertical incidence scatter from the ionosphere at 41 Mc/sec. *Phys. Rev. Lett.*, **1**, 454, 1958.
- Budden, K. G., The propagation of radio waves, *Cambridge University Press, Cambridge*, 1985.
- Buneman, O., Excitation of field aligned sound waves by electron streams, *Phys. Rev. Lett.*, **10**, 285-287, 1963.
- Carroll, J. C., E. J. Violette, and W. F. Utlaut, The Platteville high power facility, *Radio Science*, **9**, 889-894, 1974.
- Chapman, S., The absorption and dissociative or ionizing effect of monochromatic radiation in an atmosphere on a rotating earth, *Proc. Phys. Soc. (London)*, **43**, 26-45, 1931.
- Chaturvedi, P. K. and S. L. Ossakow, Plasma Instabilities in the High-Latitude E Region Induced by High-Power Radio Waves, *J. Geophys. Res.*, **95**, 15,185-15,193, 1990.
- Coster, A. J., F. T. Djuth, R. J. Jost, and W. E. Gordon, The Temporal Evolution of 3-m Striations in the Modified Ionosphere, *J. Geophys. Res.*, **90**, 2807-2818, 1985.
- Das, A. C., and J. A. Fejer, Resonance Instability of Small-Scale Field Aligned Irregularities, *J. Geophys. Res.*, **84**, 6701-6704, 1979.
- Davies, K., *Ionospheric Radio*, Peregrinus, London, 1990.
- Devlin, T., J. K. Hargreaves, and P. N. Collins, EISCAT observations of the ionospheric D-region during auroral radio absorption events, *J. Atmos. Terr. Phys.*, **48**, 785-805, 1986.

- Djuth, F. T., R. J. Jost, S. T. Noble, W. E. Gordon, P. Stubbe, H. Kopka, E. Nielsen, R. Boström, H. Derblom, Å. Hedberg and B. Thidé**, Observations of E Region Irregularities Generated at Auroral Latitudes by a High-Power Radio Wave, *J. Geophys. Res.*, **90**, 12,293-12,306, 1985.
- Djuth, F. T., B. Thidé, H. M. Ierkic and M. P. Sulzer**, Large F-region electron-temperature enhancements generated by high-power HF radio waves, *Geophys. Res. Lett.*, **14**, 953-956, 1987.
- Dougherty, J. P. and D. T. Farley**, A theory of incoherent scattering of radio waves by a plasma, *Proc. R. Soc.*, A259, **79**, 1960.
- Farley, D. T.**, A plasma instability resulting in field-aligned irregularities in the ionosphere, *J. Geophys. Res.*, **68**, 6083-6097, 1963.
- Farley, D. T.**, Multiple-pulse incoherent scatter correlation function measurements, *Radio Science*, **4**, 935, 1969.
- Farley, D. T.**, Incoherent scatter correlation function measurements, *Radio Science*, **7**, 661, 1972.
- Fialer, P. A.**, Field-aligned scattering from a heated region of the ionosphere-Observations at HF and VHF, *Radio Science*, **9**, 923-940, 1974.
- Gordon, W. E.**, Incoherent scattering of radio waves by free electrons with applications to space exploration by radar, *Proc. IRE*, **46**, 1824, 1958.
- Gordon, W. E., H. C. Carlson and R. L. Showen**, Ionospheric heating at Arecibo: First Tests, *J. Geophys. Res.*, **76**, 7808-7813, 1971.
- Gordon, W. E. and H. C. Carlson**, Arecibo heating experiments, *Radio Science*, **9**, 1041-1047, 1974.
- Greenwald R. A., K. B. Baker, R. A. Hutchins and C. Hanuise**, An HF-phased array radar for studying small-scale structure in the high-latitude ionosphere, *Radio Science*, **20**, 63-79, 1985.
- Greenwald R. A., K. B. Baker, J. R. Dudeney, M. Pinnock, T. B. Jones, E. C. Thomas, J-P. Villain, J-C. Cerisier, C. Senior, C. Hanuise, R. D. Hunsucker, G. Sofko, J. Koehler, E. Nielsen, R. Pellinen, A. D. M. Walker, N. Sato, and H. Yamagishi**, DARN/SuperDARN: A global view of the dynamics of high-latitude convection, *Space Sci. Rev.*, **71**, 761-796, 1995.
- Gurevich, A. V.**, *Nonlinear Phenomena in the Ionosphere*, Springer, New York, 1978.
- Hagfors, T.**, Electromagnetic wave propagation in a field-aligned-striated cold magnetoplasma with application to the ionosphere, *J. Atmos. Terr. Phys.*, **46**, 211-216, 1984.
- Hanuise C., Å. Hedberg, J. Oksman, E. Nielsen, P. Stubbe and H. Kopka**, Comparison between the ionospheric plasma drift and the motion of

- artificially induced irregularities as observed by HF backscatter radars, *Ann. Geophys.*, **4**, A, 1, 49-54, 1986.
- Hanuse C., J. P. Villain, D. Gresillon, B. Cabrit, R. A. Greenwald and K. B. Baker**, Interpretation of HF radar ionospheric Doppler spectra by collective wave scattering theory, *Ann. Geophys.*, **11**, 29-39, 1993.
- Hedberg, Å., H. Derblom, B. Thidé, H. Kopka and P. Stubbe**, Observations of HF backscatter associated with the heating experiment at Tromsø, *Radio Science*, **18**, 840-850, 1983.
- Hedberg, Å., H. Derblom, G. Wannberg, B. Thidé, H. Kopka and P. Stubbe**, Measurements of HF backscatter cross sections for striations created by ionospheric heating at different power levels, *Radio Science*, **21**, 117-125, 1986.
- Hibberd, F. H., E. Nielsen, P. Stubbe, H. Kopka and M. T. Rietveld**, Production of Auroral Zone E Region Irregularities by Powerful HF Heating, *J. Geophys. Res.*, **88**, 6347-6351, 1983.
- Høeg, P., E. Nielsen, P. Stubbe, and H. Kopka**, Heater-Induced 1-Meter Irregularities, *J. Geophys. Res.*, **91**, 11,309-11,320, 1986.
- Hysell, D. L., M. C. Kelley, Y. M. Yampolski, V. S. Beley, A. V. Koloskov, P. V. Ponomarenko and O. F. Tyrnov**, HF radar observations of decaying artificial field-aligned irregularities, *J. Geophys. Res.*, **101**, 26,981-26,993, 1996.
- Inhester, B., A. C. Das and J. A. Fejer**, Generation of Small-Scale Field-Aligned Irregularities in Ionospheric Heating Experiments, *J. Geophys. Res.*, **86**, 9101-9106, 1981.
- Jones, R. M. and J. J. Stephenson**, A versatile three-dimensional raytracing computer program for radio waves in the ionosphere, *Technical report OT75-76*, U. S. Dept. of Commerce, Washington D. C., U. S. A., 1975.
- Jones, T. B., T. R. Robinson, P. Stubbe and H. Kopka**, Phase Changes Induced in a Diagnostic Radio Wave Passing Through a Heated Region of the Auroral Ionosphere, *J. Geophys. Res.*, **87**, 1557-1564, 1982.
- Jones, T. B., T. R. Robinson, P. Stubbe and H. Kopka**, EISCAT observations of the heated ionosphere, *J. Atmos. Terr. Phys.*, **48**, 1027-1035, 1986.
- Kagan., L. M. and V. L. Frolov**, Significance of field-aligned currents for F-region perturbations, *J. Atmos. Terr. Phys.*, **58**, 1465-1474, 1996.
- Kelley, M. C.**, *The Earth's Ionosphere*, Academic Press, New York, 1989.
- Korovin, A. V., A. M. Nasyrov, E. V. Proskurin, and N. N. Yagnov**, Doppler frequency variations in the field-aligned scattering of VHF

- waves by artificial irregularities of the ionosphere, *Radiophys. Quantum Electron. Engl. Transl.*, **25**, 195-199, 1982.
- Lee, M. C. and S. P. Kuo**, Excitation of upper-hybrid waves by a thermal parametric instability, *J. Plasma Physics*, **30**, part 3, 463-478, 1983.
- Mantas, G. P., H. C. Carlson, jr. and C. H. LaHoz**, Thermal response of the F region ionosphere in artificial modification experiments by HF radio waves, *J. Geophys. Res.*, **86**, 561-574, 1981.
- Meltz, G., L. H. Holway, jr. and N. M. Tomljanovich**, Ionospheric heating by powerful radio waves, *Radio Science*, **9**, 1049-1063, 1974.
- Meltz, G., C. M. Rush and E. J. Violette**, Simulation of D and E region high-power microwave heating with HF ionospheric modification experiments, *Radio Science*, **17**, 701-715, 1982.
- Milikh., G. M., M. J. Freeman and L. M. Duncan**, First estimates of HF-induced modifications of the D region by the HF Active Auroral Research Program facility, *Radio Science*, **29**, 1355-1362, 1994.
- Minkoff, J., P. Kugelmann and I. Weissman**, Radio frequency scattering from a heated ionospheric volume, 1, VHF/UHF field-aligned and plasma-line backscatter measurements, *Radio Science*, **9**, 941-956, 1974.
- Minkoff, J. and R. Kreppel**, Spectral Analysis and Step Response of Radio Frequency scattering From a Heated Ionospheric Volume, *J. Geophys. Res.*, **81**, 2844-2856, 1976.
- Mjølhus, E.**, On linear conversion in a magnetized plasma, *Radio Science*, **25**, 1321-1339, 1990.
- Newman A. L., H. C. Carlson, jr., G. P. Mantas and F. T. Djuth**, Thermal response of the F-region ionosphere for conditions of large HF-induced electron-temperature enhancements, *Geophys. Res. Lett.*, **15**, 311-314, 1988.
- Noble S. T., F. T. Djuth, R. J. Jost, W. E. Gordon, Å. Hedberg, B. Thidé, H. Derblom, R. Boström, E. Nielsen, P. Stubbe and H. Kopka**, Multiple frequency radar observations of high-latitude E region irregularities in the HF modified ionosphere, *J. Geophys. Res.*, **92**, 13613-13627, 1987.
- Popple, M., P. J. Chapman, E. C. Thomas and T. B. Jones**, RAPIER: a new relocatable VHF coherent radar, *J. Atmos. Sol. Terr. Phys.*, **59**, 1035-1048, 1997.
- Rietveld, M. T., H. Kohl, H. Kopka, and P. Stubbe**, Introduction to ionospheric heating at Tromsø - 1. Experimental overview, *J. Atmos. Terr. Phys.*, **55**, 577-599, 1993.
- Rishbeth, H. and P. J. S. Williams**, The EISCAT Ionospheric Radar: the System and its Early Results, *Q. Jl R. astr. Soc.*, **26**, 478-512, 1985.

- Robinson, T. R.**, Towards a self-consistent non-linear theory of radar auroral backscatter, *J. Atmos. Terr. Phys.*, **48**, 417-422, 1986.
- Robinson, T. R.**, The heating of the high latitude ionosphere by high power radio waves, *Physics Reports*, **179**, 79-209, 1989.
- Robinson, T. R.**, The role of natural E-region plasma turbulence in the enhanced absorption of HF radio waves in the auroral ionosphere: Implications for RF heating of the auroral electrojet, *Ann. Geophys.*, **12**, 316-332, 1994.
- Robinson, T. R., F. Honary, A. Stocker and T. B. Jones**, Factors influencing the heating of the auroral electrojet by high power radio waves, *Adv. Space Res.*, **12**, (12)41-(12)44, 1995.
- Robinson, T. R., F. Honary, A. J. Stocker, T. B. Jones and P. Stubbe**, First EISCAT observations of the modification of F-region electron temperatures during RF Heating at harmonics of the electron gyro frequency, *J. Atmos. Terr. Phys.*, **58**, 385-395, 1996.
- Robinson, T. R., A. J. Stocker, G. E. Bond, P. Eglitis, D. M. Wright and T. B. Jones**, O- and X-mode heating effects observed simultaneously with the CUTLASS and EISCAT radars and low power HF diagnostics at Tromsø, *Ann. Geophys.*, **15**, 134-136, 1997.
- Sharma, A. K.**, Effect of RF on Type II Electrojet Instability, *J. Geophys. Res.*, **94**, 3805-3807, 1989.
- Schlegel, K., M. Rietveld, and A. Maul**, A modification event of the auroral E region as studied with EISCAT and other diagnostics, *Radio Science*, **22**, 1063-1072, 1987.
- Schunk, R. W. and A. F. Nagy**, Electron temperatures in the F-region of the ionosphere: Theory and observations., *Rev. Geophys. Space Phys.*, **16**, 5169-5183, 1978
- Showen, R. L.**, Artificial Heating of the Lower Ionosphere, *J. Geophys. Res.*, **77**, 1923-1933, 1972
- Stocker, A. J., F. Honary, T. R. Robinson, T. B. Jones, P. Stubbe and H. Kopka**, EISCAT observations of large scale electron temperature and electron density perturbations caused by high power HF radio waves, *J. Atmos. Terr. Phys.*, **54**, 1555-1572, 1992.
- Stocker, A. J., F. Honary, T. R. Robinson and T. B. Jones**, Anomalous Absorption During Artificial Modification at Harmonics of the Electron Gyrofrequency, *J. Geophys. Res.*, **98**, 13627-13634, 1993.
- Stubbe, P. and H. Kopka**, Ionospheric modification experiments in northern Scandinavia - a description of the Heating project, *Report MPAE-W-02-79-04, Max-Planck-Institut für Aeronomie, F.R.G.*, 1979.

- Stubbe, P. and H. Kopka**, Modification of the F-region by Powerful Radio Waves, in: *Exploration of the Polar Upper Atmosphere*, eds C. S. Deehr and J. A. Holter (Riedel, Dordrecht, Netherlands, 1981), 83-88.
- Stubbe, P., H. Kopka, T. B. Jones and T. R. Robinson**, Wide Band Attenuation of Radio Waves Caused by Powerful HF Waves: Saturation and Dependence on Ionospheric Variability, *J. Geophys. Res.*, **87**, 1551-1555, 1982.
- Stubbe, P.**, Review of ionospheric modification experiments at Tromsø, *J. Atmos. Terr. Phys.*, **58**, 349-368, 1996.
- Tellegen, B. D. H.**, Interaction between Radio-Waves?, *Nature*, **131**, 840, 1933.
- Thome, G. D. and D. W. Blood**, First observations of RF backscatter from field-aligned irregularities produced by ionospheric heating, *Radio Science*, **9**, 917-921, 1974.
- Titheridge, J. E.**, Ionogram Analysis - Least-Squares Fitting Of A Chapman-Layer Peak, *Radio Science*, **20**, 247-256, 1985.
- Tomko A. A., A. J. Ferraro, and H. S. Lee**, D-region absorption effects during high power radio wave heating., *Radio Science*, **15**, 675-682, 1980
- Turunen, T.**, GEN-SYSTEM - A new experimental philosophy for EISCAT radars, *J. Atmos. Terr. Phys.*, **48**, 777, 1986.
- Utlaut, W. F. and E. J. Violette**, Further ionosonde observations of ionospheric modification by a high powered ground-based transmitter, *J. Geophys. Res.*, **77**, 6804-6818, 1972.
- Utlaut, W. F. and E. J. Violette**, A summary of vertical incidence radio observations of ionospheric modification, *Radio Science*, **9**, 895-903, 1974.
- Villain, J. P., R. A. Greenwald, K. B. Baker, and J. M. Ruohoniemi**, HF radar observations of E-region plasma irregularities produced by oblique electron scattering, *J. Geophys. Res.*, **92**, 12327-12342, 1987.
- Walker, J. C. G.**, Active experimentation with the ionospheric plasma., *Rev. Geophys. Space Phys.*, **17**, 534, 1979.